



1993年

263

**A Study on
Optical Second Harmonic Generation Devices
Based on Organic Materials**

(有機材料を用いた光第二高調波発生素子に関する研究)

by

Takashi ISOSHIMA

DISSERTATION

submitted in partial satisfaction of the requirements for the degree of
Doctor of Philosophy in Engineering
in the Graduation Division of The University of Tokyo

Research Advisor: Professor Kunio TADA

Contents

Chapter 1 Introduction	1
1.1 Background	1
1.1.1 Nonlinear Optical Materials	2
1.1.2 Phase Matching Methods for SHG	4
1.1.3 A Brief Review on SHG Devices	7
1.1.4 Organic Nonlinear Optical Material MNA	8
1.2 The Purpose and the Constitution of This Dissertation	10
 Chapter 2 Theory of Second Harmonic Generation	
Using the Local Normal Mode Expansion	12
2.1 Introductory Remarks	12
2.2 Necessity of the Local Normal Mode Expansion Method	13
2.3 Derivation of General Nonlinear Coupled Mode Equations	14
2.4 Derivation of Nonlinear Coupled Mode Equations for SHG	16
2.5 SHG Efficiency and Effective SHG Coefficient	18
2.6 Concluding Remarks	20
Appendix 2.A Normalization Factor of a Field Profile Function	20
Appendix 2.B A Discussion on Definitions of the Effective Cross Section of the Waveguide	21
Appendix 2.C A Discussion on the Validity of the Single Mode Approximation	22
 Chapter 3 Analyses on Some Types of	
Quasi Phase Matching SHG Devices	25
3.1 Introductory Remarks	25
3.2 Quasi Phase Matching SHG Devices with Corrugation	25
3.2.1 Analytical Expression in the Limit of Strong Confinement	26
3.2.2 A Numerical Example	27
3.3 Quasi Phase Matching SHG Device by Periodic Domain Inversion	30
3.3.1 Analytical Expression in the Limit of Strong Confinement	30
3.3.2 Numerical Examples	30
3.4 Concluding Remarks	33

Chapter 4 Proposal of New Fabrication Methods of

Channel Waveguides Based on Organic Materials	34
4.1 Introductory Remarks.....	34
4.2 Proposal of New Fabrication Methods for Organic Channel Waveguides	36
4.3 Fabrication Method of a Hollow Core I - the Deposition Method.....	36
4.4 Fabrication Method of a Hollow Core II - the Sticking Method.....	37
4.5 Fabrication Method of a Hollow Core III - the Deposition Method with Interference Exposure to Fabricate Corrugated Waveguides.....	37
4.6 Concluding Remarks.....	38

Chapter 5 Examinations on Process Conditions for

Each Fabrication Step	39
5.1 Introductory Remarks.....	39
5.2 Substrate Preparation Step	40
5.3 Hollow Core Fabrication Step I - the Deposition Method.....	40
5.3.1 Evaluation Criteria and Examined Materials and Methods	41
5.3.1.1 The Matrix Core Fabrication Step.....	41
5.3.1.2 The Upper Clad Deposition Step.....	41
5.3.1.3 The Matrix Core Removal Step.....	42
5.3.1.4 Combinations of Examined Materials, Deposition Methods, and Removal Methods	43
5.3.2 Examination and Improvement of Process Combinations	43
5.3.2.1 Examination of Combinations 1.- 4.	43
5.3.2.2 Examination of Combinations 5. and 6.....	46
5.3.2.3 Examination of Combinations 7. and 8.....	47
5.3.3 Summary of the Examinations for the Deposition Method.....	50
5.4 Hollow Core Fabrication Step II - the Sticking Method.....	51
5.4.1 The Photolithography Step.....	52
5.4.2 The Etching Step.....	52
5.4.3 The Sticking Step.....	52
5.5 Hollow Core Fabrication Step III - the Deposition Method with Interference Exposure to Fabricate Corrugated Waveguides.....	53
5.6 MNA Core Crystallization Step.....	55
5.6.1 Evaluation Methods of MNA Crystal Quality and Orientation.....	55
5.6.2 Examination of MNA Crystal Growth Methods.....	56
5.6.2.1 The Slow Uniform Cooling Method.....	56
5.6.2.2 The Bridgeman Method I	58

5.6.2.3 The Zone Melting Method	58
5.6.2.4 The Bridgeman Method II	59
5.6.3 Summary of MNA Crystal Growth	60
5.7 Waveguide End Surface Cutting Method	60
5.8 Concluding Remarks	61
Appendix 5.A Photolithography Conditions	62
Appendix 5.B Conditions and Some Comments on SiO ₂ Upper Clad Deposition	63
5.B1 Sol-Gel Method	63
5.B2 Plasma-CVD Method	63
5.B3 RF Sputtering Method	63
5.B4 RF Magnetron Sputter Method	64
5.B5 Additional Polyimide Coating Method	64
Appendix 5.C Measurement of Core Refractive Indices and Crystal Orientation with an Interference Microscope	64
Chapter 6 Evaluation of MNA Waveguides and SHG Devices	66
6.1 Introductory Remarks	66
6.2 Evaluation of Channel Waveguides	66
6.3 Evaluation of SHG Devices	68
6.4 Concluding Remarks	71
Appendix 6.A SHG Efficiency with Propagation Loss	71
Chapter 7 Conclusion	73
Acknowledgments	77
References	79
Publication List	82

Chapter 1

Introduction

1.1 Background

Nonlinear optics, which began with the discovery of the electro-optic effects of the first order (Pockels effect) and the second order (Kerr effect) at the end of the 19th century, has been making rapid progress since the invention of lasers which make it possible to generate a very large optical field with single frequency. Applications of nonlinear optics expand over very wide regions such as: second harmonic generation (SHG) and optical parametric wavelength conversion which uses the second order optical nonlinearity, optical modulation which uses the Pockels or the Kerr effect, and all-optical switching and optical information processing using the third order optical nonlinearity. Some field of quantum optics [1] and material physics, such as quantum nondemolition measurement which uses the optical Kerr effect, squeezing of light which uses the fact that a nonlinear optical process is a multiphoton process, and nonlinear spectroscopy, are also applications of nonlinear optics. Materials for nonlinear optics are also studied very extensively [2][3] such as ferroelectrics, semiconductors, semiconductor quantum well structures, semiconductor doped glasses, low molecular weight organics, and organic polymers. Still, the currently available magnitude of optical nonlinearity is far from sufficient in most of those applications. Therefore, the necessity of research on materials with much higher optical nonlinearity and on device structures suitable for such materials, are growing even more.

As for SHG, efficiency is proportional to the square of the second order nonlinear optical coefficient of a material and to the power density of the fundamental wave. Therefore, in order to establish high conversion efficiency, it is necessary to use a material with a large second order optical nonlinearity in a device structure which can confine light strongly. Thus, waveguide and/or resonator structures are applied to ferroelectrics, semiconductors, and organics. Another point for high conversion efficiency is the phase matching method. In the following subsections, brief reviews on fundamental concepts and topics are presented. In subsection 1.1.1, nonlinear optical materials are reviewed. In subsection 1.1.2, SHG devices are reviewed in the relation with materials. In subsection 1.1.3, phase matching methods are reviewed. In subsection 1.1.4, features of a low molecular weight organic material MNA which is employed in this work are summarized.

1.1.1 Nonlinear Optical Materials

Optical nonlinearity is caused by a nonlinear relation between an applied electromagnetic field and a reaction of a material to the field, i.e. dielectric polarization. Macroscopic dielectric polarization P and molecular polarization p can be expressed as a power series of externally applied electric field E or local electric field ε at the molecule, as follows:

$$P = \mu_0 + \chi^{(1)} \cdot E + \chi^{(2)} : EE + \chi^{(3)} :: EEE + \dots \quad (1-1)$$

$$p = \Delta\mu_0 + \alpha \cdot E + \beta : EE + \gamma :: EEE + \dots \quad (1-2)$$

where μ_0 is the macroscopic permanent dipole moment, $\chi^{(1)}$ the linear electric susceptibility (second rank tensor), $\chi^{(2)}$ the second order nonlinear electric susceptibility (third rank tensor), $\chi^{(3)}$ the third order nonlinear electric susceptibility (fourth rank tensor), $\Delta\mu_0$ the molecular permanent dipole moment, α the linear molecular polarizability (second rank tensor), β the second order nonlinear hyperpolarizability (third rank tensor), and γ the third order nonlinear hyperpolarizability (fourth rank tensor). Macroscopic parameters depend not only on the molecular parameters but also on the symmetry of the crystal. For example, a centro-symmetric crystal has no even order optical nonlinearity even though its even order molecular hyperpolarizability is large. The magnitude of these molecular parameters can be decomposed into some kinds of polarizations, that is, polarization caused by atomic core displacement, i.e., lattice vibration, electronic polarization, and complex contribution of lattice vibration and electronic polarization. Each of them has its own cut off frequency, and contributes only for a frequency lower than the cut-off. In optical parametric process, only the electronic polarization contributes. In the Pockels effect with an applied electric field of a frequency lower than the lattice vibration resonant frequency, polarization from lattice vibration also contributes. In this subsection, only electronic polarization is considered for the optical SHG process.

It is known empirically that there is a correlation relation between nonlinear and linear susceptibility. Miller pointed out empirically that the value

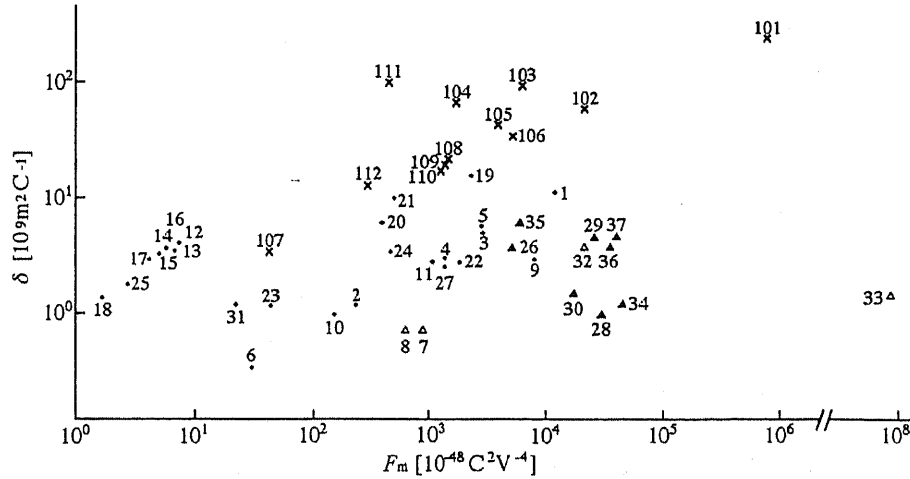
$$\delta = \frac{\chi^{(2)}}{\{\chi^{(1)}\}^3} \quad (1-3)$$

which is called Miller's delta, is almost constant for any material [4]. Later, it was pointed out theoretically that δ is not a constant but proportional to dielectric moment of atomic bonds [5].

Materials with a nonlocalized electron cloud are known to have large electronic polarization. For example, organic materials with conjugated π electrons which expand all over the molecule, such as substitution products of benzene, have large optical nonlinearity because of its nonlocalized π electrons [6]. In general, a substituted group in a molecule causes deformation of π electrons, and the second order optical nonlinearity is enhanced with large molecular dielectric moment of deformed π electrons. This effect, which is called the mesomeric effect, increases with the size of nonlocalized π electrons system. In addition, substitution with a donor group and an acceptor group increases the difference of dielectric moment between excited and ground states a lot, and this causes further enhancement of the second order nonlinearity [6][7]. This charge transfer effect also increases with

the size of nonlocalized π electrons system. On the other hand, the lowest electronic transition energy decreases with the increase of the size of localized π electrons system, which means the increase of absorption edge in wavelength.

Figure 1-1 shows the second order optical nonlinearity of various materials [8]. The abscissa of the figure



Number	Material	Tensor index	Number	Material	Tensor index
1	LiNbO ₃	33	20	LiIO ₃	31
2	LiNbO ₃	31	21	LiIO ₃	33
3	Ba ₂ NaNb ₅ O ₁₅	33	22	BaTiO ₃	31
4	Ba ₂ NaNb ₅ O ₁₅	31	23	ZnO	14
5	LiTaO ₃	33	24	ZnO	33
6	LiTaO ₃	31	25	SiO ₂	11
7 ^a	Ag ₃ AsS ₃	31	26	CaS ₂	33
8 ^a	Ag ₃ SeS ₃	31	27	ZnS	33
9	PbTiO ₃	31	28	GaAs	14
10	SrBaNb ₄ O ₁₂	31	29	CdSe	31
11	SrBaNb ₄ O ₁₂	33	30	GaP	14
12	(NH ₃)H ₂ PO ₄	36	31 _b	(NH ₂ CH ₂ COOH) ₃ H ₂ SO ₄	23
13	(NH ₃)H ₂ PO ₄	14	32 _a	HgS	11
14	KH ₂ PO ₄	36	33 _a	InP	11
15	KD ₂ PO ₄	36	34 _a	InP	14
16	RbH ₂ PO ₄	14	35	CuI	14
17	RbH ₂ PO ₄	36	36	InAs	14
18	RbH ₂ AsO ₄	36	37	ZnTe	14
19 ^b	LiIO ₃	31			

Number	Material	Tensor index
101	MNA (5-nitro-2-aminotoluene)	11
102	MNA	12
103	MAP ((3-methyl-2,4-dinitrophenyl)-aminopropanate)	21
104	MAP	22
105	mNA (meta-nitroaniline)	31
106	mNA	33
107	mNA	32
108	POM (3-methyl-4-nitropyridine-1-oxide)	36
109	POM	14
110	POM	25
111	HEX (hexamine)	14
112	BZL (benzil)	11

Fig.1-1 Comparison of various nonlinear optical materials (modified from figures in Ref.[8]) The vertical axis shows the Miller's delta and the horizontal axis shows the figure of merit for SHG F_m . Definitions of δ and F_m are a little different from those in Eqs.(1-3) and (1-4), as follows: $\delta = d/\epsilon_0^3 \chi^{(1)2}(\omega) \chi^{(1)}(2\omega)$; $F_m = d^2/n^2(\omega) n(2\omega)$. The filled circles show ferroelectrics and oxides, the triangles semiconductors, and the cross organics. Empty triangles show values at 10.6 μ m, and other marks at 1.06 μ m, except for Nos.18 and 31 which show values at 0.6943 μ m.

shows the figure of merit F_m for SHG defined as follows:

$$F_m = \frac{\{\chi^{(2)}\}^2}{\{\chi^{(1)}\}^3} \quad (1-4)$$

SHG efficiency is proportional to this figure of merit F_m . The ordinate shows the Miller's delta δ defined as Eq.(1-3). The filled circles show ferroelectrics and oxides, the triangles semiconductors, and the crosses organics. In general, semiconductors with high refractive index have a larger figure of merit F_m than ferroelectrics with lower refractive index. On the other hand, some organics with nonlocalized π electrons have very large figures of merit F_m in spite of their low refractive index.

1.1.2 Phase Matching Methods for SHG

Generally speaking, in order to make an accumulative interaction between electromagnetic fields in two modes, the phase velocities of these interacting modes must be equal, that is, the phase matching should be fulfilled. In other words, the photon momentum of interacting modes must be preserved during the interaction.

It is the same in the SHG process, and phase matching is necessary to achieve high conversion efficiency. Phase matching in SHG can be understood intuitively as follows: if phase velocity of second harmonic mode is different from that of fundamental mode, the second harmonic field generated in a position of nonlinear medium and in another position which has propagated to the former position have different phases which cancel out. The length in which the phase difference is π is called the coherent length.

Optical media have normal dispersion in the transparent region and the refractive index increases with the decrease of wavelength. Therefore, it is impossible to achieve phase matching between fundamental and second harmonic, unless some special devices are employed. However, in optical waveguides, various phase matching methods can be used as follows: use of media birefringence, use of modal dispersion in waveguide, use of Cerenkov radiation mode, use of periodic structure (quasi phase matching), use of two fundamentals which propagate in opposite direction to each other. On the contrary, the phase matching method in bulk media is limited to the use of birefringence and of periodic domain inversion [9], and the former is usually employed. These methods are described briefly in the next paragraphs, and their features are summarized in Table 1-I.

1) Phase matching with medium birefringence

Refractive indices for two orthogonal polarization in a birefringent medium are different from each other. Therefore, the refractive index for the fundamental wave of a polarization can be equalized to that for second harmonic wave of the other polarization by controlling the crystal angle or temperature, and thus phase matching is achievable [10]. In this method, there is no decrease of SHG efficiency originating from the phase matching method, because phase matching is achieved by controlling the refractive indices of the medium. On the other hand, phase matching is not achievable between modes of the same polarization. Many of the nonlinear optical media such as MNA and LiNbO₃ have much larger nonlinear constant for the same polarization compared to that

for different polarizations, and these large nonlinearity cannot be used in this phase matching method.

2) Phase matching with modal dispersion in a waveguide

A modal field feels an effective refractive index which is affected by the refractive index of the medium, the waveguide form, and the order of lateral mode. Phase matching cannot be achieved between the fundamental and second harmonic modes of the same order because of the normal dispersion of a medium. On the other hand, the effective refractive index for a higher order mode decreases with the order of mode, and therefore an effective refractive index of a higher order second harmonic mode can be equalized to that of a lower order fundamental mode. In this method, orders for fundamental and second harmonic are different to each other and field profiles of these modes are almost orthogonal. Hence, overlap integral is small, resulting into small SHG efficiency. Overlap integral can be increased with a special structure such as four layer waveguide [11]. Another disadvantage is the requirement of very high accuracy of waveguide size in fabrication, because the modal effective indices are very sensitive to the size of a waveguide. This requirement can be relaxed a little by setting the size of a waveguide to a 'noncritical' size [12].

3) Phase matching with Cerenkov radiation mode

Polarization propagating faster than light in a medium radiates electromagnetic field slantways. This is called Cerenkov radiation. In SHG process, Cerenkov radiation can be generated if the phase velocity of the second harmonic polarization, which is same as that of the fundamental wave, is larger than that of the second harmonic wave in the clad medium. Second harmonic wave is radiated into an angle which satisfies phase matching condition, and this means that slight fabrication errors in waveguide parameters affect only the radiation angle and SHG efficiency is not seriously degraded. Still, it has been theoretically shown that SHG efficiency varies largely with the variation of waveguide size because of phase matching in the lateral direction of the waveguide [13][14], and a certain accuracy in fabrication is required even though the constraint is much looser than in other methods such as the modal dispersion phase matching method. In addition, SHG efficiency in this method is proportional to device length, rather than square of that as in other colinear phase matching methods, and is rather low because of the short interaction length. The fact that second harmonic is radiated slantways can be a disadvantage in some applications such as optical integrated circuits.

4) Phase matching with periodic structures (quasi phase matching)

A periodic structure causes periodic spatial modulation in amplitude and phase of electromagnetic fields in a waveguide, resulting into sidebands, which are called spatial harmonics, separated from each other by the wavenumber of the periodic structure. Coupling between those spatial harmonics of the fundamental and second harmonic causes phase matching. This method does not equalize the refractive indices themselves, and is thus called *quasi* phase matching method. In the SHG process, quasi phase matching is achieved through spatial harmonics around the propagation coefficient of the nonlinear polarization of second harmonic frequency driving a second harmonic propagation mode. In this method, a diagonal element of the nonlinear coefficient tensor, i.e. nonlinear coefficient for same polarization, can be used. In addition, the same order of modes for the fundamental

and second harmonic can be used to avoid reduction of overlap integral. There are two types of periodic structure:

- 4-1) Periodic ferroelectric domain inversion. Optical nonlinearity of the second order is caused by a bias of spontaneous polarization electric field applied to that of third order. Therefore, ferroelectric domain inversion causes inversion in sign of second order nonlinear coefficient, and thus inversion in phase of second harmonic polarization. This phase modulation causes spatial harmonics resulting into phase matching. This can be described in real space as follows: second harmonic waves radiated at two points separated by coherence length are out of phase by π and cancel out each other without domain inversion, while when the domain inversion has a period of twice of the coherence length, they are in phase and accumulative. Although SHG efficiency is rather high in this method, the applicable medium is limited to those of which ferroelectric domain can be inverted, such as LiNbO_3 and LiTaO_3 .
- 4-2) Corrugation. Corrugation of a waveguide causes periodic spatial modulation in amplitude and in phase of the second harmonic polarization through two effects, that is, the nonlinear coefficient modulation and the linear refractive index modulation. The former causes amplitude modulation of the second harmonic polarization. The latter causes amplitude modulation of the second harmonic polarization through the modulation of lateral field profile, and phase modulation of the second polarization through the modulation of propagation coefficient. This can be described in real space as follows: second harmonic waves radiated at two points separated by coherence length cancel out each other without corrugation, while they cannot cancel out totally and the residual accumulates with corrugation. It can be easily seen that SHG efficiency in this method is smaller than in the periodic domain inversion method. In addition, corrugation may cause coupling between guided and radiation modes. On the other hand, this method can be easily applied to any material in which corrugated waveguides can be fabricated.
- 5) Phase matching with two counter-propagating fundamental and normally radiating second harmonic modes

Two fundamentals propagating in the opposite direction give a total wavenumber of 0 in the propagating direction. Hence, the second harmonic is always radiated normal to the waveguide for any fundamental wavelength [15][16][17]. Though phase matching in the transversal direction causes periodic decrease of the SHG efficiency with increase of waveguide size, the requirement for waveguide size accuracy is not so tight because the interaction length is short. However, the short interaction length results in low SHG efficiency, as in the Cerenkov radiation method. Therefore, this method is mainly applied to optical measurement devices such as optical correlators and spectrometers, rather than to short wavelength light sources. Optical correlators can be used to measure an ultra short optical pulse form through observing the longitudinal distribution of the radiated second harmonic intensity. In spectrometers, a wave to be measured propagates forward and interacts with a single frequency reference wave propagating backward, and spectrum of the forward wave can be obtained as the angular distribution of sum frequency wave intensity, because the radiation angle depends on the wavelength of the forward wave.

Table 1-I Features of various phase matching methods

Phase matching method	Efficiency	Available tensor index	Sensitivity to fabrication error	Available material	Output direction
Birefringence	O	X	Δ	Δ	O
Modal dispersion	X~O	O	X	O	O
Cerenkov radiation	X	O	O	O	X
Quasi phase matching	Periodic domain inversion	O	O	Δ	X
	Corrugation	Δ	O	Δ	O
	Counter propagation	X	O	O	O

1.1.3 A Brief Review on SHG Devices

In this section, some materials, that is, ferroelectrics, semiconductors, organic molecular crystals, and organic polymers, are briefly reviewed from the standpoint of SHG devices.

Ferroelectrics such as LiNbO_3 , LiTaO_3 , and KTiO_2PO_5 (KTP) are the most advanced in SHG device fabrication technology. Although a Ti-indiffused LiNbO_3 channel waveguide with birefringent phase matching[10][18] was popular formerly, attentions are now focused on proton exchange channel waveguide devices with periodic domain inversion quasi phase matching. LiTaO_3 and KTP, which are known for higher optical damage threshold than LiNbO_3 also attract a lot of attention. Especially, LiTaO_3 devices are almost completed in a sense that experimental SHG efficiency has almost reached the theoretical limit, i.e. about $150\%/W^{-1}\text{cm}^{-2}$ [19][20] and that quality of waveguides is very high. Hence, recent studies focus on extending the allowance in phase matching wavelength rather than improving the SHG efficiency.

Semiconductors are not so popular for near infrared and visible SHG materials. This is because the GaAs family, in which monolithic integration with laser diodes and modulators is easily achievable, absorbs visible light, and II-VI semiconductors, such as ZnS, which are transparent for visible light has small optical nonlinear coefficient, e.g. several pm/V. The only GaAs SHG device in which both the fundamental and second harmonic are guided modes employed quasi phase matching with corrugation and the fundamental wavelength was $2.1\mu\text{m}$ [21]. Some GaAs devices using counter-propagating fundamentals for phase matching have been reported for visible second harmonic [15][16][17][22][23], mainly aimed for optical measurement devices as mentioned above. As a material, although enhancement of nonlinearity with quantum well structures may be expected as in the Kerr effect through the quantum confined Stark effect, the SHG coefficient of quantum well structures for near infrared region in which interband transitions play a major role is the same order as bulk, with almost no enhancement [24][25].

Low molecular weight organic materials are attracting a lot of attention because of their extremely large optical nonlinearity. However, device fabrication technology of these materials is immature. Planar waveguides are fabricated by filling and crystallizing an organic material between two glass substrates, though this method has a difficulty in controlling the thickness of the waveguide. Most of the channel waveguides are fabricated with hollow core fiber filled by an organic crystal. Phase matching method is almost limited to Cerenkov radiation. Reported propagation loss of a waveguide is rather high, and treatment of waveguide incident surface is difficult because of the low hardness of the material. Thus, experimentally demonstrated SHG efficiency is still lower than the theoretical prediction by several orders of magnitude. Still, optical nonlinearity of some of the low molecular weight organics is the highest among various kind of materials, and theoretical prediction shows the SHG efficiency based on these materials to be higher than that in ferroelectric devices by a few orders of magnitude. Recently, new attempts such as heteroepitaxial crystal growth of organic materials have been reported to fabricate high quality waveguides.

Organic polymers are easily fabricated into planar waveguides with spin coating method. Groups with high second order nonlinearity are substituted into the subchain or mainchain of a polymer and the second order nonlinearity is activated with the electric field poling at a temperature above the glass transition temperature of the polymer. However, the glass transition temperatures of most polymers are around 100°C, and the relaxation of molecular alignment cannot be negligible even at the room temperature. This relaxation can be suppressed to certain extent with some methods such as cross linking. Another problem is absorption edge of nonlinear groups which are as long as 700nm for red dyes with large nonlinearity. Density of nonlinear groups is not so high, and the nonlinear coefficient is lower than that of low molecular weight organics. As phase matching methods, the Cerenkov radiation method and the periodic domain inversion method through the poling process are often employed. The Cerenkov radiation method is suitable for a device in which the second harmonic wavelength is within the absorption band, because of the short interaction length. Channel waveguides can be fabricated with etching or photobreaking, and propagation loss of lower than 1dB/cm can be obtained.

1.1.4 Organic Nonlinear Optical Material MNA

5-nitro-2-aminotoluene (better known as alias 2-methyl-4-nitroaniline, MNA) is a low molecular weight organic material with a molecular structure shown in Fig.1-2. Nonlocalized π electrons cause large second order nonlinearity through the charge transfer effect with a donor of an amino group and an acceptor of a nitro group [6][7][26][27][28]. The figure of merit for SHG is three orders of magnitude larger than that of LiNbO_3 d_{31} , and one and a half order larger than that of LiNbO_3 d_{33} .

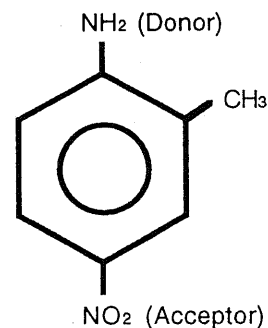


Fig.1-2 The molecular structure of MNA.

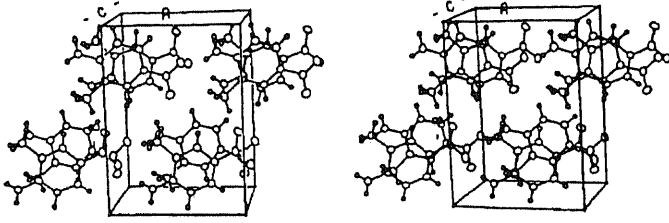


Fig.1-3 Stereoscopic view of the unit cell of MNA [27].

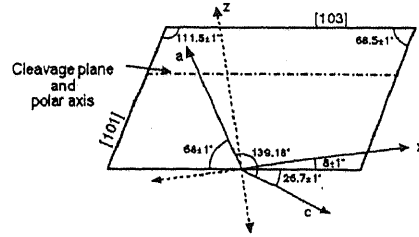


Fig.1-4 Schematic diagram of an MNA crystal. [27] The relative orientation of the crystal morphology, principal axes, and crystallographic axes are shown.

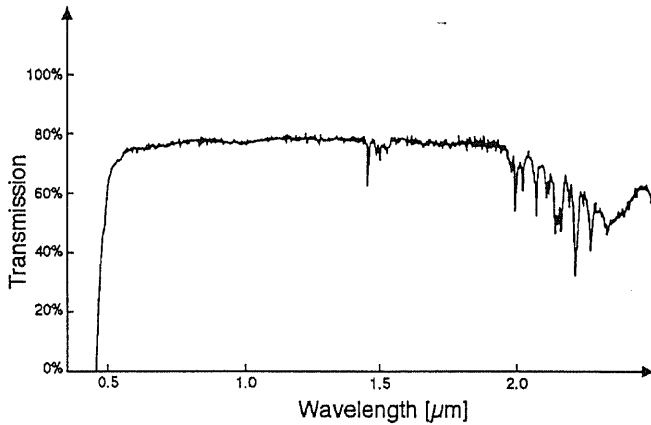


Fig.1-5 Transmission spectrum of an MNA crystal. [26]

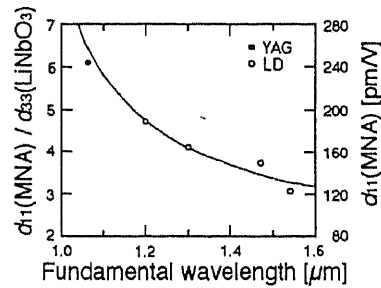
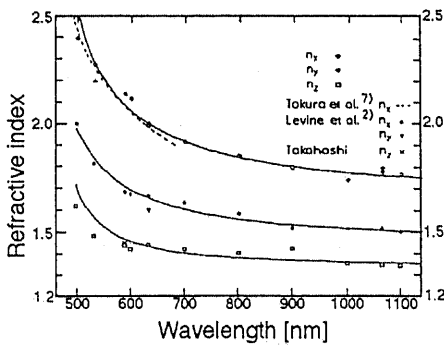
Fig.1-6 Dispersion of nonlinear coefficient d_{11} of MNA [29]. The abscissa represents the fundamental wavelength.

Fig.1-7 Dispersion of the refractive indices of MNA [30]. The solid lines represent the least-squares fit to the Sellmeier formula.

Table 1-II Sellmeier coefficients of MNA [30]

$$n^2 = A + \frac{B}{1 - \frac{C}{\lambda^2}} \quad (\lambda: \mu\text{m})$$

	A	B	C
n_x	1.27	1.56	0.172
n_y	1.37	0.78	0.174
n_z	1.53	0.26	0.204

MNA is yellow solid at room temperature. The melting point is 131°C. It is easily sublimated, and easily dissolved by most of the organic solvents. The single crystal has a thin flake-like form, and the molecular crystal is monoclinic with the space group of Cc . The unit cell is shown in Fig.1-3 [27], and the lattice constants are $a=11.57\text{\AA}$, $b=11.62\text{\AA}$, $c=8.22\text{\AA}$, and $\beta=139.18^\circ$ [26][27][28]. The relative orientation of the crystal morphology, principal axes, and crystallographic axes of an MNA crystal are shown in Fig.1-4 [27]. The optical x axis has the

largest nonlinearity. The absorption edge is about $0.5\mu\text{m}$, as is shown in Fig.1-5 [26]. Figure 1-6 shows the dispersion of SHG coefficient d_{11} [29]. Dispersion of the refractive index for each of the optical axis is shown in Fig.1-7, and the Sellmeir coefficient in Table 1-II [30].

1.2 The Purpose and the Constitution of This Dissertation

The purpose of this dissertation is to realize high efficiency SHG devices. As the nonlinear optical material, MNA is employed because of its extremely large optical nonlinearity as described above, and of its availability. A channel waveguide structure is employed as the device structure because of its high optical confinement. As the phase matching method, the quasi phase matching method with corrugation is employed because of its applicability to organic materials such as MNA, and of its high degree of freedom in device design. Such a device has not yet been studied theoretically and experimentally. Therefore, the definite aims are to establish a new SHG theory based on the local normal mode expansion to analyze the devices, and new fabrication methods of organic channel waveguides including corrugated ones for quasi phase matching SHG, and to evaluate these devices.

This dissertation is composed of seven chapters.

In Chapter 2, SHG theory is newly developed based on the local normal mode expansion. The necessity of local normal mode expansion in the analysis of SHG is presented first. A general expression for the nonlinear coupled mode equation with the local normal mode expansion is derived from the Maxwell equations. Nonlinear coupled mode equations for SHG are derived from the general expression, and expressions for the SHG efficiency and the effective SHG coefficient are derived.

In Chapter 3, analyses on some types of quasi phase matching SHG devices, i.e., a device with corrugation and a device with periodic domain inversion, are presented. Analytical expressions for the SHG efficiency and the effective SHG coefficient under the strong light confinement approximation, which is useful for the rough estimation of device performance, are derived for each type of devices. In addition, numerical examples are presented and compared with the results of the ideal normal mode expansion.

In Chapter 4, new fabrication methods of low molecular weight organic channel waveguides are proposed. These methods has no disadvantages of the conventional channel waveguide fabrication methods such as low accuracy of size. The outline of these methods is described first, and then fabrication methods of the hollow core, which are the most important part of the proposed methods, are described. A fabrication method of the hollow core with corrugation, which is aimed to achieve quasi phase matching for SHG, is also described.

In Chapter 5, each step of the processes proposed in Chapter 4 are examined experimentally. The

fabrication methods described in Chapter 4 can be achieved utilizing process technologies for semiconductors. Still, the materials and combinations of technology are different from semiconductor processes, and hence thorough examination of each fabrication step is necessary. In this chapter, the substrate preparation step, the hollow core fabrication step for which the deposition method, the sticking method, and the deposition method with interference exposure are proposed in the previous chapter, the MNA crystal core fabrication step, and the waveguide edge treatment step are examined.

In Chapter 6, MNA channel waveguides and SHG devices are evaluated. The devices are uniform channel waveguides, Y-branches, and corrugated channel waveguide quasi phase matching SHG devices, and light guiding experiment, propagation loss measurement, and SHG experiment are described.

In Chapter 7, all the results are summarized and conclusions are presented.

Chapter 2

Theory of Second Harmonic Generation Using the Local Normal Mode Expansion

2.1 Introductory Remarks

The local normal mode expansion has been used for analysis of linear mode coupling in a waveguide, but never been used for analysis of nonlinear mode coupling. However, the local normal mode expansion makes the analysis easy in a waveguide with a periodic structure. Thus, in this chapter, a second harmonic generation theory is reconstructed with the local normal mode expansion.

This chapter has 6 sections and 3 appendices.

In section 2.2, the necessity of local normal mode expansion in the analysis of SHG is presented.

In section 2.3, a general expression of nonlinear coupled mode equations with the local normal mode expansion is derived from the Maxwell equations.

In section 2.4, nonlinear coupled mode equations for SHG is derived from the general expression.

In section 2.5, expressions of SHG efficiency and effective SHG coefficient are derived.

In section 2.6, the summary of this chapter is presented.

In appendix 2.A, a normalization factor of a modal field profile function of a channel waveguide is presented.

In appendix 2.B, definitions of effective cross section of a waveguide are discussed.

In appendix 2.C, the validity of the single mode approximation in the LNME method is discussed.

2.2 Necessity of the Local Normal Mode Expansion Method

Theoretical analyses and numerical calculations on the SHG efficiency under QPM were given by many researchers [19][21][31][32][33][34][35][36]. However, these are not sufficient. In order to precisely evaluate the SHG efficiency in a waveguide with a periodic structure, the exact electric field profile in a waveguide, which varies periodically along longitudinal direction of the waveguide because of the periodic structure, must be evaluated. This is true not only for QPM with corrugation, but also for QPM with a periodic domain inversion in a ferroelectric waveguide because the domain inversion process also causes a change of the linear refractive index, resulting in a change of the field profile. In the above mentioned analyses and calculations, the ideal normal mode expansion (INME), which uses modes for a waveguide of averaged width and refractive index as the basis of the expansion [37][38][39][40], is employed to describe the electric field profile in a waveguide. In the analysis of the mode coupling through *linear* refractive index perturbation only, the perturbation polarization is expressed by a superposition of the linear polarizations originating in fields of existing modes. The modal amplitude driven with a perturbation polarization originating in phase mismatched modes only oscillate with a small amplitude and do not accumulate. Therefore, coupling between modes without phase matching can be ignored. On the other hand, in the analysis of the mode coupling through *nonlinear* polarization, a perturbation polarization cannot be expressed as a superposition of nonlinear polarizations each originating in the existing modes. Therefore, many modes, whether phase matched or not, must be considered to evaluate the nonlinear polarization exactly and the single mode approximation which is almost always used may give a wrong result. This means that the amount of calculation for SHG efficiency is very large, i.e., one must solve multimode coupled mode equations which have both *linear* and *nonlinear* perturbation polarization terms.

On the contrary, in the case of the local normal mode expansion (LNME), which uses modes for a waveguide of local width and refractive index as the basis of the expansion [38][39][40], the electric field distribution in a waveguide can be described rather exactly even with the single mode approximation. Therefore, the amount of calculation can be reduced a lot. In addition, the fact that we can see the change in the magnitude and the profile of field along the propagating direction without superposing many modes, gives us intuition to understand the physical mechanism of quasi phase matching.

In this dissertation, we present nonlinear coupled mode equations based on the LNME for the first time. Expressions for SHG efficiency and effective SHG coefficient are also derived. In addition, we give theoretical and numerical analyses on two types of QPM devices: one is with corrugation and the other with a periodic domain inversion. The numerical examples are based on a corrugated channel waveguide device using an organic MNA and a periodically domain inverted channel waveguide device using a ferroelectric LiNbO₃. The results are compared to those obtained by the conventional INME.

2.3 Derivation of General Nonlinear Coupled Mode Equations

In the following discussion, we define the transverse plane of the waveguide to be in the xy plane and the longitudinal direction to be the z direction. In the LNME, the field in the actual waveguide at z is expanded with a set of eigenmodes for a hypothetical longitudinally uniform waveguide which has the same cross section as the actual waveguide at z [38][39][40]. This hypothetical waveguide has no optical nonlinearity. Electric and magnetic fields in the hypothetical waveguide $\{E^{(0)}(x,y,z), H^{(0)}(x,y,z)\}$ can be written as follows:

$$E^{(0)}(x,y,z) = E_\mu(x,y,z) \exp\left[-i \int_0^z \beta_\mu(\zeta) d\zeta\right], \quad (2-1)$$

$$H^{(0)}(x,y,z) = H_\mu(x,y,z) \exp\left[-i \int_0^z \beta_\mu(\zeta) d\zeta\right], \quad (2-2)$$

where $E_\mu(x,y,z)$ and $H_\mu(x,y,z)$ are the normalized modal field profiles, $\beta_\mu(z)$ the propagation coefficient, and μ the mode index number. We define the sign of $\beta_\mu(z)$ as positive for a mode propagating to $+z$ direction and negative for $-z$ direction [41]. These fields follow the Maxwell's equations for the hypothetical waveguide:

$$\nabla \times E^{(0)}(x,y,z) = -i \omega \mu_0 H^{(0)}(x,y,z), \quad (2-3)$$

$$\nabla \times H^{(0)}(x,y,z) = i \omega \varepsilon_0 \hat{\varepsilon}_r(x,y,z) E^{(0)}(x,y,z), \quad (2-4)$$

where ω is the angular frequency and $\hat{\varepsilon}_r(x,y,z)$ the relative linear dielectric tensor. It should be noted that argument z of this tensor is not a variable but a parameter in Eqs (2-3) and (2-4). We can decompose the operator ∇ into transverse and longitudinal components [38]:

$$\nabla = \nabla_t + \mathbf{e}_z \frac{\partial}{\partial z} \quad (2-5)$$

where subscripts t and z denote the transverse and the longitudinal components, respectively. \mathbf{e}_z is a unit vector in the z direction. In Eqs. (2-3) and (2-4), the argument z of the modal field profiles $E_\mu(x,y,z)$ and $H_\mu(x,y,z)$ is treated as a parameter and derivatives in z does not operate on these modal field profiles. Therefore, Eqs. (2-3) and (2-4) can be rewritten using Eqs. (2-1), (2-2) and (2-5) as follows:

$$\nabla_t \times E^{(0)}(x,y,z) - i\beta_\mu(z) \mathbf{e}_z \times E^{(0)}(x,y,z) = -i \omega \mu_0 H^{(0)}(x,y,z), \quad (2-6)$$

$$\nabla_t \times H^{(0)}(x,y,z) - i\beta_\mu(z) \mathbf{e}_z \times H^{(0)}(x,y,z) = i \omega \varepsilon_0 \hat{\varepsilon}_r(x,y,z) E^{(0)}(x,y,z). \quad (2-7)$$

On the other hand, electric and magnetic fields in the actual waveguide $\{E(x,y,z), H(x,y,z)\}$ satisfies the following Maxwell equations:

$$\nabla_t \times E(x,y,z) + \mathbf{e}_z \times \frac{\partial E(x,y,z)}{\partial z} = -i \omega \mu_0 H(x,y,z), \quad (2-8)$$

$$\nabla_t \times H(x,y,z) + \mathbf{e}_z \times \frac{\partial H(x,y,z)}{\partial z} = i \omega \left\{ \varepsilon_0 \hat{\varepsilon}_r(x,y,z) E(x,y,z) - \Delta P(x,y,z) \right\}, \quad (2-9)$$

where $\Delta P(x,y,z)$ is a perturbation polarization originating from the nonlinear susceptibility. Subtracting the scalar product of $E^{(0)}(x,y,z)^*$ and Eq. (2-9) from the scalar product of $H(x,y,z)$ and complex conjugate of Eq. (2-6), and also the scalar product of $E(x,y,z)$ and complex conjugate of Eq. (2-7) from the scalar product of $H^{(0)}(x,y,z)^*$ and Eq. (2-8), and adding the resulting equations, we can obtain the following equation:

$$\begin{aligned}
 & \nabla_t \cdot \left(\mathbf{E} \times \mathbf{H}_t^{(0)*} + \mathbf{E}_t^{(0)*} \times \mathbf{H} \right) \\
 & + \mathbf{e}_z \cdot \left\{ \frac{\partial \mathbf{E}_t}{\partial z} \times \mathbf{H}_t^{(0)*} + \mathbf{E}_t^{(0)*} \times \frac{\partial \mathbf{H}_t}{\partial z} - i \beta_\mu(z) \left(\mathbf{E}_t \times \mathbf{H}_t^{(0)*} + \mathbf{E}_t^{(0)*} \times \mathbf{H}_t \right) \right\} \\
 & = -i \omega \mathbf{E}^{(0)*} \cdot \Delta \mathbf{P} , \tag{2-10}
 \end{aligned}$$

where argument (x, y, z) was omitted for simplicity. Considering that for a guided mode the electric field is zero at an infinitely far point and that periodic boundary condition can be used for a radiation mode, integral of those terms including ∇_t over the xy plane is zero. Therefore, we can obtain by integrating Eq. (2-10) over xy plane:

$$\begin{aligned}
 & \iint \mathbf{e}_z \cdot \left\{ \frac{\partial \mathbf{E}_t}{\partial z} \times \mathbf{H}_t^{(0)*} + \mathbf{E}_t^{(0)*} \times \frac{\partial \mathbf{H}_t}{\partial z} - i \beta_\mu(z) \left(\mathbf{E}_t \times \mathbf{H}_t^{(0)*} + \mathbf{E}_t^{(0)*} \times \mathbf{H}_t \right) \right\} dx dy \\
 & = -i \omega \iint \mathbf{E}^{(0)*} \cdot \Delta \mathbf{P} dx dy . \tag{2-11}
 \end{aligned}$$

$\{\mathbf{E}_t(x, y, z), \mathbf{H}_t(x, y, z)\}$ can be expanded by the local normal modes $\{\mathbf{E}_v(x, y, z), \mathbf{H}_v(x, y, z)\}$ as follows [38]:

$$\mathbf{E}_t(x, y, z) = \sum_v a_v(z) \mathbf{E}_v(x, y, z) \exp \left[-i \int_0^z \beta_v(\zeta) d\zeta \right] , \tag{2-12}$$

$$\mathbf{H}_t(x, y, z) = \sum_v a_v(z) \mathbf{H}_v(x, y, z) \exp \left[-i \int_0^z \beta_v(\zeta) d\zeta \right] , \tag{2-13}$$

where \sum includes summation over discrete modes and integral over continuous modes, i.e., $\int dv$ [41]. $a_v(z)$ denotes normalized modal field amplitude. The transverse modal fields satisfies the following orthonormal relation [41]:

$$\begin{aligned}
 & \frac{1}{4} \iint \mathbf{e}_z \cdot \left[\mathbf{E}_v(x, y, z) \times \mathbf{H}_{\mu t}(x, y, z)^* + \mathbf{E}_{\mu t}(x, y, z)^* \times \mathbf{H}_v(x, y, z) \right] dx dy \\
 & = \begin{cases} \pm \delta_{\mu v} & (\text{discrete mode}) \\ \pm \delta(\beta_\mu(z) - \beta_v(z)) & (\text{continuous mode}) \end{cases} \tag{2-14}
 \end{aligned}$$

The sign of the right hand side of Eq. (2-14) is defined as same as the sign of $\beta_m(z) = \beta_n(z)$. Substituting Eqs. (2-12) and (2-13) into Eq. (2-11) and using the orthonormal relation Eq. (2-14), we obtain

$$\begin{aligned}
 \pm \frac{d}{dz} a_\mu(z) & = -\frac{1}{4} \sum_v \left\{ a_v(z) \exp \left[-i \int_0^z \{\beta_v(\zeta) - \beta_\mu(\zeta)\} d\zeta \right] \right. \\
 & \quad \cdot \left. \iint \mathbf{e}_z \cdot \left(\frac{\partial \mathbf{E}_{vt}}{\partial z} \times \mathbf{H}_{\mu t}^* + \mathbf{E}_{\mu t}^* \times \frac{\partial \mathbf{H}_{vt}}{\partial z} \right) dx dy \right\} \\
 & \quad - i \frac{\omega}{4} \exp \left[i \int_0^z \beta_\mu(\zeta) d\zeta \right] \iint \mathbf{E}_{\mu t}^* \cdot \Delta \mathbf{P} dx dy , \tag{2-15}
 \end{aligned}$$

which is a general expression of the nonlinear coupled mode equation with the LNME.

2.4 Derivation of Nonlinear Coupled Mode Equations for SHG

In the following discussion of nonlinear coupled mode equations, we use superscripts f and s for the fundamental and second harmonic components, respectively. To simplify the discussion, we assume that the modal field profiles vary slowly along z , and the z -derivatives of them can be ignored. The perturbation polarization ΔP^f and ΔP^s can be written as

$$\Delta P^f = 2 \tilde{d} E^f E^s \quad (2-16)$$

and

$$\Delta P^s = \tilde{d} E^f E^f, \quad (2-17)$$

where \tilde{d} is the second order nonlinear optical coefficient tensor. Using Eqs. (2-12)(2-13)(2-16)(2-17), we can derive from Eq. (2-15) nonlinear coupled mode equations for the fundamental and second harmonic modal amplitudes:

$$\frac{d a_\mu^f(z)}{dz} = -i \frac{\omega^f}{4} \sum_{v1} \sum_{v2} \left\{ a_{v1}^f(z) a_{v2}^s(z) \exp \left[-i \int_0^z \left\{ \beta_{v2}^s(\zeta) - \beta_{v1}^f(\zeta) - \beta_\mu^f(\zeta) \right\} d\zeta \right] \right. \\ \left. \cdot \iint E_{\mu}^{f*} \cdot \tilde{d}(\omega^f; -\omega^f, \omega^s) E_{v1}^{f*} E_{v2}^s dx dy \right\}, \quad (2-18)$$

$$\frac{d a_\mu^s(z)}{dz} = -i \frac{\omega^s}{4} \sum_{v1} \sum_{v2} \left\{ a_{v1}^f(z) a_{v2}^f(z) \exp \left[-i \int_0^z \left\{ \beta_{v1}^f(\zeta) + \beta_{v2}^f(\zeta) - \beta_\mu^s(\zeta) \right\} d\zeta \right] \right. \\ \left. \cdot \iint E_{\mu}^{s*} \cdot \tilde{d}(\omega^s; \omega^f, \omega^f) E_{v1}^f E_{v2}^f dx dy \right\}. \quad (2-19)$$

A more practical expression of these equations convenient for the calculation of the second harmonic generation efficiency can be derived as follows. We assume that the dielectric axes of the guide and clad materials coincide with the waveguide coordinate frame, that is, the thickness, the width, and the longitudinal direction of the waveguide. Therefore, the modal fields have a principal component in the thickness or width direction [42][43], and hence neglecting other components is a good approximation. Vectors and tensors in Eqs. (2-18) and (2-19) are reduced to scalars by approximating the modal field vector to a scalar as follows:

$$E_{\mu x}^m = c_\mu^m g_\mu^m(x, y, z) \quad (m=f, s), \quad (2-20)$$

where function $g_\mu^m(x, y, z)$ is a field profile of an arbitrary scale, and c_μ^m a normalization factor. This normalization factor can be expressed approximately (see Appendix 2.A) as follows:

$$\{ c_\mu^m(z) \}^2 = 2 \frac{1}{n_{\text{eff}\mu}^m(z)} \sqrt{\frac{\mu_0}{\epsilon_0}} \frac{1}{\iint |g_\mu^m(x, y, z)|^2 dx dy} \quad (m=f, s). \quad (2-21)$$

The effective refractive index $n_{\text{eff}\mu}^m(z)$ is related to the local propagation coefficient $\beta_\mu^m(z)$ through the well-known formula

$$n_{\text{eff}\mu}^m(z) = \frac{\beta_\mu^m(z)}{k_0^m} \quad (m=f, s), \quad (2-22)$$

where $k_0^m = \omega^m/c_0$ is the wavenumber in vacuum and c_0 the velocity of light in vacuum. In this context we

assume that $\beta_\mu^m(z)$ is real. Under this approximation, the second order nonlinear optical coefficient tensor \tilde{d} reduces to a scalar d . For example, if both the fundamental and second harmonic modes are principally x -polarized, then $d=d_{11}=d_{xxx}$. In addition, we make the single mode approximation, i.e., there is only one mode for each of the fundamental and second harmonic. The validity of this approximation will be discussed in Appendix 2.C. Thus, in the following discussion, we omit the mode index numbers, i.e., v_1 , v_2 , and μ . Substituting Eq. (2-21) into Eqs. (2-18) and (2-19) under the single mode assumption, we obtain

$$\begin{aligned} \frac{d}{dz} a^f(z) = & -i \sqrt{2} \omega^f \left(\frac{\mu_0}{\epsilon_0} \right)^{\frac{3}{4}} a^f(z)^* a^g(z) \exp[-i \Delta \beta_0 z] \\ & \cdot \frac{\exp \left[-i \int_0^z \left\{ \beta^g(\zeta) - 2\beta^f(\zeta) - \Delta \beta_0 \right\} d\zeta \right]}{n_{\text{eff}}^f(z) \sqrt{n_{\text{eff}}^g(z)}} \\ & \cdot \frac{\iint d(x,y,z) \{g^f(x,y,z)\}^* \{g^g(x,y,z)\} dx dy}{\sqrt{\left\{ \iint |g^g(x,y,z)|^2 dx dy \right\} \left\{ \iint |g^f(x,y,z)|^2 dx dy \right\}^2}}, \end{aligned} \quad (2-23)$$

and

$$\begin{aligned} \frac{d}{dz} a^g(z) = & -i \sqrt{2} \omega^g \left(\frac{\mu_0}{\epsilon_0} \right)^{\frac{3}{4}} a^f(z)^2 \exp[i \Delta \beta_0 z] \\ & \cdot \frac{\exp \left[-i \int_0^z \left\{ 2\beta^f(\zeta) - \beta^g(\zeta) + \Delta \beta_0 \right\} d\zeta \right]}{n_{\text{eff}}^g(z) \sqrt{n_{\text{eff}}^f(z)}} \\ & \cdot \frac{\iint d(x,y,z) \{g^g(x,y,z)\}^* \{g^f(x,y,z)\}^2 dx dy}{\sqrt{\left\{ \iint |g^g(x,y,z)|^2 dx dy \right\} \left\{ \iint |g^f(x,y,z)|^2 dx dy \right\}^2}}, \end{aligned} \quad (2-24)$$

where the relation $\omega^g=2\omega^f$ was used. The averaged propagation coefficient mismatch $\Delta \beta_0$ is defined as:

$$\Delta \beta_0 = \frac{1}{\Lambda} \int_z^{z+\Lambda} \left\{ \beta^g(\zeta) - 2\beta^f(\zeta) \right\} d\zeta, \quad (2-25)$$

where Λ is the period of the periodic waveguide structure such as corrugation or domain inversion. Let us define terms with the period of Λ in the right hand side of Eqs. (2-23) and (2-24) as follows:

$$\begin{aligned} f(z) \equiv & \frac{\exp \left[-i \int_0^z \left\{ 2\beta^f(\zeta) - \beta^g(\zeta) + \Delta \beta_0 \right\} d\zeta \right]}{n_{\text{eff}}^g(z) \sqrt{n_{\text{eff}}^f(z)}} \\ & \cdot \frac{\iint d(x,y,z) \{g^g(x,y,z)\}^* \{g^f(x,y,z)\}^2 dx dy}{\sqrt{\left\{ \iint |g^g(x,y,z)|^2 dx dy \right\} \left\{ \iint |g^f(x,y,z)|^2 dx dy \right\}^2}}. \end{aligned} \quad (2-26)$$

Using $f(z)$, Eqs. (2-23) and (2-24) can be expressed as follows:

$$\frac{d}{dz} a(z) = -i \sqrt{2} \omega^f \left(\frac{\mu_0}{\epsilon_0} \right)^{\frac{3}{4}} a^f(z)^* a^s(z) \exp[-i \Delta \beta_0 z] f^*(z), \quad (2-27)$$

$$\frac{d}{dz} a^s(z) = -i \sqrt{2} \omega^f \left(\frac{\mu_0}{\epsilon_0} \right)^{\frac{3}{4}} a^f(z)^2 \exp[i \Delta \beta_0 z] f(z). \quad (2-28)$$

$f(z)$ can be expanded into a Fourier series as follows:

$$f(z) = \sum_{q=-\infty}^{+\infty} F_q \exp[iqKz], \quad (2-29)$$

where F_q is the q -th order Fourier coefficient defined as:

$$F_q = \frac{1}{\Lambda} \int_0^{\Lambda} f(z) \exp[-iqKz] dz, \quad (2-30)$$

and $K = 2\pi/\Lambda$ is the wavenumber of the periodic structure. Using Eq. (2-29), we can obtain from Eqs. (2-23) and (2-24)

$$\frac{d}{dz} a(z) = -i \sqrt{2} \omega^f \left(\frac{\mu_0}{\epsilon_0} \right)^{\frac{3}{4}} a^f(z)^* a^s(z) \sum_{q=-\infty}^{+\infty} F_q^* \exp[-i \Delta \beta_q z] \quad (2-31)$$

and

$$\frac{d}{dz} a^s(z) = -i \sqrt{2} \omega^f \left(\frac{\mu_0}{\epsilon_0} \right)^{\frac{3}{4}} \{a^f(z)\}^2 \sum_{q=-\infty}^{+\infty} F_q \exp[i \Delta \beta_q z], \quad (2-32)$$

where $\Delta \beta_q = \Delta \beta_0 + qK$ is propagation coefficient mismatch for q -th order diffraction. From these equations we can easily see that QPM is achieved when $\Delta \beta_q$ is zero for some value of integer q .

2.5 SHG Efficiency and Effective SHG Coefficient

If we employ the no pump depletion approximation, the fundamental amplitude can be approximated to a constant $a^f(z) = a^f$, and Eq. (2-32) can be easily integrated with an initial condition of $a^s(0) = 0$ resulting in the following expression:

$$a^s(z) = \sqrt{2} \omega^f \left(\frac{\mu_0}{\epsilon_0} \right)^{\frac{3}{4}} a^{f^2} \sum_{q=-\infty}^{+\infty} F_q \frac{\exp[i \Delta \beta_q z] - 1}{\Delta \beta_q}. \quad (2-33)$$

Assuming that $\Delta \beta_q$ is much smaller for some order $q = q_0$ than for other orders, the terms other than the $q = q_0$ term of the summation in Eq. (2-28) can be ignored as follows:

$$a^s(z) = \sqrt{2} \omega^f \left(\frac{\mu_0}{\epsilon_0} \right)^{\frac{3}{4}} a^{f^2} F_{q_0} \frac{\exp[i \Delta \beta_{q_0} z] - 1}{\Delta \beta_{q_0}}, \quad (2-34)$$

where $\Delta \beta_{q_0}$ is the residual phase coefficient mismatch. From Eq. (2-34), the second harmonic power flow at z is expressed as follows:

$$\begin{aligned} P^s(z) &\equiv |a^s(z)|^2 \\ &= 2 \omega^{f^2} \left(\frac{\mu_0}{\epsilon_0} \right)^{\frac{3}{2}} |a^f|^4 |F_{q_0}|^2 \left| \frac{\exp[i \Delta \beta_{q_0} z] - 1}{\Delta \beta_{q_0} z} \right|^2 z^2 \\ &= 2 \omega^{f^2} \left(\frac{\mu_0}{\epsilon_0} \right)^{\frac{3}{2}} P^{f^2} |F_{q_0}|^2 \text{sinc}^2 \left(\frac{\Delta \beta_{q_0} z}{2} \right) z^2. \end{aligned} \quad (2-35)$$

Thus, the second harmonic generation efficiency η for a device of length l can be obtained as follows:

$$\begin{aligned}\eta &\equiv \frac{P^s(l)}{P^f} \\ &= 2 \omega^f{}^2 \left(\frac{\mu_0}{\epsilon_0} \right)^{\frac{3}{2}} |F_{qd}|^2 \operatorname{sinc}^2 \left(\frac{\Delta \beta l}{2} \right) P^f l^2 .\end{aligned}\quad (2-36)$$

It may be convenient to introduce an effective SHG coefficient d_{eff} which is defined as follows:

$$d_{\text{eff}} \equiv F_{q0} \sqrt{S_{\text{eff}} n_{\text{eff}}^f n_{\text{eff}}^s} . \quad (2-37)$$

The averaged effective waveguide cross section of the waveguide is defined as:

$$\overline{S_{\text{eff}}} \equiv \frac{1}{\Lambda} \int \int \int_{z=0}^{z=\Lambda} S_{\text{eff}}(z) dx dy dz , \quad (2-38)$$

where $S_{\text{eff}}(z)$ is the local effective cross section of the waveguide (see Appendix 2.B for the definition of the effective cross section). The averaged effective refractive indices $\overline{n_{\text{eff}}^f}$ and $\overline{n_{\text{eff}}^s}$ are defined as follows:

$$\overline{n_{\text{eff}}^m} \equiv \frac{1}{\Lambda} \int_{z=0}^{z=\Lambda} n_{\text{eff}}^m(\zeta) d\zeta \quad (m=f,s) . \quad (2-39)$$

Using these definitions, Eq. (2-36) can be expressed as:

$$\eta = 2 \omega^f{}^2 \left(\frac{\mu_0}{\epsilon_0} \right)^{\frac{3}{2}} \frac{|d_{\text{eff}}|^2}{n_{\text{eff}}^f{}^2 n_{\text{eff}}^s} \operatorname{sinc}^2 \left(\frac{\Delta \beta l}{2} \right) \frac{P^f}{\overline{S_{\text{eff}}}} l^2 \quad (2-40)$$

which is the same as the conventional formulation [44] except that some effective values, i.e., d_{eff} , $\overline{n_{\text{eff}}^f}$, $\overline{n_{\text{eff}}^s}$, and $\overline{S_{\text{eff}}}$ is used in place of the bulk values. Hence, we can define the following expression:

$$\text{FOM} \equiv \frac{|d_{\text{eff}}|^2}{n_{\text{eff}}^f{}^2 n_{\text{eff}}^s} = |F_{qd}|^2 \overline{S_{\text{eff}}} \quad (2-41)$$

as an expanded (or generalized) figure of merit including both material factor and phase matching method factor.

The second harmonic generation efficiency considering depletion of the fundamental can be derived through the following procedure [36][45]. Equations (2-31) and (2-32) can be expressed as follows:

$$\begin{aligned}\frac{d}{dz} a^f(z) &= -i a^f(z)^* a^s(z) \sum_{q=-\infty}^{+\infty} \kappa_q^* \exp[-i \Delta \beta_q z] \\ &\approx -i a^f(z)^* a^s(z) \kappa_{q0}^* \exp[-i \Delta \beta_{q0} z]\end{aligned}\quad (2-42)$$

$$\begin{aligned}\frac{d}{dz} a^s(z) &= -i \{a^f(z)\}^2 \sum_{q=-\infty}^{+\infty} \kappa_q \exp[i \Delta \beta_q z] \\ &\approx -i \{a^f(z)\}^2 \kappa_{q0} \exp[i \Delta \beta_{q0} z] ,\end{aligned}\quad (2-43)$$

where nonlinear coupling coefficient κ_q is defined as:

$$\begin{aligned}\kappa_q &\equiv \sqrt{2} \omega^f \left(\frac{\mu_0}{\epsilon_0} \right)^{\frac{3}{4}} F_q \\ &= \sqrt{2} \omega^f \left(\frac{\mu_0}{\epsilon_0} \right)^{\frac{3}{4}} \frac{d_{\text{eff}}}{\sqrt{S_{\text{eff}} n_{\text{eff}}^f n_{\text{eff}}^s}} .\end{aligned}\quad (2-44)$$

Equations (2-42) and (2-43) can be solved and the resulting SHG efficiency is [36][45]

$$\eta = \gamma \operatorname{sn}^2 \left[\frac{\kappa_{q0} a^f(0) l}{\sqrt{\gamma}} ; \gamma \right] \quad (2-45)$$

$$\gamma = \left\{ \frac{2 \kappa_{q0} a^f(0)}{\sqrt{[2 \kappa_{q0} a^f(0)]^2 + \left(\frac{\Delta\beta_{q0}}{2}\right)^2 + \left(\frac{\Delta\beta_{q0}}{2}\right)^2}} \right\}^2 \quad (2-46)$$

where $\text{sn}[\zeta; \gamma]$ is the Jacobian elliptic function defined as follows:

$$\zeta = \int_0^\xi \frac{d\xi''}{\sqrt{(1 - \xi''^2)(1 - \gamma^2 \xi''^2)}} , \quad \xi = \text{sn}[\zeta; \gamma] \quad (2-47)$$

If the phase matching condition is exactly satisfied, i.e., $\Delta\beta_{q0} = 0$, Eq. (2-45) can be reduced to

$$\eta = \tanh^2[\kappa_{q0} a^f(0) l] \quad (2-48)$$

which is an asymptotic approaching 1 with increasing $\kappa_{q0} a^f(0) l$.

2.6 Concluding Remarks

In this chapter, general nonlinear coupled mode equations based on the local normal mode expansion have been derived for the first time. In addition, nonlinear coupled mode equations for quasi phase matching SHG and practical expressions of SHG efficiency, effective SHG coefficient, and a general form of figure of merit have been shown.

Appendix 2.A Normalization Factor of a Field Profile Function

For a TE mode in a planar waveguide, the normalization factor can be obtained easily and rigorously. The magnetic field can be expressed as follows [41][44] :

$$H_y^m = \frac{\beta^m}{\omega^m \mu_0} E_x^m \quad (m=f,s) . \quad (2-A1)$$

This linear relation gives the normalization factor Eq. (2-21) through substitution of Eqs. (2-20) and (2-A1) into Eq. (2-14). For a TM mode in a planar waveguide, the derivation is a little more complicated. The electric field of a TM mode in a planar waveguide can be expressed as follows [38][41] :

$$E_x^m = \frac{\beta^m}{\omega^m \epsilon_0 (\hat{\epsilon}_r)_{xx}} H_y^m \quad (m=f,s) , \quad (2-A2)$$

i.e., the electric field has discontinuity at the boundary of the core and clad because of the discontinuity of the dielectric constant. If the mode is far from cut off, the evanescent field in the clad is negligible and we can approximate the normalization factor by Eq. (2-21).

For a channel waveguide, it is more complicated, but we can go with the same approximation. The magnetic field of TE_x mode can be expressed as [43]:

$$H_y^m = \frac{1}{\omega^m \mu_0 \beta^m} \left[\left(k_0^2 (\hat{\epsilon}_r)_{xx} + \frac{\partial^2}{\partial y^2} \right) E_x^m - \frac{\partial^2}{\partial x \partial y} E_y^m \right] \quad (m=f,s) , \quad (2-A3)$$

which can be transformed in the core as:

$$H_y^m = \frac{\left\{ k_0^2 n_x^{m2} - k_y^2 - \frac{n_x^{m2}}{n_y^{m2}} k_x^2 \right\}}{\omega^m \mu_0 \beta^m} \frac{k_0^2 n_y^{m2}}{\left\{ k_0^2 n_y^{m2} - k_x^2 \right\}} E_x^m \quad (m=f,s) . \quad (2-A4)$$

For isotropic media, this equation can be reduced to [42]:

$$H_y^m = \frac{\omega^m \epsilon_0 n^{m2} \beta^m}{k_0^2 n^{m2} - k_x^2} E_x^m \quad (m=f,s) . \quad (2-A5)$$

Under the assumption of far-from-cut-off, the transverse wavenumber k_x^2 is much smaller than the total wavenumber $k_0^2 n_y^{m2}$, and the following approximation can be used:

$$\beta^{m2} \approx k_0^2 n_x^{m2} - k_y^2 - \frac{n_x^{m2}}{n_y^{m2}} k_x^2 \quad (m=f,s) . \quad (2-A6)$$

In addition, the evanescent field is negligibly small, thus Eq. (2-A4) can be approximated to Eq. (2-21). The far-from-cut-off assumption is also the fundamental assumption for the Marcatili's method [42].

Appendix 2.B A Discussion on Definitions of the Effective Cross Section of the Waveguide

In Ref.[36], the interaction cross section

$$S_{\text{int}}(z) \equiv \frac{\left\{ \iint |g^i(x,y,z)|^2 dx dy \right\} \left\{ \iint |g^f(x,y,z)|^2 dx dy \right\}^2}{\left\{ \iint \{g^i(x,y,z)\}^* \{g^f(x,y,z)\}^2 dx dy \right\}^2} \quad (2-B1)$$

is used as the effective cross section $S_{\text{eff}}(z)$. This definition has an advantage that the value can be determined uniquely. However, in the context of Eq. (2-40), the meaning of the term P^f/S_{eff} and the effective SHG coefficient d_{eff} is not clear. We have introduced d_{eff} as a kind of figure of merit considering both the material nonlinearity and the phase-matching method. Though, in this definition of $S_{\text{eff}}(z)$, the overlap integral factor originating from the choice of the fundamental and the second harmonic mode is included not in d_{eff} but in P^f/S_{eff} . For example, if the fundamental and/or the second harmonic is higher order mode, $S_{\text{int}}(z)$ has a larger value than the actual waveguide cross section.

Therefore, we propose using the effective cross section for fundamental $S_{\text{eff}}^f(z)$ as $S_{\text{eff}}(z)$. This definition has advantages that the meaning of the term P^f/S_{eff} is clearly the fundamental power density, and that d_{eff} gives the figure of merit. However, there is a disadvantage that the definition of the effective cross section for fundamental is not unique. For a TE and a TM mode of a three-layer (single guiding layer) planar waveguide

shown in Fig.2-1, the following definitions of the effective waveguide thickness are used [41]:

$$T_{\text{eff}} \equiv \begin{cases} T + \frac{1}{\gamma_2} + \frac{1}{\gamma_3} & \text{(for a TE mode)} \\ T + \frac{1}{q_2^2 \gamma_2} + \frac{1}{q_3^2 \gamma_3} & \text{(for a TM mode)} \end{cases} \quad (2-B2)$$

where γ_2 and γ_3 are the extinction coefficient of evanescent field in the clad layers 2 and 3, respectively, and q_2 and q_3 are defined as follows:

$$q_j^2 \equiv \left(\frac{n_{\text{eff}}}{n_1} \right)^2 + \left(\frac{n_{\text{eff}}}{n_j} \right)^2 - 1 \quad (j=2,3) \quad (2-B3)$$

This effective thickness T_{eff} means that the actual guided power equals the power guided through a waveguide of T_{eff} wide with a uniform power density distribution of half of the peak power density in the actual waveguide. The factor 1/2 can be interpreted to originate from averaging. This definition may be easily expanded to a simple channel waveguide shown in Fig.2-2 for a TE-like mode as follows:

$$S_{\text{eff}} \equiv \left(T + \frac{1}{\gamma_2} + \frac{1}{\gamma_3} \right) \left(W + \frac{1}{q_4^2 \gamma_4} + \frac{1}{q_5^2 \gamma_5} \right) \quad (2-B4)$$

This effective cross section S_{eff} means that the actual guided power equals the power guided through a waveguide of S_{eff} in cross sectional area with a uniform power density distribution of a quarter of the peak power density in the actual waveguide. The factor 1/4 can be interpreted to originate from averaging over two directions. On the other hand, there is no such easily understandable definition for a four or more layer waveguide, because the half or the quarter of the peak power density in the actual waveguide can no more be interpreted to originate from averaging.

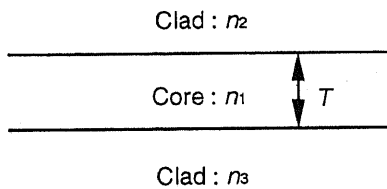


Fig.2-1 Model of planar waveguide used for calculation of effective thickness.

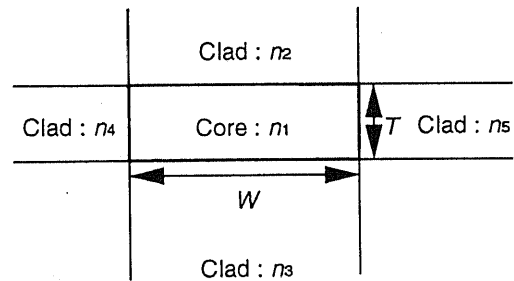


Fig.2-2 Model of channel waveguide used for calculation of effective cross section.

Appendix 2.C A Discussion on the Validity of the Single Mode Approximation

The single mode approximation, i.e., the adiabatic approximation, used in this and next chapters is valid when the variation of the field along the longitudinal (z) direction is small. This condition can be expressed in some ways.

The first expression is that the "taper" of the waveguide is small. This is expressed as:

$$|\theta_{\max}| \ll 1 \quad (2-C1)$$

where θ_{\max} is the maximum angle between the corrugated core-clad boundary and the z direction. In a sinusoidally corrugated waveguide shown in Fig.3-1, θ_{\max} is expressed as:

$$\theta_{\max} = W_0 D \frac{2\pi}{\Lambda} \quad (2-C2)$$

where W_0 is the averaged waveguide width, D the degree of modulation in the waveguide width, Λ the period of the corrugation. Substituting Eq.(2-C2) into (2-C1), the following condition is obtained:

$$D \ll \frac{\Lambda}{2\pi W_0} \quad (2-C3)$$

For example, the right-hand side of this inequality equals 0.034 for a waveguide of $3\mu\text{m}$ wide with the corrugation period of $0.65\mu\text{m}$, which is the phase matching value of an MNA SHG device.

This condition is the most strict one. A more gentle condition may be expressed as

$$\left| a_\mu \left(z = \frac{\Lambda}{2} \right) \right| \ll \left| a_\nu(z=0) \right|, \quad (2-C4)$$

where mode ν is the initial mode, that is, the only mode existing at $z=0$ where the waveguide is narrowest. Here it is assumed that the waveguide is widest at $z=\Lambda/2$. This means that the *local* energy transfer must be negligibly small. The left-hand side of (2-C4) can be obtained as follows. The linear coupling coefficient $\kappa_{\mu\nu}^L$ from mode ν to μ is defined as

$$\begin{aligned} \kappa_{\mu\nu}^L &\equiv -\frac{1}{4} \iint \mathbf{e}_z \cdot \left(\frac{\partial \mathbf{E}_{\nu t}}{\partial z} \times \mathbf{H}_{\mu t}^* + \mathbf{E}_{\mu t}^* \times \frac{\partial \mathbf{H}_{\nu t}}{\partial z} \right) dx dy \\ &= \frac{\omega \epsilon_0}{4(\beta_\mu^* - \beta_\nu)} \iint \frac{\partial n^2}{\partial z} \mathbf{E}_\nu \cdot \mathbf{E}_\mu^* dx dy \end{aligned} \quad (2-C5)$$

The z -derivative of n^2 is transformed as [38]

$$\frac{\partial n^2}{\partial z} = (n_{\text{core}}^2 - n_{\text{clad}}^2) \frac{\partial W(z)}{\partial z} \delta(x, y : \Gamma(z)), \quad (2-C6)$$

where δ is Dirac's delta function which is not 0 for (x, y) included to Γ , i.e. the side boundaries between the core and clad. Neglecting the nonlinear coupling term, the coupled mode equation Eq.(2-15) is integrated as:

$$\begin{aligned} a_\mu \left(\frac{\Lambda}{2} \right) &\approx -\frac{1}{4} \int \left\{ a_\nu(0) \exp \left[-i \int_0^z (\beta_\nu(\zeta) - \beta_\mu(\zeta)) d\zeta \right] \cdot \iint \mathbf{e}_z \cdot \left(\frac{\partial \mathbf{E}_{\nu t}}{\partial z} \times \mathbf{H}_{\mu t}^* + \mathbf{E}_{\mu t}^* \times \frac{\partial \mathbf{H}_{\nu t}}{\partial z} \right) dx dy \right\} \\ &\approx a_\nu(0) \frac{W\left(\frac{\Lambda}{2}\right) - W(0)}{(n_{\text{eff}\mu}^* - n_{\text{eff}\nu})} \frac{(n_{\text{core}}^2 - n_{\text{clad}}^2)}{\sqrt{n_{\text{eff}\mu}^* n_{\text{eff}\nu}}} \frac{(g_{x\mu}^* g_{x\nu})_{\text{core side boundary}}}{\sqrt{\int |g_{x\mu}|^2 dx \int |g_{x\nu}|^2 dx}} \frac{\int g_{y\mu}^* g_{y\nu} dy}{\sqrt{\int |g_{y\mu}|^2 dy \int |g_{y\nu}|^2 dy}} \end{aligned} \quad (2-C7)$$

where the following assumptions are made: the variable separation can be applied to the modal field profile $g_\mu(x, y, z)$ and $g_\nu(x, y, z)$ as

$$\begin{aligned} g_\mu(x, y, z) &= g_{x\mu}(x, z) g_{y\mu}(y) \\ g_\nu(x, y, z) &= g_{x\nu}(x, z) g_{y\nu}(y), \end{aligned} \quad (2-C8)$$

and the variation of effective refractive indices and modal fields at the core-clad boundary along the longitudinal

position z is not large and can be approximated with constants. The order of magnitude of the right-hand side of Eq.(2-C6) can be estimated as follows. The terms composed of the refractive indices and effective refractive indices are the order of 1. The last term composed of $g_{y\mu}$ and $g_{y\nu}$ is less than or equal to 1. $W(\Lambda/2)-W(0)$ is the order of DW_0 , where D is the degree of width modulation and W_0 the averaged width. $\sqrt{\int |g_{x\mu}|^2 dx \int |g_{x\nu}|^2 dx}$ is the order of W_0 when the order of maximum value of the field profile $g_{x\mu}$ and $g_{x\nu}$ is 1. $g_{x\mu}^* g_{x\nu}$ is the order of 0.1 or less for a waveguide with rather strong confinement. Hence, the amplitude $a_\mu(\Lambda/2)$ is smaller than the amplitude of the initial mode by one or more orders of magnitude as far as D is small. Therefore, the single mode approximation in the LNME may be valid for a small value of D , e.g. the order of 0.1. Whether this condition is appropriate or not should be examined with a multimode theory or a numerical method.

In addition, there is another condition for the single mode approximation as follows [40] :

$$|\kappa_{\mu\nu q}^L| \ll \left| \beta_\mu - \beta_\nu + \frac{2\pi}{\Lambda} q \right|, \quad (2-C9)$$

where $\kappa_{\mu\nu q}^L$ is the q -th order Fourier coefficient of $\kappa_{\mu\nu}^L$. This condition means that the energy transfer along a rather long distance, compared with the corrugation period, is negligible. However, this is not satisfied for a waveguide in which phase matched radiation modes exist. Strictly speaking, therefore, the single mode approximation is not valid for such a periodic waveguide. In spite, this mode coupling is a 'long range' one, and can be treated as a loss to the mode ν in the nonlinear coupled mode equations. This will be described in detail in Appendix 6.A. Hence, the validity of the single mode approximation is not affected by whether Eq.(2-C9) is satisfied or not.

Chapter 3

Analyses on Some Types of Quasi Phase Matching SHG Devices

3.1 Introductory Remarks

In the previous chapter, general and practical expressions of SHG efficiency and effective SHG coefficient have been derived based on the local normal mode expansion (LNME). In this chapter, analyses on some types of quasi phase matching (QPM) SHG devices, i.e., a device with corrugation and a device with periodic domain inversion, are presented. Analytical expressions of SHG efficiency and effective SHG coefficient under strong light confinement approximation, which is useful for rough estimation of a device performance, are derived for each type of device. In addition, numerically calculated results are shown and compared with those obtained by the conventional ideal normal mode expansion (INME).

In section 3.2, a device with corrugation is analyzed, for which a corrugated channel waveguide device based on an organic MNA is an example.

In section 3.3, a device with periodic domain inversion is analyzed, for which channel waveguide devices based on ferroelectrics LiNbO_3 and LiTaO_3 are examples.

In section 3.4, the summary is presented.

3.2 Quasi Phase Matching SHG Devices with Corrugation

In a sinusoidally corrugated waveguide, QPM is achieved through periodic modulation of the field distribution, effective refractive index (propagation coefficient) and nonlinearity. Although some analyses were proposed [21][31][34], these used the conventional INME and only consider the modulation of the effective index and/or nonlinearity. Therefore, the LNME, which can treat the modulation of the field profile easily, is expected to give different results from the INME.

3.2.1 Analytical Expression in the Limit of Strong Confinement

If the fundamental and second harmonic modes are far from cut-off and strongly confined, we can derive approximated analytical expression of SHG efficiency η and effective SHG coefficient d_{eff} . Consider a channel waveguide with the structure shown in Fig.3-1. In the strong confinement limit [46], the modal field profile function of the lowest order mode can be written as follows:

$$g^f(x, y, z) = g^s(x, y, z) = \begin{cases} \cos\left(\frac{\pi}{W(z)}x\right) \sin\left(\frac{\pi}{T}y\right) & \left(-\frac{W(z)}{2} \leq x \leq \frac{W(z)}{2}, 0 \leq y \leq T\right) \\ 0 & (\text{otherwise}) \end{cases} \quad (3-1)$$

Substituting this into Eq. (2-26) and approximating the effective refractive index to the refractive index of the core material, we can obtain

$$\begin{aligned} f(z) &= \left(\frac{8\sqrt{2}}{3\pi}\right)^2 d \frac{1}{n_{\text{core}}^2 \sqrt{n_{\text{core}}} \sqrt{W(z)} T} \\ &\approx \left(\frac{8\sqrt{2}}{3\pi}\right)^2 d \frac{1}{n_{\text{core}}^2 \sqrt{n_{\text{core}}} \sqrt{W_0} T} \left(1 - \frac{D}{2} \cos Kz\right), \end{aligned} \quad (3-2)$$

where local width of the waveguide is defined as $W(z) = W_0 (1 + D \cos Kz)$. Therefore the -1st order Fourier coefficient F_{-1} can be expressed as follows:

$$F_{-1} = \frac{32D}{9\pi^2} d \frac{1}{n_{\text{core}}^2 \sqrt{n_{\text{core}}} \sqrt{W_0} T} \quad (3-3)$$

Substituting Eq. (3-3) into Eq. (2-37), the effective SHG coefficient can be obtained as:

$$d_{\text{eff}} = \frac{32D}{9\pi^2} d \quad (3-4)$$

which is independent of averaged width W_0 and thickness T . This feature is different from the INME result [31]

¹. The SHG efficiency can be expressed as:

$$\eta = \frac{2048}{81\pi^4} \omega^2 \left(\frac{\mu_0}{\epsilon_0}\right)^{\frac{3}{2}} \frac{D^2 d^2}{n_{\text{core}}^2 n_{\text{core}}} \text{sinc}^2\left(\frac{\Delta\beta l}{2}\right) \frac{P^f}{W_0 T} l^2. \quad (3-5)$$

We can also derive more general expressions for d_{eff} and η as:

$$d_{\text{eff}} = C \frac{D}{4} d \quad (3-6)$$

$$\eta = \frac{C^2}{8} \omega^2 \left(\frac{\mu_0}{\epsilon_0}\right)^{\frac{3}{2}} \frac{D^2 d^2}{n_{\text{core}}^2 n_{\text{core}}} \text{sinc}^2\left(\frac{\Delta\beta l}{2}\right) \frac{P^f}{W_0 T} l^2, \quad (3-7)$$

where C is a field profile factor defined as:

$$C = \left(\frac{8\sqrt{2}}{3\pi}\right)^n \quad (3-8)$$

for a structure in which the field is transversely confined in n dimension(s) with a sinusoidal profile and in $(2-n)$ dimension(s) with a uniform profile, e.g., $n=1$ for a planar waveguide.

¹ It should be noted that the corrugation amplitude a in ref.31 equals not D but $W_0 D$.

3.2.2 A Numerical Example

As an example, we have made a numerical analysis on a channel waveguide SHG device using an organic nonlinear optical material 2-methyl-4-nitroaniline (MNA). The device model and material parameters used in this analysis are shown in Fig.3-1 and Table 3-I. In this analysis, the following assumptions are made: optical axes of MNA coincide with the coordinate axes and both the fundamental and second harmonic are TE_{x00} single modes. The fundamental and second harmonic wavelength are $1.06[\mu\text{m}]$ and $0.53[\mu\text{m}]$, respectively. The SHG efficiency was calculated for first order grating under no pump depletion

approximation in the exact quasi phase matching condition. The modal field distribution and the phase coefficient have been calculated by the Marcatili's method [42] for an isotropic media [43].

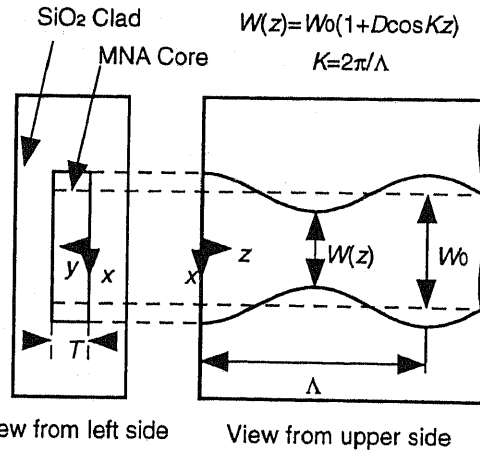


Fig.3-1 Model used for analysis of corrugated waveguide quasi phase matching

Table 3-I Material parameters used for the analysis of MNA channel width-corrugated waveguide QPM device.

Core : MNA [26][29][30]			Clad : SiO ₂		
		Fundamental	SH	Fundamental	SH
refractive index	n_x	1.764	2.301	1.449	1.461
	n_y	1.514	1.849		
	n_z	1.359	1.575		
SHG coefficient	d_{11}	$2.21 \times 10^{-21} \text{ C/V}^2$ [= $\epsilon_0 \times (250 \text{ pm/V})$]		0	

Fundamental wavelength : $1.06 \mu\text{m}$, Second Harmonic (SH) wavelength : $0.53 \mu\text{m}$

Figure 3-2 shows the calculated dependence of the corrugation pitch Λ on the fundamental wavelength λ . This calculated value is smaller than the value for a bulk, e.g. $\Lambda \sim 1 \mu\text{m}$ for $\lambda = 1.06 \mu\text{m}$. This is because the difference of the refractive index of the core and clad is larger for the second harmonic than the fundamental, and the effective refractive index mismatch is increased through the waveguide dispersion.

Figures 3-3, 3-4, and 3-5 show the calculated dependence of the normalized SHG efficiency on the waveguide thickness T , the averaged waveguide width W_0 , and the degree of width modulation D , through the LNME. The approximated analytic result for strong confinement

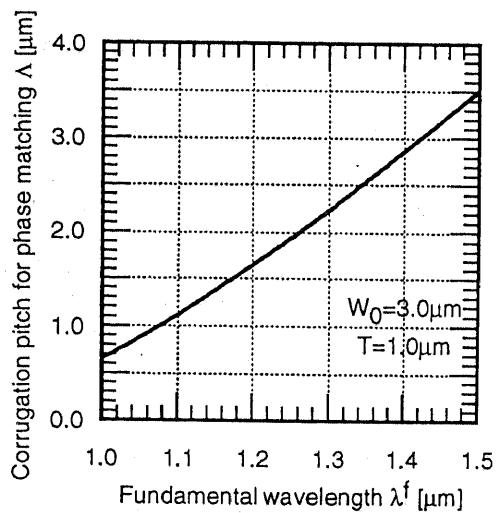


Fig.3-2 Dependence of the corrugation pitch Λ on the fundamental wavelength λ for the first order QPM in an MNA channel corrugated waveguide QPM device.

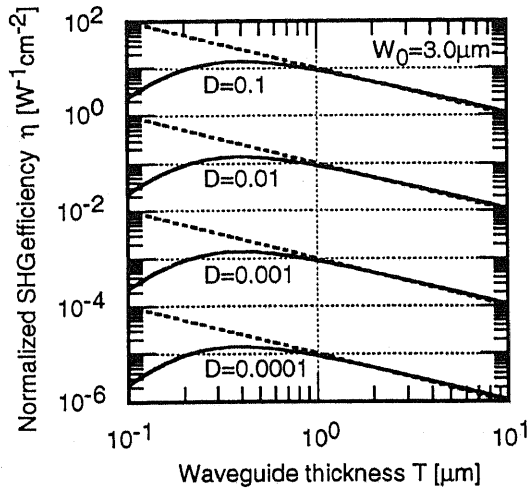


Fig.3-3 Dependence of SHG efficiency on the waveguide thickness for an MNA channel corrugated waveguide QPM device calculated with the LNME. The approximated analytic result for strong confinement limit given by Eq.(3-5) is shown with the dotted line.

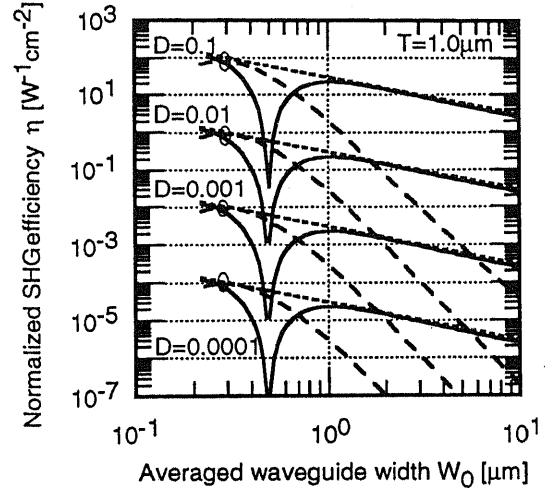


Fig.3-4 Dependence of SHG efficiency on the averaged waveguide width for an MNA channel corrugated waveguide QPM device calculated with the LNME (full line) and the INME (broken line). The approximated analytic result for strong confinement limit given by Eq.(3-5) is shown with the dotted line.

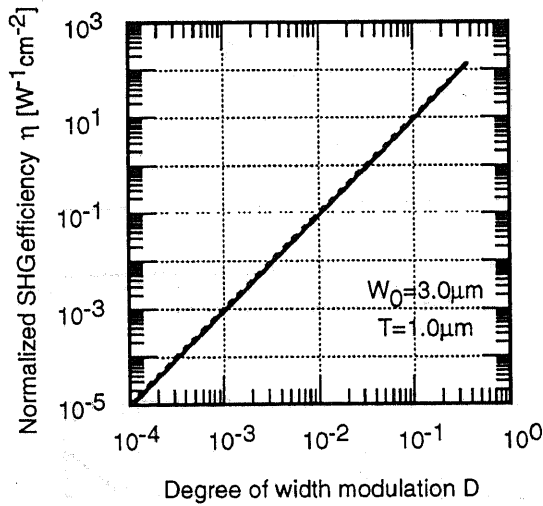


Fig.3-5 Dependence of SHG efficiency on the degree of width modulation for an MNA channel corrugated waveguide QPM device calculated with the LNME. The approximated analytic result for strong confinement limit given by Eq.(3-5) is shown with the dotted line.

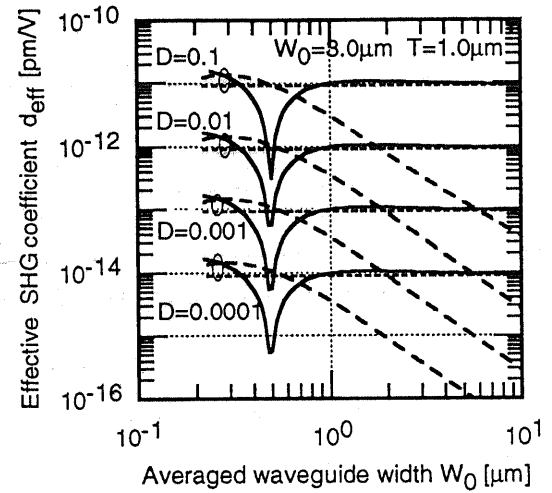


Fig.3-6 Dependence of effective SHG coefficient on the averaged waveguide width for an MNA channel corrugated waveguide QPM device calculated with the LNME (full line) and the INME (broken line). The approximated analytic result for strong confinement limit given by Eq.(3-4) is shown with the dotted line.

limit given by Eq. (3-5) is also shown with the dotted line. Figure 3-6 shows the effective SHG coefficient calculated with the LNME and its approximation for strong confinement limit given by Eq. (3-4). Figures 3-4 and 3-6 also show the result obtained by the INME (broken line).

We can see from Fig.3-4 that there are qualitative and quantitative differences between the results by the

LNME and INME. This is because the optical confinement of this device is strong, which can be seen from the fact that the strong confinement approximation gives quite good results coincident with the numerically calculated LNME results for smaller D and for larger W_0 and T . Hence, we can say that the modulation of field profile is predominant in QPM mechanisms in this device.

We should note that there is a zero efficiency point at about $W_0=0.5[\mu\text{m}]$ in the curve calculated with the LNME in Fig.3-4, in spite of the fact that the efficiency has a maximum at about $T=0.5[\mu\text{m}]$ in Fig.3-3. An explanation of this is given by Fig.3-7, which shows the dependence of the absolute value of $f(z)$ defined in Eq. (2-

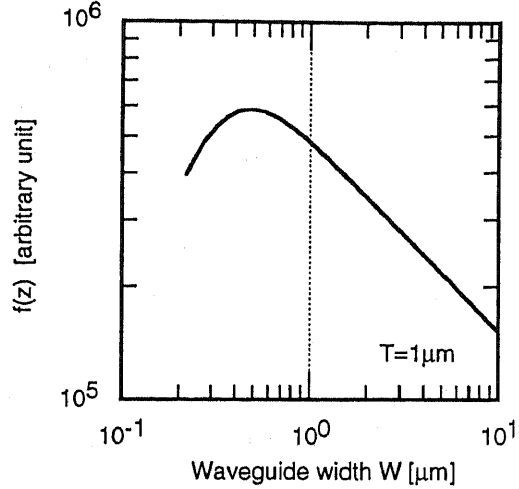


Fig.3-7 Dependence of absolute value of function $f(z)$ defined in Eq.(2-26) on the waveguide local width for an MNA channel corrugated waveguide QPM device.

26) on the *local* waveguide width W . A smaller waveguide width W gives a smaller confinement factor and a larger field intensity, and this trade-off relation gives $f(z)$ a maximum at about $W=0.5[\mu\text{m}]$. The dependence of the absolute value of $f(z)$ on the thickness T is the same as Fig.3-7 and is not shown. As derived in Eq. (2-36), the efficiency is proportional to the square of the Fourier coefficient F_q of the phase matching order $q=q_0$, which originates from the variation of $f(z)$ with the periodic width variation along the longitudinal direction. $f(z)$ is almost constant around the maximum at about the *local* width $W=0.5[\mu\text{m}]$, and thus F_q , except for $q=0$, are nearly equal to zero at about the *averaged* width $W_0=0.5[\mu\text{m}]$, and this results in the zero efficiency point in Fig.3-4. On the other hand, F_{q_0} is proportional to $f(z)$ for constant *averaged* width W_0 and degree of width modulation D . Therefore, the efficiency dependence on T is the same as the $f(z)^2$ dependence on T , resulting in the fact that the efficiency has a maximum at about $T=0.5[\mu\text{m}]$.

From Fig.3-6, it can be seen that the effective nonlinear coefficient d_{eff} calculated with the LNME approaches asymptotically to the value given with Eq. (3-4) with the increase of W_0 . On the other hand, d_{eff} calculated with the INME can be seen to decrease with the increase of W_0 . This is because the SHG efficiency in the INME depends on the variation of the overlap integral through the variation of the size of nonlinear core region, while the field profile does not vary. This means that the efficiency depends on the magnitude of the field at the boundary of corrugated core and it decreases with the increase of width and confinement. This behavior of SHG efficiency in the INME is quite different from that in the LNME, in which the SHG efficiency depends on the variation of the modal field profile.

The above mentioned behavior of the SHG efficiency and effective SHG coefficient cannot be explained with the single mode INME, because the variation of the modal field profile along the longitudinal direction is not considered in the INME. As described in Appendix 2.C, the single mode approximation in the LNME can be safely employed under the condition of Eq.(2-C1), e.g. $D \leq 0.01$, and may be valid under the condition of Eq.(2-

C4), e.g. $D \leq 0.1$. Thus, at least under these conditions, the LNME results are correct. As for a larger D , further investigation is necessary. On the other hand, an arbitrary field profile can be expanded with a complete set of modes. Therefore, the facts that a zero point appears in the SHG efficiency curve, as shown in Fig.3-4, and that the effective SHG coefficient is almost constant as shown in Fig.3-6, may be obtained if the multimode INME is employed. However, in the multimode INME, one must solve multimode coupled mode equations which have both linear and nonlinear perturbation polarization terms. This means that the amount of calculation in the multimode INME is much larger than in the single mode LNME. In addition, with the multimode INME, it may be difficult to clarify the physical mechanism of phenomena such as the appearance of the zero point in the variation of SHG efficiency with the averaged width and the effective SHG coefficient being almost constant. Thus, the LNME is much more advantageous for the analysis of SHG in a corrugated waveguide than the INME.

3.3 Quasi Phase Matching SHG Device by Periodic Domain Inversion

In this section, we analyze SHG devices with a periodic domain inversion structure for QPM. In this structure using ferroelectrics such as LiNbO₃, and LiTaO₃, the modal field profile varies not a lot, because the refractive index change by domain inversion is not large and waveguide size is almost uniform. Thus, the difference between the results with the LNME and with the INME is expected to be small.

3.3.1 Analytical Expression in the Limit of Strong Confinement

Analytical expression in the limit of strong confinement can be derived through almost the same procedure as described in sec.3.2.1. Thus, for an SHG device of W in width and T in thickness with a perfect domain inversion of 1:1 duty ratio and no refractive index change in domain inversion, d_{eff} and η can be expressed as follows:

$$d_{\text{eff}} = C \frac{2}{\pi q_0} d \quad (3-9)$$

$$\eta = \frac{8C^2}{\pi^2 q_0^2} \omega^2 \left(\frac{\mu_0}{\epsilon_0} \right)^{\frac{3}{2}} \frac{d^2}{n_{\text{core}}^2 n_{\text{core}}^2} \text{sinc}^2 \left(\frac{\Delta \beta l}{2} \right) \frac{P^f}{WT} l^2, \quad (3-10)$$

where q_0 is the quasi phase matching diffraction order of odd integer. The effective SHG coefficient is same as the well-known value $2d/\pi q_0$ [32] except for the field profile factor C defined in Eq. (3-8).

3.3.2 Numerical Examples

We have made a numerical analysis on channel waveguide SHG devices using LiNbO₃ and LiTaO₃. The device model and the material parameters used in this analysis are shown in Fig.3-8 and Table 3-II. The assumed structures are a proton exchanged channel waveguide on a z-cut substrate with periodic domain inversion by Ti

indiffusion for LiNbO₃, and a proton exchanged channel waveguide on a z-cut substrate with periodic domain inversion by proton exchange and high temperature annealing for LiTaO₃. The cores are approximated to have rectangular shape of W in width and T in thickness, and rectangular refractive index profile. Therefore, both fundamental and second harmonic are TM₀₀ single mode. The fundamental and second harmonic wavelength are 1.06[μm] and 0.53[μm], respectively. The SHG efficiency was calculated for first order grating under no pump depletion approximation in the exact quasi phase matching condition. The modal field distribution and the phase coefficient have been calculated by the Marcatili's method [42] for an isotropic media [43].

Table 3-II Material parameters used for the analysis of z-cut LiNbO₃ and LiTaO₃ channel periodically domain inverted waveguide QPM device.

a. Assumed process method and effects to material parameters for LiNbO₃ [41]

Fabrication method		Domain inversion Ti indiffusion	Channel Fabrication Proton exchange
Refractive index change	$\Delta n_x = \Delta n_y$	0.01	-0.04
	Δn_z	0.02	0.13

These refractive index changes are assumed to operate additively.

b. Material parameters for LiNbO₃ [41][47]

		Fundamental	SH
Refractive index	$n_x = n_y$	2.2322	2.3241
	n_z	2.1560	2.2340
SHG coefficient	d_{33}	$3.60 \times 10^{-22} \text{ C/V}^2 [= \epsilon_0 \times (40.7 \text{ pm/V})]$	

Fundamental wavelength : 1.06 μm Second Harmonic (SH) wavelength : 0.53 μm

c. Assumed process method and effects to material parameters for LiTaO₃ ²

Fabrication method		Domain inversion Proton exchange and anneal	Channel Fabrication Proton exchange
Refractive index change	$\Delta n_x = \Delta n_y$	0	0.015
	Δn_z	0	0.015

d. Material parameters for LiTaO₃ [41]

		Fundamental	SH
Refractive index	$n_x = n_y$	2.1366	2.2043
	n_z	2.1406	2.2089
SHG coefficient	d_{33}	$1.71 \times 10^{-22} \text{ C/V}^2 [= \epsilon_0 \times (19.3 \text{ pm/V})]$	

Fundamental wavelength : 1.06 μm Second Harmonic (SH) wavelength : 0.53 μm

²T. Yuhara, private communication

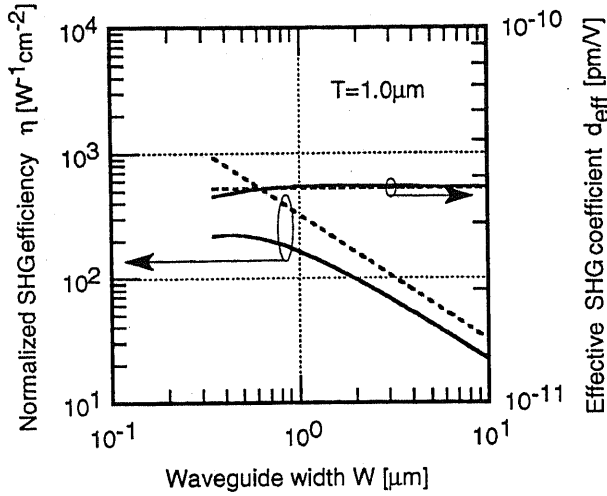


Fig.3-9 Dependence of SHG efficiency and effective SHG coefficient on the waveguide width for a LiNbO₃ channel periodically domain inverted QPM device calculated with the LNME. The approximated analytic results for strong confinement limit given by Eqs.(3-10) and (3-9) are shown with the dotted lines.

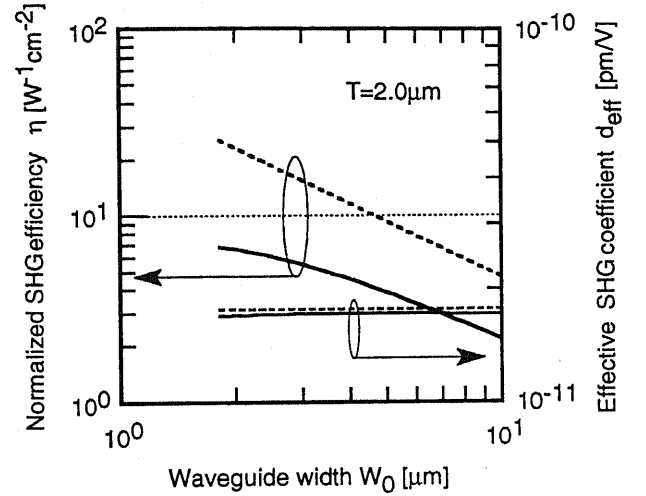


Fig.3-10 Dependence of SHG efficiency and effective SHG coefficient on the waveguide width for a LiTaO₃ channel periodically domain inverted QPM device calculated with the LNME. The approximated analytic results for strong confinement limit given by Eqs.(3-10) and (3-9) are shown with the dotted lines.

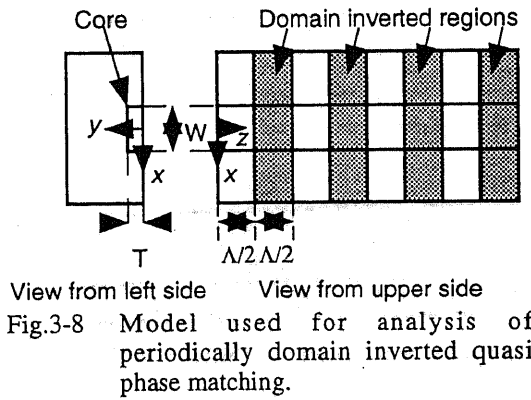


Fig.3-8 Model used for analysis of periodically domain inverted quasi phase matching.

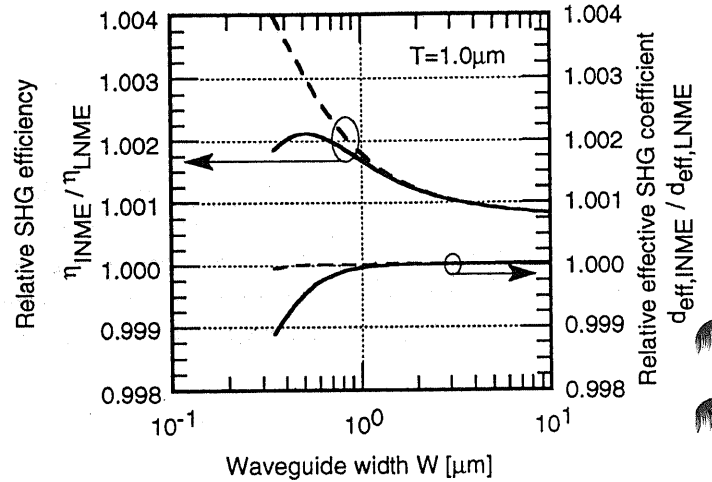


Fig.3-11 Dependence of SHG efficiency and effective SHG coefficient on the waveguide width for a LiNbO₃ channel periodically domain inverted QPM device calculated by the INME with (full lines) and without (broken lines) propagation coefficient variation along the longitudinal direction of the waveguide, plotted relatively to the LNME result.

Figures 3-9 and 3-10 show the SHG efficiency and the effective SHG coefficient dependence of the LiNbO₃ and LiTaO₃ device, respectively, on the waveguide width W calculated with the LNME numerically (full lines). The approximated analytic LNME results for strong confinement limit given by Eqs. (3-10) and (3-9) are also shown with the dotted lines. Though the separation between the numerical and analytic results of the SHG efficiency is larger for the LiTaO₃ device of which the optical confinement is weaker, the numerical and analytic effective SHG coefficients coincide well for both devices. Comparison of the INME results with the LNME results is made in Fig.3-11, in which the SHG efficiency and the SHG coefficient calculated with the INME are shown relatively to the results with the LNME. Calculation by the INME was done with (full lines) and without

(broken lines) propagation coefficient variation along the longitudinal direction of the waveguide [35][36], which is due to the refractive index variation caused by the domain inversion process. In the latter ("without propagation coefficient variation") case, ϕ_L in Eq. (75) of [36] is taken to be zero. It can be seen from Fig.3-11 that the INME results coincides with the LNME results almost perfectly, which is expected from the fact that modal field profile scarcely varies because of the small refractive index change by domain inversion and uniform waveguide size and that the predominant phase matching mechanism is the periodic inversion of the sign of the SHG coefficient. Thus, we may use these conventional INME method in place of the local normal mode expansion.

3.4 Concluding Remarks

In this chapter, analyses on devices quasi phase matched with corrugations and periodic domain inversions have been made. Analytical expressions under strong light confinement and numerical results of SHG efficiency and effective SHG coefficient are shown for each type of devices and compared with results by the conventional ideal normal mode expansion.

For the corrugation type device, an MNA channel waveguide device has been analyzed. A very characteristic result that the SHG efficiency and the effective SHG coefficient has a zero point at some rather small value of averaged waveguide width, e.g. about $0.5\mu\text{m}$, has been shown for the first time. This result originates from a trade-off relation between field intensity and field confinement factor as a function of waveguide width, which makes the modulation of nonlinear polarization with the corrugation null. The results with the conventional ideal normal mode expansion fails to give this feature. In addition, the ideal normal mode expansion fails to give sufficient results for wider waveguides qualitatively and quantitatively. These differences between the local and the ideal normal mode expansion is caused by the fact that modulation of the field profile is dominant in the quasi phase matching mechanism in this type of device, and the ideal normal mode expansion fails to describe it.

For the periodic domain inversion device, LiNbO_3 and LiTaO_3 devices have been analyzed. It was shown that the results with the local normal mode expansion and ideal normal mode expansion coincide considerably, because in this device, modulation of field profile is small and the effect on the SHG efficiency is small. In other words, it has been shown that the conventional ideal normal mode expansion can be used for a QPM device with periodic domain inversion.

Chapter 4

Proposal of New Fabrication Methods of Channel Waveguides Based on Organic Materials

4.1 Introductory Remarks

Low-molecular-weight organic materials such as MNA are of great interest owing to their very large optical nonlinearity. However, they have disadvantages of low mechanical strength and low processability, that is, most of them have high solubility with many organic solvents and some can be sublimated. Therefore it is not easy to fabricate channel waveguides with these organic crystals.

In spite of these difficulties, some fabrication methods of organic channel waveguides have been reported. These are shown in Fig.4-1, and reviewed briefly in the following:

1. Hollow core fiber (micro capillary) method shown in Fig.4-1(a) [48][49][50].

In this method, low molecular weight organic materials are filled as a single crystal core into a hollow core. This is the currently most frequently used method. This method has an advantage that a long fiber made of various types of glass with precise core size can be obtained. On the other hand, there are some disadvantages with this method such that Cerenkov radiation method is the only applicable phase matching method and that it is impossible to fabricate some components such as gratings or branches.

2. Rib fabrication method shown in Fig.4-1(b) [51].

In this method, two substrates to one of which trenches are fabricated are faced each other to fabricate organic crystal film between them. The organic crystal film around a trench functions as a rib waveguide. This method has a serious disadvantage of difficulty in controlling the waveguide thickness.

3. Strip loading method shown in Fig.4-1(c) [52].

In this method, high refractive index strips are fabricated into one of the glass substrates, and organic crystal film is fabricated between them. The organic crystal film under the high refractive index strips functions as channel waveguides. This method has a serious disadvantage of difficulty in controlling the waveguide

thickness. Although there is a similar method in which light is guided in the high refractive index strip rather than in the organic film, this has another serious disadvantage of low electric field intensity in the nonlinear organic film region.

4. Organic thin film etching method shown in Fig.4-1(d) [53].

In this method, organic thin film is fabricated first, and then, using some photolithography technique, etched into channels. Two techniques have been reported: in one, inorganic photoresist is used for photolithography and organic solvent for etching. In the other, an organic nonlinear material, which is undissolvable to the solvent of an organic photoresist, is fabricated into channels through ordinary photolithography and reactive ion etching process. The organic crystal film is fabricated between two glass substrates as in the planar waveguide fabrication process, and thus this method also has a serious disadvantage of difficulty in controlling the waveguide thickness. However, this disadvantage may be solved with some kind of organic thin film fabrication method such as vapor phase deposition or organic molecular beam heteroepitaxy. Another disadvantage of this method is that the organic core has no upper clad to protect the core.

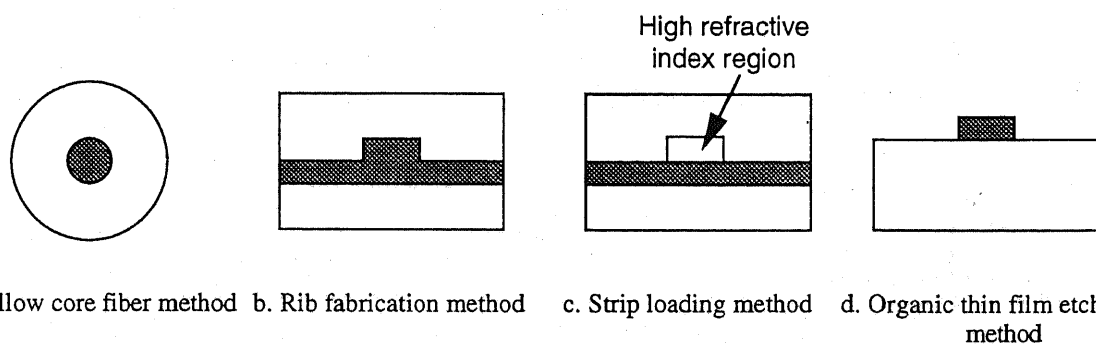


Fig.4-1 Some conventional fabrication methods of organic channel waveguides

In this chapter, we propose new fabrication methods for low molecular weight organic channel waveguides, including those with corrugations, without the disadvantages mentioned above.

In section 4.2, the outline of these method is described.

In sections 4.3-4, fabrication methods of a hollow core, which are the most important part of the proposed methods, are described.

In section 4.5, a fabrication method of a hollow core with corrugation, which is aimed to achieve quasi phase matching for SHG, is described.

In section 4.6, a summary is presented.

4.2 Proposal of New Fabrication Methods for Organic Channel Waveguides

The outline flow diagram of the proposed methods is shown in Fig.4-2. First, we fabricate a hollow core (micro-capillary), and then an organic nonlinear material is filled into and crystallized in the hollow core with the melting or solution method.

We propose two methods to fabricate a hollow core of an arbitrary form. One is called deposition method and the other sticking method. These methods are described in detail in the following sections. We also propose a fabrication method of a hollow core with corrugation, also described in detail in the following section.

Advantages of these new methods are as follows: Since the waveguide form is determined with a photolithography process, as described in the following subsections, waveguides with complicated forms such as a grating and a branch can be fabricated precisely. In addition, the core thickness can be determined accurately through controlling the thickness of the matrix core in the deposition method and the etched depth of the trench in the sticking method. Moreover, the organic core is protected with an upper clad layer. By choosing various materials for a clad and a substrate, the degree of freedom in designing a waveguide increases considerably.

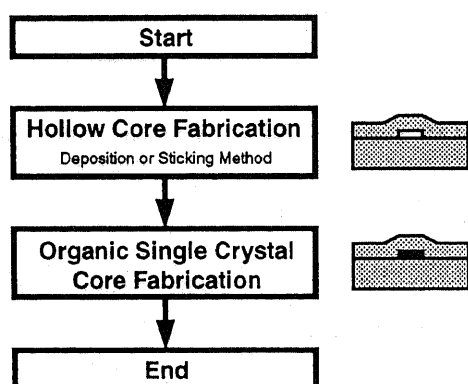


Fig.4-2 Outline flow diagram of new fabrication methods of organic channel waveguides

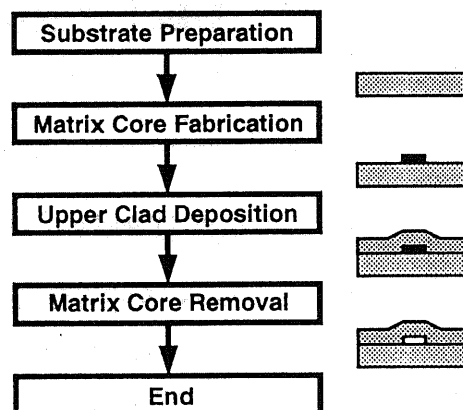


Fig.4-3 Flow diagram of the deposition method to fabricate hollow cores

4.3 Fabrication Method of a Hollow Core I - the Deposition Method

In the deposition method shown in Fig.4-3, a solid core is first delineated with photolithography. This core is a matrix of the finally fabricated organic crystal core. Then, an upper clad layer is deposited on the matrix core. At last, the matrix core is removed and a hollow core is fabricated. Therefore, a material for this dummy core must be easily removable. In this method, a branch and a grating with a long period can be easily fabricated with a photomask used in photolithography. A short period grating can be fabricated with two beam interference exposure as is proposed in section 4.5.

4.4 Fabrication Method of a Hollow Core II - the Sticking Method

In the sticking method shown in Fig.4-4, we use two substrates as an upper and a lower clad. A trench is fabricated on one of the substrates with photolithography and etching. This step is the same as that of the rib fabrication method described in section 4.1, but in this new method the two substrates are thermally stuck, i.e. directly bonded, to each other. Thus the trench becomes a hollow core and the thickness is well-controlled with the etching process. In this method, a branch and a grating with a long period can be easily fabricated with a photomask used in photolithography.

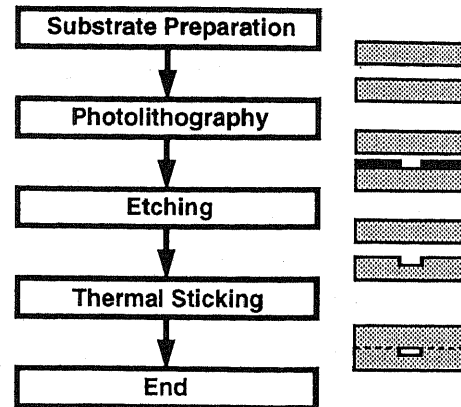


Fig.4-4 Flow diagram of the sticking method to fabricate hollow cores

4.5 Fabrication Method of a Hollow Core III - the Deposition Method with Interference Exposure to Fabricate Corrugated Waveguides

In the deposition method described above, a corrugation with a long period (longer than several μm) can be easily fabricated with a photomask in the photolithography process. However, a corrugation with a shorter period cannot be fabricated with this method. For example, the first order grating for quasi phase matching in an MNA channel waveguide SHG device has a period of $0.65\mu\text{m}$ for the fundamental wavelength of $1\mu\text{m}$, and such a short period corrugation is ordinarily fabricated with interference (holographic) exposure [54][55] or electron beam exposure. Therefore, another hollow core fabrication method based on the deposition method is proposed here.

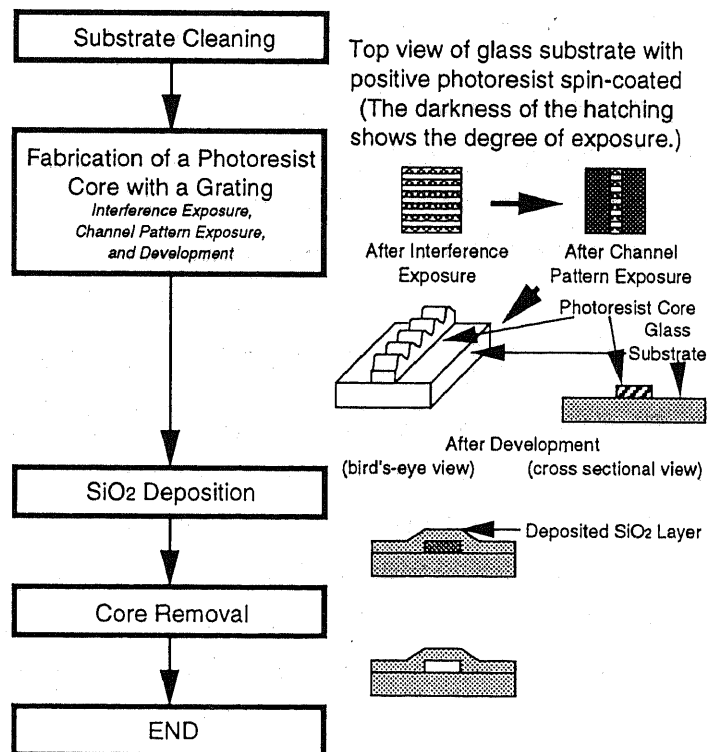


Fig.4-6 Flow diagram of corrugated hollow core fabrication method by the deposition method with two beam interference exposure

The process flow diagram is shown

in Fig.4-6. In this method, two beam interference exposure is employed and a positive photoresist is used as the matrix core. In an ordinary photographic process with the two beam interference exposure to fabricate a grating, which is a process used in the fabrication of distributed feedback lasers, a corrugation is fabricated on the surface of a substrate. Therefore, photoresist is coated thin enough and exposed sufficiently to be penetrated to the surface of the substrate with development. In this method, on the other hand, the corrugation is fabricated on the upper surface of a *matrix core*, and thus the photoresist is coated with the same thickness as the core and, as is shown in Fig.4-6, exposed with a properly controlled dose for a certain amplitude of corrugation, e.g., 20% of the core thickness. After the interference exposure, a channel pattern is exposed with enough dose to remove the photoresist at the unnecessary areas, and then the photoresist is developed into a channel with a corrugated upper surface. After depositing the upper clad layer, the corrugated hollow core is obtained by removing the matrix core.

4.6 Concluding Remarks

In this chapter, new channel waveguide fabrication methods suitable to low molecular weight organic materials have been proposed.

In these methods, a hollow core (micro-capillary) is fabricated at first, and then an organic nonlinear material is filled into and crystallized in the hollow core.

Two methods to fabricate a hollow core, i.e. the deposition method and the sticking method, have been proposed. In the deposition method, a matrix core is first delineated with photolithography, then an upper clad layer is deposited on the matrix core, and the matrix core is removed. In the sticking method, two substrates are used as an upper and a lower clad. A trench is fabricated on one of the substrates with photolithography and etching, and the two substrates are thermally stuck to each other. In addition, a fabrication method of a corrugated waveguide with two beam interference exposure has been proposed.

These methods have no disadvantages in the conventionally used methods, and have lots of advantages as follows: since the waveguide form is determined with a photolithography process, waveguides with complicated form such as a grating and a branch can be fabricated precisely. Also the core thickness can be determined accurately by controlling the thickness of the matrix core in the deposition method and the etched depth of the trench in the sticking method. Moreover, the organic core is protected by the upper clad layer. By choosing various materials for the clad, the degree of freedom in designing a waveguide increases considerably.

Chapter 5

Examinations on Process Conditions for Each Fabrication Step

5.1 Introductory Remarks

The fabrication methods described in the previous chapter can be achieved utilizing process technologies for semiconductors. Still, the materials and combinations of technology are different from semiconductor processes, and hence sufficient examination of each fabrication step is necessary. In this chapter, the experimental examinations and their results are described as follows:

In section 5.2, the substrate preparation step is examined.

In section 5.3, the deposition method for hollow core fabrication described in section 4.3 is examined. Each step of this method, i.e. matrix core fabrication step, upper clad deposition step, and matrix core removal step, is examined for various matrix core materials and clad deposition methods.

In section 5.4, the sticking method for hollow core fabrication described in section 4.4 is examined. Some etching methods for groove fabrication and thermal sticking condition are examined.

In section 5.5, the deposition method with interference exposure for corrugated hollow core fabrication described in section 4.5 is examined. Relations between magnitude of exposure and corrugation depth are obtained.

In section 5.6, the MNA crystal core fabrication step is examined. Some crystal growth methods are examined for quality and orientation of MNA crystal, and requisite conditions are clarified to grow a good crystal.

In section 5.7, the waveguide edge treatment step is examined.

In section 5.8, these results are summarized.

In Appendix 5.A, photolithography conditions are described.

In Appendix 5.B, upper clad deposition conditions for the deposition method are described.

In Appendix 5.C, evaluation methods for refractive index and crystal orientation of MNA with interference microscopes are described.

5.2 Substrate Preparation Step

Ordinary cover glasses has been employed as substrates, because they are about 0.2mm thin and easy to cut. Although slide glasses were examined at first, they were thick and it was difficult to obtain good normal end surface by cutting with a diamond pen or a wafer scribe.

As for substrate cleaning method, ordinary organic solvents and a commercially available semiconductor cleaning solvent are examined.

In the organic solvents cleaning method, the substrate is boiled and cleaned with ultrasonic for 10 minutes in trichloroethylene, then in acetone, and at last in ethanol. The substrate is dried with N₂ gas blow.

In the semiconductor cleaning solvent method, the substrate is cleaned with ultrasonic for 5 minutes in a commercially available semiconductor cleaning solvent (*Semico-Clean 23*, Furuuchi Chem. Co. Ltd.), linsed in pure water for 5 minutes with ultrasonic, and then dried with N₂ gas blow.

Comparison of these substrates after cleaning and after sputtering has shown that the latter method is better in its ability to remove dust and contamination and in the adhesion strength of sputtered thin film to the substrate.

5.3 Hollow Core Fabrication Step I - the Deposition Method

As described in section 4.3 and Fig.4-3, the deposition method is composed of the matrix core fabrication step, the upper clad deposition step, and the matrix core removal process. These steps are related each other and it is difficult to determine the process condition of each step independently. In the following subsections, hence, evaluation criteria and examined materials and methods are explained for each of the steps at first. Next, the examined combinations of the materials and methods are described, and then the examination and improvement are reported for each combination. The obtained results are summarized in the end.

The hollow core structures were evaluated mainly through observation of cross section with a SEM, i.e. scanning electron microscope (*DS-130*, Topcon Co., Ltd.), and an optical microscope.

In SEM observation of an insulator such as a glass, electron acceleration voltage should be set to a rather small value in order to avoid charge-up of the sample with incident electron beam which makes observation impossible. On the other hand, the resolution of SEM increases with the increase of electron acceleration voltage because energy dispersion of the electron beam decreases for higher electron acceleration. Conditions for cover glass samples were examined and the optimal acceleration voltage was 2kV with which sufficient resolution was able to be obtained for magnification of up to 10000 without charge-up. All of the following SEM photographs were taken with 2kV of acceleration voltage.

5.3.1 Evaluation Criteria and Examined Materials and Methods

5.3.1.1 The Matrix Core Fabrication Step

The following points are preferable for a matrix core material, and are the criteria for evaluation:

1. The thickness is easily and precisely controllable.
2. A channel can be easily fabricated.
3. Cross section is rectangular because waveguides with rectangular cross section can be designed easier than those with any other shape.
4. Surface is smooth in order to reduce propagation loss.
5. Deformation and deterioration does not occur during upper clad deposition.
6. Removal of the matrix core after upper core deposition is easy.

The following materials were examined as matrix core:

- a. Vacuum evaporated Al film. Lift off method was used to fabricate a channel (See Appendix 5.A1 for photolithography and lift-off condition).
- b. Negative type photoresist (*ONNR-22*, Tokyo Ohka Kogyo Co., Ltd., See Appendix 5.A2 for photolithography condition).
- c. Positive type photoresist (*OFPR-800*, Tokyo Ohka Kogyo Co., Ltd., See Appendix 5.A3 for photolithography condition).
- d. Positive type photoresist with high resolution (*TSMR*, Tokyo Ohka Kogyo Co., Ltd., See Appendix 5.A4 for photolithography condition).

The photomasks used in the photolithography process had straight channel patterns of 3 μ m or 5 μ m wide and 15mm long.

5.3.1.2 The Upper Clad Deposition Step

The following points are preferable to the upper clad deposition method, and are the criteria for evaluation:

1. The film quality is good. In this context, quality includes density, optical quality, and step coverage characteristics. In the deposition method, the upper clad is deposited on a matrix core with almost normal side surface and poor step coverage causes decrease of upper clad strength resulting into cracks in the upper clad.
2. The deposition temperature is low. High deposition temperature causes photoresist matrix core deformation and deterioration. Especially, deformation of the matrix core results into deformed organic core. In order to

avoid deformation and deterioration, a temperature of 120°C or below is preferable.

3. The deposition rate is high. In order to obtain sufficient upper core strength, a few μm or larger thickness is preferable.
4. The stress of deposited film is small. The film stress causes bend of a cover glass substrate, and in some cases, deformation of matrix cores.

The following SiO_2 deposition methods were examined:

- a. Sol-gel method (see Appendix 5.B1 for deposition condition).
- b. Plasma chemical vapor-phase deposition (P-CVD) method (see Appendix 5.B2 for deposition condition).
- c. Radio-frequency (RF) sputtering method (see Appendix 5.B3 for deposition condition).
- d. RF magnetron sputtering method (see Appendix 5.B4 for deposition condition).

In order to increase the degree of freedom of waveguide design, the refractive index of the upper clad should be varied. In the deposition methods described above, this can be achieved by, for example, depositing a SiON film and varying the ratio of O and N. However, more fundamental conditions must be determined first, and therefore only SiO_2 was employed as a deposition material in the examinations.

5.3.1.3 The Matrix Core Removal Step

The following features are preferable to the matrix core removal method, and are the criteria for evaluation:

1. The matrix core must be removed completely without any residue.
2. The removal rate should be reasonably high.
3. No deformation or cracks in the upper clad should be occur during the removal.

For the vacuum evaporated Al film matrix core, soak into HCl was examined.

For the matrix core with any type of photoresist, the following three methods were examined:

- a. Incineration. The photoresist matrix core was incinerated with a furnace (a hand-made one or RC-2400, Biorad Co. Ltd.) at about 500°C in ordinary atmosphere including O_2 .
- b. Soak into a photoresist remover. Three remover solvents were examined: *Remover 502* (Tokyo Ohka Kogyo Co., Ltd.) for negative type ONNR-22 photoresist; *Remover 10* (Tokyo Ohka Kogyo Co., Ltd.) and *Posistrip LE* (EKC Technology, Inc.) for positive type OFPR-800 and TSMR photoresists.
- c. Soak into reagent acetone (only for positive photoresists). The photoresist matrix core was removed with reagent acetone. This method was employed only in the case that the photoresist postbake and the upper clad deposition temperatures were less than about 120°C.

All of these removal processes were executed after exposing edges of the matrix core by cutting the substrate, so as to allow the matrix core to come into contact with a removal solvent or the atmosphere.

5.3.1.4 Combinations of Examined Materials, Deposition Methods, and Removal Methods

The combinations of processes and methods are listed in Table 5-I, in the order of examination and improvement.

Table 5-I Combinations of examined processes

	Material for matrix core	SiO ₂ deposition method	Matrix core removal method
1.	Evaporated Al	Sol-gel	Soak into HCl
2.	Evaporated Al	RF sputter	Soak into HCl
3.	ONNR-22 (negative)	Sol-gel	Incineration, soak into a remover
4.	ONNR-22 (negative)	RF sputter	Incineration, soak into a remover
5.	OFPR-800 (positive)	RF sputter	Incineration
6.	OFPR-800 (positive)	Plasma-CVD	Incineration
7.	OFPR-800 (positive)	RF magnetron sputter	Incineration, soak into a remover
8.	TSMR (positive)	RF magnetron sputter	Incineration, soak into acetone

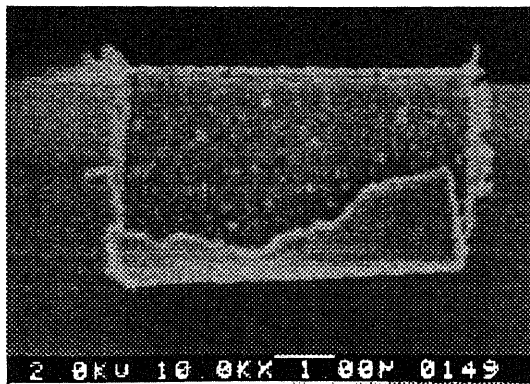
5.3.2 Examination and Improvement of Process Combinations

5.3.2.1 Examination of Combinations 1.- 4.

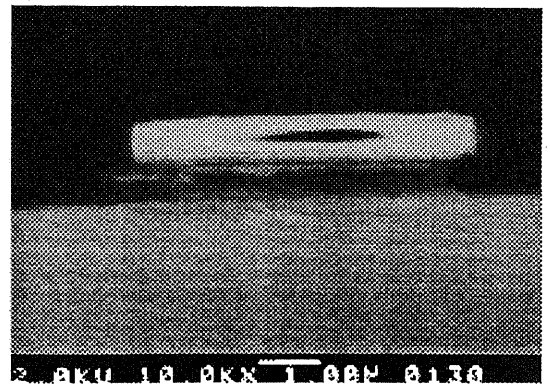
First of all, combinations 1. through 4. were examined. In these combinations, the evaporated Al film was compared with the negative photoresist ONNR-22 as a matrix core, and the sol-gel method with the RF sputter method as SiO₂ deposition method.

Figure 5-1 shows the cross sections of the matrix core with evaporated Al and ONNR-22 photoresist. The ONNR-22 photoresist core had rather fine rectangular cross section, in contrast with the evaporated Al film which has a rough surface. The turn over in the side edges of the evaporated Al core may be caused by incomplete lift-off process and thus improvable, while the surface roughness cannot be avoided for thick films with ordinary vacuum evaporation.

Figure 5-2 shows the cross sections of the matrix core with evaporated Al film on which the SiO₂ upper clad was deposited with the sol-gel method or with the RF sputter method. No deformation of the matrix core can be seen.

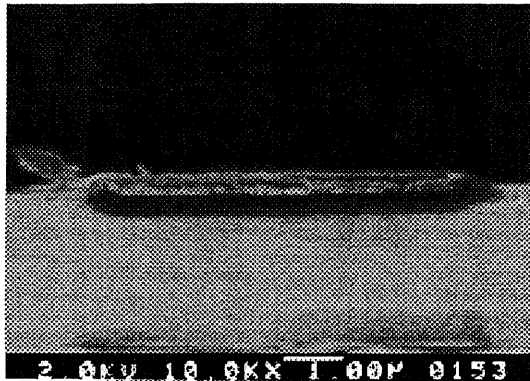


(a) Evaporated Al film. The matrix core can be seen hanging over the edge of the substrate.

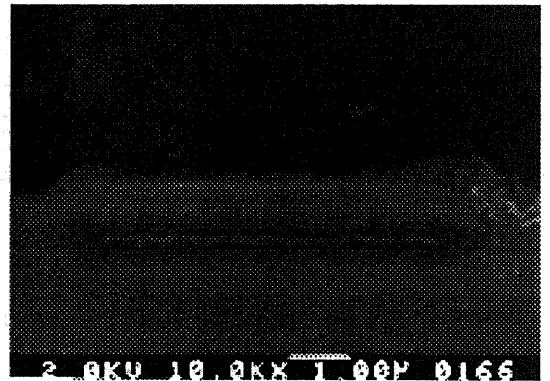


(b) *ONNR-22* negative type photoresist. The matrix core has peeled off the substrate during the cut of the substrate.

Fig. 5-1 Cross sectional SEM photographs of a matrix core



(a) Sol-gel method



(b) RF Sputter method

Fig. 5-2 Cross sectional SEM photographs of a matrix core with the evaporated Al film on which SiO_2 upper clad is deposited

Figure 5-3 shows the cross sections of the matrix core with *ONNR-22* negative type photoresist on which the SiO_2 upper clad was deposited with the sol-gel method or with the RF sputter method. It can be seen from Fig.5-3(a) that the *ONNR-22* core was deformed especially at both sides with the sol-gel clad. In the sol-gel method, silicon alchoxide is dehydrated, polymerized to gel, and turned into solid in the baking process when hard shrinkage occurs. This film shrinkage, especially at the sides of the matrix core where sol-gel film was as thick as the matrix core, caused the deformation of the "soft" photoresist matrix core. On the other hand, the upper corners of the matrix core were only a little rounded with the RF sputtered clad. The photoresist was discolored to dark brown during the sputtering. In general, photoresists are deformed at high temperature, e.g. 140°C or higher, through glass transition of the polymer. In addition, they deteriorate at high temperature. The surface of a cover glass sample can be easily heated to higher than 200°C during RF sputtering because of the low thermal conductivity of glass and the poor thermal contact between the sample and a water-cooled sample holder. This problem will be discussed again in subsection 5.3.2.4, and here it is pointed out that the deposition temperature can be sufficiently high to cause deformation and deterioration of the photoresist matrix core. Besides, sputter

etching of the matrix core through the reverse sputtering, and oxidization of the matrix core with sputtered oxide from SiO₂ target, can be considered as the cause of deformation and deterioration of the photoresist core.



(a) Sol-gel method



(b) RF Sputter method

Fig. 5-3 Cross sectional SEM photographs of a matrix core with the *ONNR-22* negative type photoresist on which SiO₂ upper clad is deposited

The removal process of the evaporated Al film with soak into HCl took several days or more. This quite low removal rate can be explained as follows: the Al solving reaction generates H₂ bubbles which separate HCl from the Al matrix core, and AlCl₃ generated in the reaction saturates in the neighbourhood of the Al-HCl contact surface resulting in deceleration of the reaction.

The removal process of *ONNR-22* photoresist with incineration took less than 1 day. No residue was observed in the hollow cores with an optical microscope. A cross section of a hollow core after the removal process is shown in Fig.5-4. The removal process with *Remover 502* failed because of the photoresist deterioration during the deposition process.

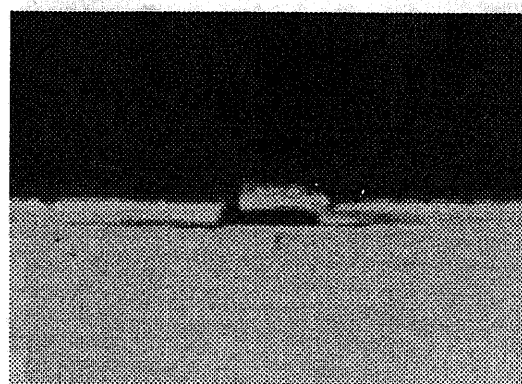
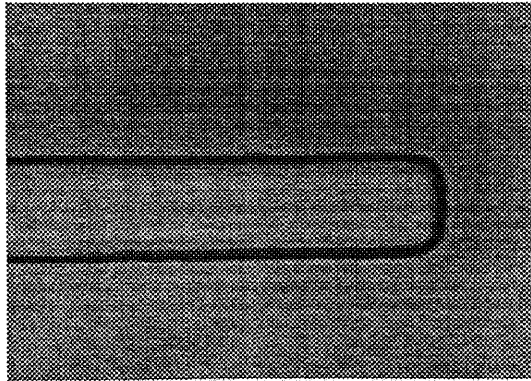
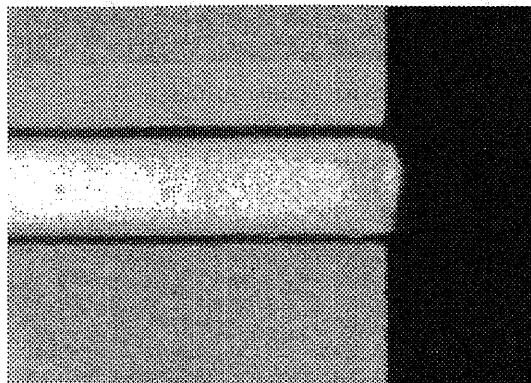


Fig. 5-4 A cross sectional SEM photograph of a hollow core with the *ONNR-22* / RF sputter method

All these results can be summarized as follows. As a material for the matrix core, the negative photoresist *ONNR-22* was superior to the evaporated Al film, because of the surface smoothness and of the ease in the matrix core removal. As the SiO₂ deposition method, the RF sputtering method was superior to the sol-gel method because of the smaller deformation in the matrix core and the higher deposition rate. Although evaporated Al film was superior to the photoresist in terms of matrix core deformation, the deformation of *ONNR-22* matrix core with the RF sputtering was not so hard and tolerable. The incineration method was superior as the removal process. Figure 5-5 shows the upper side optical microscopic view of each step of the combination of *ONNR-22*, RF sputtering, and incineration.



(a) After the matrix core fabrication



(b) After the upper clad deposition



(c) After the matrix core removal

Fig 5-5 Upper side optical microscopic photographs of each step of a hollow core fabrication process with the combination of *ONNR-22*, the RF sputtering, and the incineration.

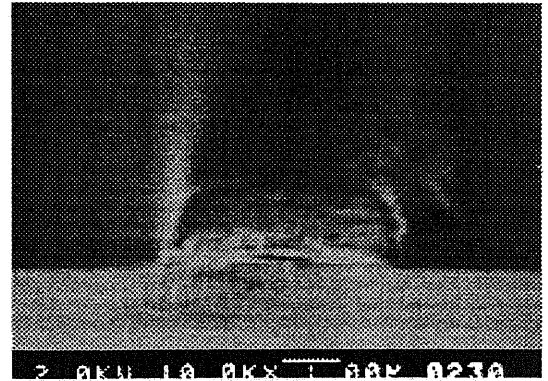


Fig.5-6 A cross sectional SEM photograph of an *OFPR-800* matrix core

5.3.2.2 Examination of Combinations 5. and 6.

Next, combinations 5. and 6. were examined. In these combinations, positive photoresist *OFPR-800* was employed as the matrix core material. *ONNR-22* negative photoresist was substituted with a positive photoresist *OFPR-800* because the former was discontinued and incompatible with the corrugated hollow core fabrication method described in section 4.6 and 5.5 which requires a positive photoresist. As the SiO_2 deposition method, Plasma-CVD method was compared with RF sputtering.

The photolithography condition is described in Appendix 5.A3, as already mentioned. The postbake temperature was set to 120°C to avoid deformation and to make the acetone soak removal method possible. Figure 5-6 shows a cross section of a matrix core with *OFPR-800*, which is less rectangular than *ONNR-22*.

The deposition condition of the Plasma-CVD method is described in Appendix 5.B3. This method had some

unpreferable features as follows: the deposited SiO_2 film, independent of the deposition temperature, was peeled from the substrate in many small areas adjacent to cores during the photoresist incineration process. In addition, the film deposited at higher than 200°C had compressive stress which bends the substrate. On the other hand, although the film deposited at lower than 200°C had no such stress, it is known that the film quality, characterized with low density and high refractive index [56], for such a low temperature deposition is not good.

The deposition condition of the RF sputter method is described in Appendix 5.B2. Sputter gas pressure was set to 2×10^{-2} Torr. Higher sputtering gas pressure of about 3×10^{-2} Torr caused degradation in adhesion between the film and the substrate. Although the deposition rate for 400W of RF power was about 15nm/min. for a short period of less than 20 minutes, the rate for a longer period decreased to about 9nm/min. This decrease may be attributed to the increase of deposition temperature resulting in the decrease of SiO₂ cluster adhesion probability on the substrate, and to the charge-up of the substrate resulting into reverse sputtering. Therefore, intermittent sputtering, in which the shutter was opened for 20 minutes to sputter and closed for 10 minutes to cool and discharge the substrate, was examined, and the deposition rate of sputtering period was sustained. The matrix core was deformed both in the continual, shown in Fig.5-7, and the intermittent sputtering. This suggests that the increase of surface temperature was quite large even in the intermittent sputtering. Thus, low power sputtering was examined with 30W of RF power, and this reduced the deformation as shown in Fig.5-8. In this low power deposition method, RF power was increased to 400W after 1 hour of low power sputtering in order to deposit the thick film. The matrix core was removed with the incineration method.

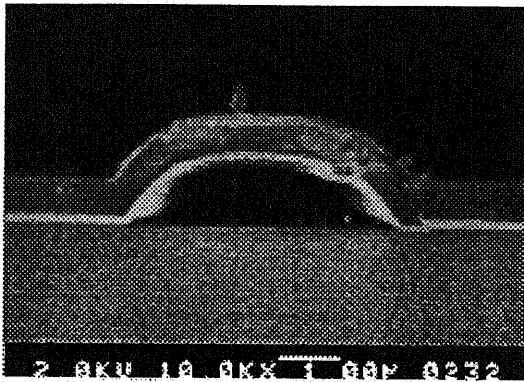


Fig.5-7 A cross sectional SEM photograph of a hollow core with the *OFPR-800* matrix core and the ordinary RF sputtering method



Fig.5-8 A cross sectional SEM photograph of a hollow core with an *OFPR-800* matrix core and the low-power RF sputtering method

These results are summarized as follows. The *OFPR-800* positive photoresist matrix core had less perfect rectangular cross section than the *ONNR-22* core, and was more easily deformed during the upper clad deposition. Therefore, sputtering condition was optimized to reduce deformation, where RF power was set sufficiently low to keep the substrate cool. The plasma-CVD deposition method was inferior to RF sputtering for the poor adhesion between the deposited film and the substrate, and for its stress in the deposited film.

5.3.2.3 Examination of Combinations 7. and 8.

At last, combinations 7. and 8. were examined. In these combinations, a high resolution positive photoresist *TSMR* was compared with *OFPR-800* as the matrix core material, and RF magnetron sputter method was examined as the SiO₂ deposition method. *TSMR* was introduced to improve the form of the cross section. The RF magnetron sputter has been introduced to replace the former RF sputter used in the above mentioned

combinations.

Photolithography condition for *TSMR* photoresist is described in Appendix 5.A4, as already mentioned. Figure 5-9 shows cross section of a hollow core with *TSMR* photoresist on which SiO_2 was deposited with the RF magnetron sputter. It can be seen that the cross section is almost rectangular. The difference in the cross sectional form between *OFPR-800* and *TSMR* can be attributed to the sensitivity characteristics of these photoresists. Figure 5-10 shows characteristics of exposure vs. residual photoresist thickness for *OFPR-800* and *TSMR*. It can be seen that *TSMR* has steeper curve than *OFPR-800* around the threshold exposure. At the pattern edges of a photomask, the magnitude of exposure varies rather slowly because of diffraction, and this caused slant side edges for *OFPR-800* which has a less steep sensitivity curve. *TSMR* has a steeper sensitivity curve and the pattern edges after development were almost normal resulting into rectangular cross section.

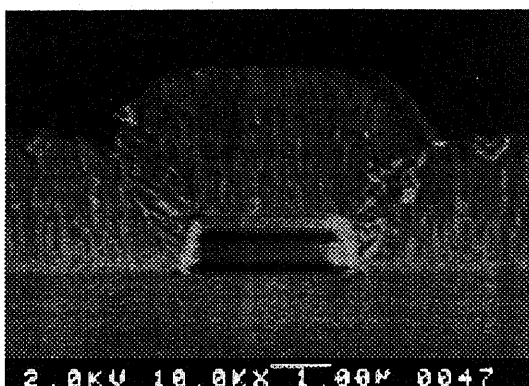


Fig.5-9 A cross sectional SEM photograph of a hollow core with the *TSMR* / RF magnetron sputter method

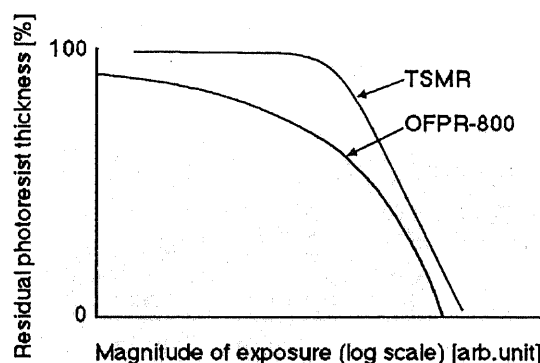


Fig.5-10 Sensitivity characteristics of *OFPR-800* and *TSMR* photoresists (modified from Ref.57). The residual thickness means the thickness after exposure and development.

The primary conditions for the RF magnetron sputtering method are described in Appendix 5.B4. In the following paragraphs, conditions which hardly affect the hollow core fabrication are described.

Although the deposition rate did not depend on the sputtering gas pressure as described in Appendix 5.A4, the film quality and the film stress was affected by the pressure. The quality was evaluated with some practical criteria for the organic channel waveguide fabrication as follows. If there are cracks in the upper clad, MNA crystal filled into the hollow core is dissolved during the final cleaning process with acetone. Therefore, the fact that whether MNA crystal core remains or not after cleaning with acetone can be used as a criterion of the quality evaluation. Another criterion of the quality evaluation is whether the sputtered film is doped with MNA or not during the crystal growth process. Porous film can be doped with MNA molecules, turning to yellow after the crystal growth and cleaning process. The film stress can be evaluated from the bend of the substrate after a certain thickness of film has been deposited. The results of examination are shown in Table 5-II. The compressive film stress decreased with the increase of sputtering gas pressure [57], and became almost zero at 2.0Pa. On the other hand, the film quality degraded with the increase of sputtering gas pressure. The composition of sputtering gas also affected to the film quality. Films deposited in O_2 rich gas had better quality. However, there was no

condition which satisfies both requirements of low film stress and high film quality. The film quality can be evaluated with SEM or optical microscope observation of the cross section, in which column structures can be seen for the porous film.

Table 5-II Dependence of RF magnetron sputtered film stress and quality on the sputtering gas pressure

Sputtering gas flow		Sputtering gas pressure [Pa]	Film stress ^a	Film quality	
Ar [sccm]	O ₂ [sccm]			MNA remaining ^b	MNA doping ^c
4	0	0.5	+++	O	O
4	0	1.0	++	O	O
4	0	1.5	+	X	O
4	0	2.0	0	X	X
1	3	2.0	0	X	O

- a. '+' means a compressive stress and the amount of '+' shows the magnitude of stress.
- b. 'O' and 'X' means high and low film quality, that is, MNA remained and did not remain after the final cleaning process with acetone, respectively.
- c. 'O' and 'X' means high and low film quality, that is, MNA was and was not doped to the film during the crystal growth, respectively

As mentioned in the previous subsection, photoresists, especially positive ones, are easily affected by temperature, resulting into deformation and deterioration. Positive photoresists were often rumbled with heat, in addition to the cross sectional deformation. In the sputter machine, a sample was ordinarily held on a water-cooled sample holder plate with metal cramps. Still, thermal contact between the sample and the holder was poor, and surface temperature of the sample during the sputtering raised to as high as 200°C, estimated from the discolor of the photoresist. Thus, in order to improve the thermal contact between the sample and the holder, a drop of diffusion pump (DP) oil was dropped on the holder and the sample was placed on it to spread the oil drop between the sample and the holder. With this method, thermal contact was extremely improved. Discolor, deterioration, and deformation of the photoresist matrix core were avoided, and the core was removable with acetone. The improvement of thermal contact was observed only in the area covered with the DP oil in the reverse side of the sample, and the photoresist core in the area not covered with the oil in the reverse side was still deteriorated and deformed. On the other hand, excess oil out of the sample edge sometimes splashed and contaminated the surface of the sample. Hence, the amount of the DP oil should be just enough to fill the gap between the sample and the holder.

A large film stress causes a bend of a cover glass sample and widens of the gap between the sample and the holder, resulting into degradation of the thermal contact improved with the DP oil. In order to avoid this film stress, an additional polyimide coating method was examined. In this method, the upper clad was deposited with the condition for low film stress, i.e. 2.0Pa of sputtering gas pressure, and the low film quality was compensated by coating polyimide on the upper clad in order to fill cracks and pinholes. The polyimide (*Photopies UR-3800*, Toray Co., Ltd.) was coated under the condition described in Appendix 5.B5 after the matrix core removal. In a

sample processed with this method, the matrix core was removable with acetone and MNA crystal cores remained without being dissolved with acetone during the final cleaning process.

Another method, the two step deposition method, to satisfy both requirements of low film stress and high film quality was examined. In this method, the upper clad was sputtered rather thin under the good film quality condition, e.g. 0.5Pa of sputtering gas pressure, and then sputtered rather thick under the low film stress condition, e.g. 2.0Pa. The deposition condition is described in Appendix 5.B6. This method enabled deposition with a rather high film quality with low film stress, and MNA crystal cores remained without being dissolved with acetone during the final cleaning process.

Three removal methods for positive photoresist cores, that is, incineration, soak into a remover, and soak into acetone, were examined. The incineration was same as described in the previous sections. Although even the deteriorated photoresist was removable with this method, the film stress sometimes increased and cracks occurred during the high temperature incineration. The remover soaking method was not practical because of its extremely low removal rate. This quite low removal rate can be explained as follows: as was the HCl soak method for the evaporated Al film, the viscosity of the remover was high, and the dissolved photoresist diffused slowly and saturated in the neighbourhood of core-remover contact surface, resulting in deceleration of the dissolving reaction. The acetone soaking method had reasonably high removal rate and it took about 2 days to remove 15mm length of photoresist matrix core. This high removal rate can be attributed to the fact that the dissolved photoresist diffused rather fast because of the low viscosity of acetone. Of course, this method was only applicable for a sample with low deposition temperature less than 120°C.

5.3.3 Summary of the Examinations for the Deposition Method

The results of the examinations are summarized as follows.

Table 5-III shows the results of the examination for the matrix core materials. Photoresists were superior to evaporated Al film, mainly because of the film surface smoothness and ease of removal. Positive photoresists were compatible to the interference exposure process for the corrugated waveguides, and, among those, a high resolution positive photoresist, *TSMR*, was preferable because of its rectangular cross section.

Table 5-III Features of materials for the matrix core

	Surface roughness	Cross sectional form	Deformation during the upper clad deposition	Removal easiness	Compatibility to the interference exposure
Evaporated Al film	X	X	O	X	X
ONNR-22 negative	O	O	Δ	O	X
OFPR-800 positive	O	X	X	O	O
TSMR positive	O	O	X	O	O

The results of the examination for the upper clad SiO₂ deposition method are shown in Table 5-IV. Sol-gel method was not preferable in spite of its excellent step coverage, mainly because of its shrinkage during the bake process which brought fatal deformation to the photoresist matrix core, and of its low deposition rate. Plasma-CVD method was not preferable for its rather high deposition temperature and for its rather large film stress. RF sputter method and RF magnetron sputter method was preferable for its low deposition temperature with a trick to improve thermal contact between the sample and holder. However, the conditions for high film quality and low film stress were incompatible with each other, and some special processes such as the two step sputtering method or the additional polyimide coating method had to be employed to obtain a sufficient result.

Table 5-IV Features of SiO₂ deposition methods for the upper clad

	Deposition rate	Deposition temperature	Step coverage	Film quality	Film shrinkage or stress
Sol-gel	X	X	O	-	X
Plasma-CVD	O	X	Δ	Δ	X
RF sputter	Δ	O	Δ	Δ	O
RF magnetron sputter	O	O	Δ	O ⁻ X	X ⁻ O

Table 5-V shows the results of the examinations for the core matrix removal methods. The HCl soaking method was not practical because of its very low removal rate, and this was one of the reasons for the inadequacy of the evaporated Al film for the matrix core. This was same for the remover soaking method. The incineration method and the acetone soaking method had reasonable removal rate, and the latter was more preferable for its low process temperature.

Table 5-V Features of removal methods of the matrix core

	Removal rate	Deterioration of the clad
HCl soak (Al film)	X	-
Incineration (photoresist)	O	Δ
Remover soak (photoresist)	X	-
Acetone soak (photoresist)	O	O

5.4 Hollow Core Fabrication Step II - the Sticking Method

As described in section 4.4 and fig.4-4, the sticking method is composed of the photolithography step, etching step, and the sticking (direct bonding) step, which are examined in the following subsections.

5.4.1 The Photolithography Step

This step was an ordinary photolithography process and a positive type photoresist *OFPR-800* was employed under a condition described in Appendix 5.A3.

5.4.2 The Etching Step

Wet etching and dry etching were examined.

Wet etching was examined with buffered HF of 16% concentration. The etching rate was about 86nm/min., and the etching time was limited to less than about 5 minutes by the peeling of the photoresist from the substrate. Therefore, the maximum depth of a groove was about 0.3 μ m. The photoresist was removed with a photoresist remover (*Remover 10*, Tokyo Ohka Kogyo Co., Ltd.) after etching.

Dry etching was examined with a reactive ion etcher (*30032*, Plasma Systems Corp.) using CF₄ etchant gas. The condition was as follows: the preparatory chamber pressure was 3 $\times 10^{-5}$ Torr. Etching was done under the condition of the etching gas CF₄ flow of 48sccm, the etching gas pressure of 0.3Torr, the RF power of 300W, the etching time of 350 seconds, followed by the photoresist ashing under the condition of the ashing gas O₂ flow of 30sccm, the ashing gas pressure of 0.2Torr, and the RF power of 100W. This condition resulted in over-etching and the etched surface was quite rough. Etching conditions must be further examined to obtain a good result.

5.4.3 The Sticking Step

A wet etched sample was used to examine this step. The grooved surface of an etched sample was faced with a plain sample, held between stainless steel plates, heated in an electric furnace with inactive N₂ gas flow for 1 hour, and slowly cooled down in the furnace. The heating process was examined for some temperatures between 600°C and 650°C. Two substrates stuck to each other for any temperature within the above range. Although the etched grooves remained for 600°C and 620°C, they vanished for temperatures higher than 640°C. In the former samples, the gap between the substrates remained unstuck in more than half of the area, as is shown in Fig.5-12, because of poor planar accuracy of the cover glasses.

Figure 5-13 shows a cross section of a hollow core with the sticking method. The substrates were completely stuck without any gap in the unetched regions. The side edges were slant because of undercut during wet etching. Figure 5-14 shows the upper side microscopic view of each step of the sticking method.

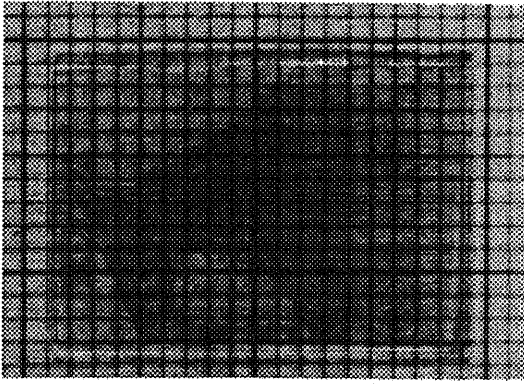


Fig.5-12 A photograph of stuck substrates. Remaining gap between the substrates can be distinguished with the interference fringes.

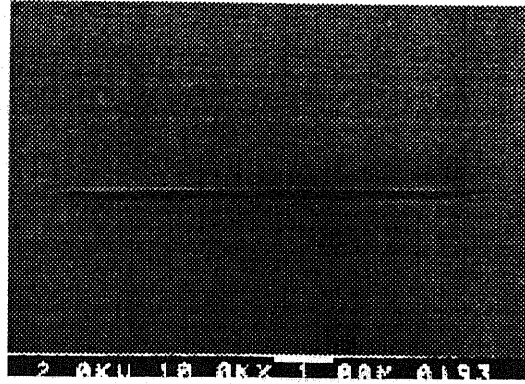
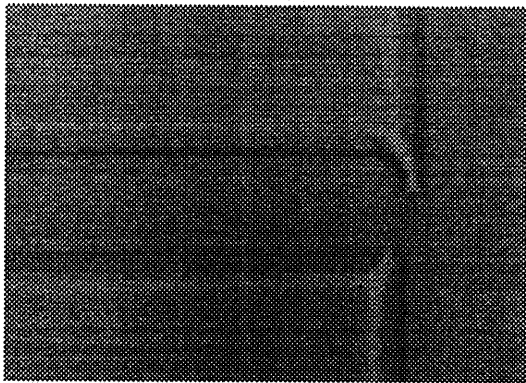
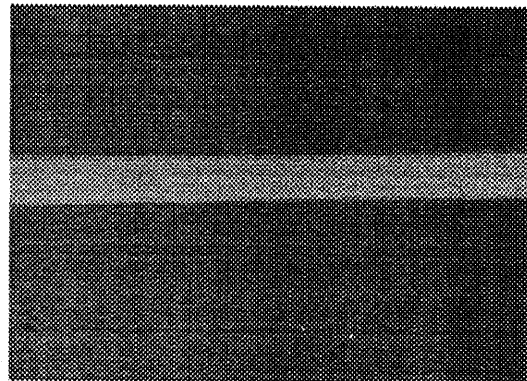


Fig.5-13 A cross sectional SEM photograph of a hollow core with the sticking method



(a) After wet etching



(b) After thermal sticking

Fig.5-14 Upper side optical microscopic photographs of each step of a hollow core fabrication process with the sticking method.

5.5 Hollow Core Fabrication Step III - the Deposition Method with Interference Exposure to Fabricate Corrugated Waveguides

As described in section 4.5 and Fig.4-5, the deposition method with interference exposure is composed of the corrugated matrix core fabrication step, the upper clad deposition step, and the matrix core removal process. The corrugated matrix core fabrication step is composed of the interference exposure step, the channel pattern exposure step, and the development step. Those steps other than the interference exposure step have been described in Section 5.3, and in this section only the interference exposure step is described.

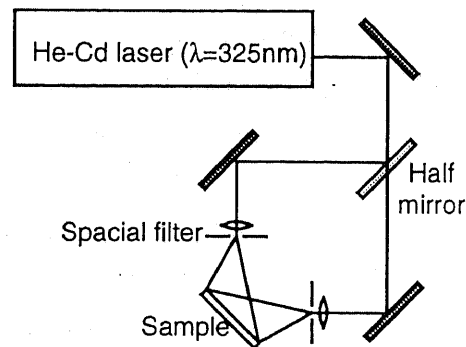
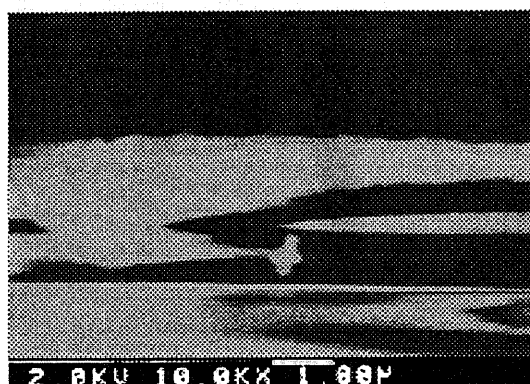


Fig.5-15 Experimental setup for interference exposure

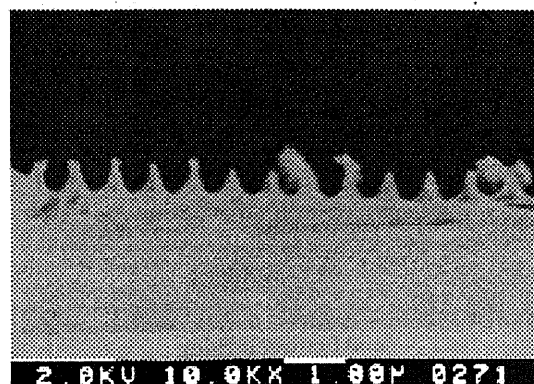
The coating condition of the positive type photoresists, *OFPR-800* and *TSMR*, were same as described in

Appendix 5.A3 and 5.A4, respectively. Figure 5-15 shows the experimental setup for interference exposure. The distances between the spacial filters and the sample was 300mm, and the normalized period variation, i.e. chirp, of the interference fringes for the sample of 15mm long was estimated as about 10^{-4} [58]. The polarization was s-polarization. The exposure condition was examined by observing the cross section after development with *NMD-3* (2.38% of concentration, Tokyo Ohka Kogyo Co., Ltd.) for 1 minute. In these examination, the channel pattern was not exposed.

OFPR-800 was examined for the exposure times of 10, 20, 40, 80, and 140 seconds with the UV light peak intensity of about $0.51\text{mW}/\text{cm}^2$. Figure 5-16 shows the cross sections for 80 and 140 seconds of exposure. Almost no corrugation was fabricated for 10 and 20 seconds of exposure, and the corrugation depth increased with the increase of the exposure time. The degree of thickness modulation for 80 seconds of exposure was about 0.2, which was a practical value for quasi phase matching SHG device described in section 3.1.



(a) Exposure time of 80 seconds



(b) Exposure time of 140 seconds

Fig 5-16 Cross sectional SEM photographs of *OFPR-800* photoresists developed after interference exposure

TSMR was examined for the exposure times of 20, 40, 60, 80, and 100 seconds with the same UV intensity as for *OFPR-800*. Figure 5-17 shows the cross sections for 40, 60, 80, and 100 seconds of exposure. Although the corrugation depth increased with the increase of the exposure time until 80 seconds, it decreased for 100 seconds of exposure, in which case the largest thickness of the photoresist, which corresponded to the minimum exposure, also decreased. The degree of thickness modulation for 40 seconds exposure was about 0.2, which was a practical value for quasi phase matching SHG device described in section 3.1. The upper side microscopic view of a corrugated hollow core is shown in Fig. 5-18, in which corrugation can be seen.

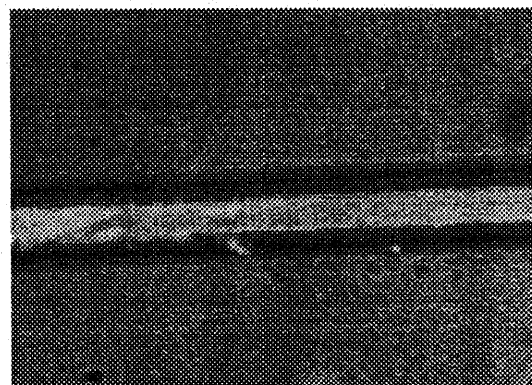


Fig.5-18 An optical microscopic photograph from upper side of a corrugated organic waveguide

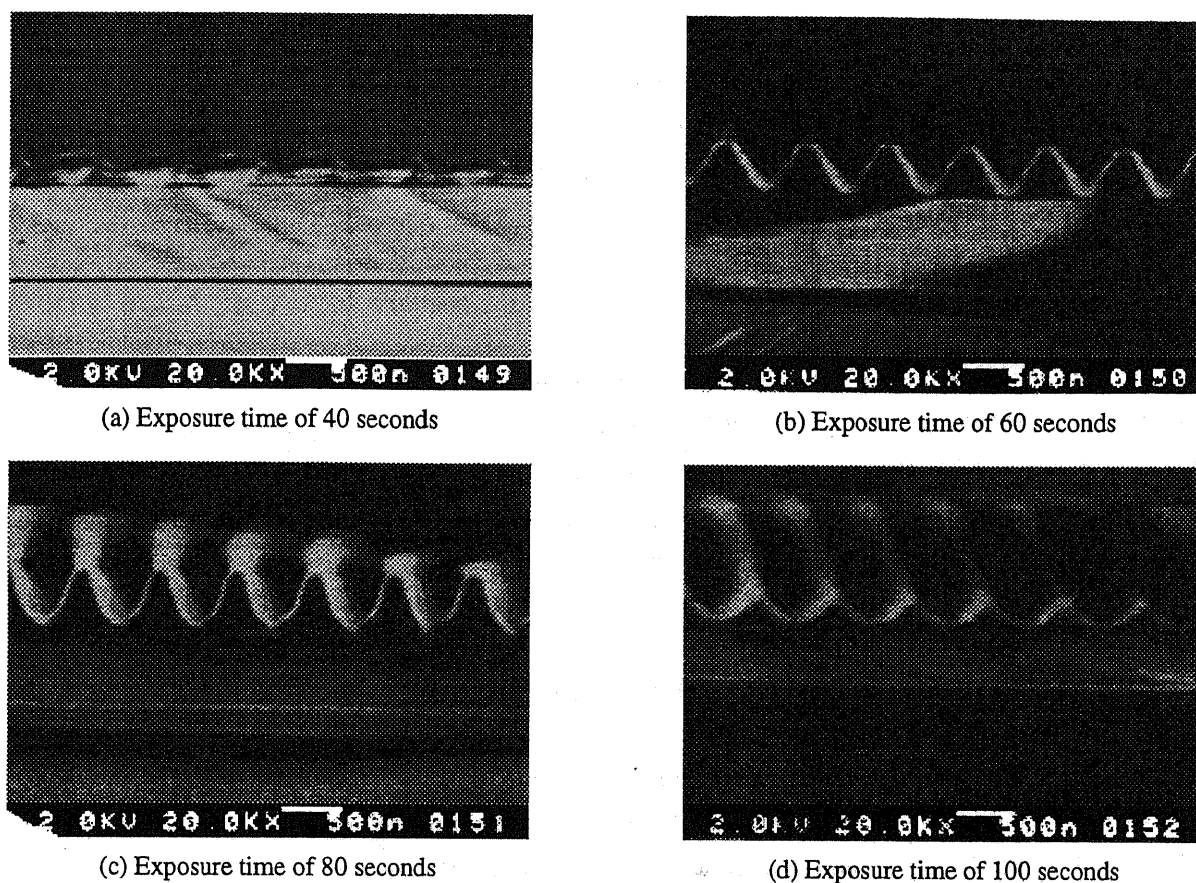


Fig.5-17 Cross sectional SEM photographs of TSMR photoresists developed after interference exposure

5.6 MNA Core Crystallization Step

The organic material MNA was filled into the hollow cores with capillarity by heating above the melting point, 131°C, and crystallized. In this section, evaluation methods of MNA crystal quality and orientation are described at first in subsection 5.6.1, and then some crystal growth methods are described.

5.6.1 Evaluation Methods of MNA Crystal Quality and Orientation

MNA crystal quality of the cores was evaluated with optical microscopic observation. Samples was observed with magnitude of 1000 and searched for cracks, bubbles, crystal boundaries, etc.

MNA crystal orientation was evaluated through the refractive index, which was measured with a transparent interference microscope (*Interfaco*, Karl-Zeiss Jena) in combination with a reflective interference microscope (*Optiphoto*, Nikon Co., Ltd.) or a talystep (*Dektak*, Sloan Co., Ltd.). MNA forms a biaxial birefringent crystal and, generally speaking, it is impossible to determine the crystal orientation uniquely with

refractive indices in a plane. However, the orientation can be determined if the optical axis with the largest or the smallest refractive index is included in the plane. As is mentioned in section 1.1.4, refractive indices of MNA are known [30], and it has been reported that the y axis with middle refractive index is orientated normal to the substrate plane and the x axis with the largest refractive index and the z axis with the smallest one are parallel to the surface of the substrates for a planar crystal growth between two substrates [30][29]. Hence, the crystal orientation can be determined through observing the anisotropic refractive indices parallel to the substrate surface with light normal incident upon the substrate.

In a transparent interference microscope, the light through a sample interferes with a reference light, which gives the optical path length. A reflective interference microscope or a talystep gives the surface step height, and the refractive index can be obtained from the optical path length and the surface step height. Birefringence can be measured with inserting a polarizer into the optical path of a transparent interference microscope. The measurement method is described in detail in Appendix 5.C.

5.6.2 Examination of MNA Crystal Growth Methods

Figure 5-19 shows the examined four crystal growth methods (furnaces), that is, the slow uniform cooling method, the Bridgeman method I with 10mm of furnace diameter, the zone melting method, and the Bridgeman method II with 0.5mmX30mm of furnace cross section. The employed MNA reagent was commercially available non-classified MNA powder (Tokyo Kasei Co., Ltd.) which has been reported as sufficiently pure and to be able to grow a fine bulk crystal without any additional purification [59].

5.6.2.1 The Slow Uniform Cooling Method

In this method, MNA powder is put with a sample holder into a small glass bottle, heated to melt in a thermoregulated furnace (*DN-43H*, Yamato Science Co., Ltd.), and cooled. Then a sample with hollow cores is set on the holder, heated again to 140°C for 30 minutes and cooled with the heater off. The sample is taken out and cleaned in reagent acetone to remove unnecessary MNA solid on the sample. The first MNA solidification process is employed to avoid intermittent filling of hollow core with MNA through intermittent melting of each MNA powder particle.

Figure 5-20 shows some crystal states of an MNA core. Obtained single crystal cores were up to 5~6mm long and many of them were 1~2mm long. This was quite long for uniform cooling, compared with the fact that the single crystal areas for planar crystal growth with temperature gradient had same length of sides. On the other hand, single crystal core length of up to 190mm has been reported for a hollow core fiber with temperature gradient. These results for channel waveguides can be attributed to the small solid-liquid surface resulting in crystal growth from a single nucleus.

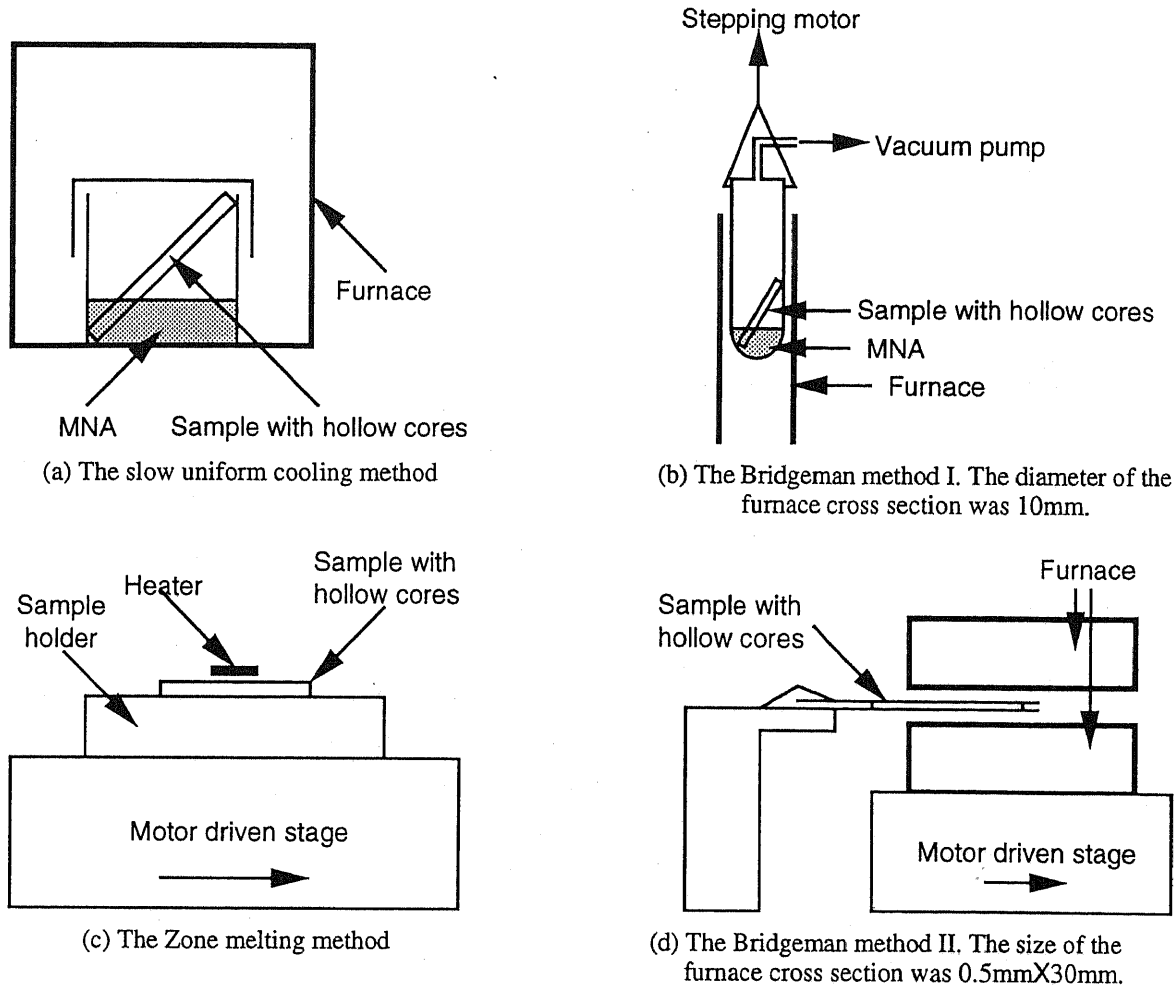


Fig.5-19 Examined crystal growth furnaces of MNA in hollow cores

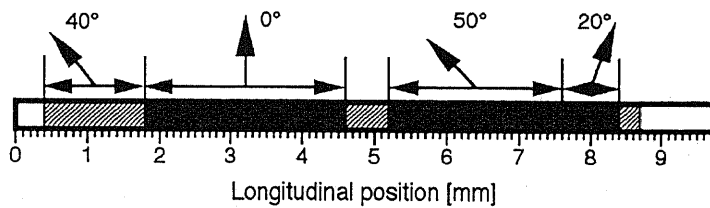


Fig.5-20 An example of MNA crystal quality and orientation grown with the slow uniform cooling method. The darkness of the hatching represents the quality, that is, the darker region has higher quality. The arrows pointing up show the orientation of x axis in the regions defined by the lateral arrows, and the angles were measured from normal to the longitudinal direction. z axis was included in the plane of the paper.

In most crystal domains, x axis were pointed in the longitudinal direction of a waveguide, y axis in the thickness direction, and z axis in the width direction, which coincided with those reported for planar waveguides. This was fatal to SHG application, and therefore this method was not preferable for SHG device fabrication.

5.6.2.2 The Bridgeman Method I

In order to control the gradient of temperature which was impossible in the above described method, crystal growth with a furnace shown in Fig.5-19(b) was examined. Figure 5-21 shows the temperature gradient in this furnace. In addition, the effect of atmosphere during the crystal growth was examined through comparison of crystal growth in vacuum of 10^{-4} Torr and in ordinary atmosphere.

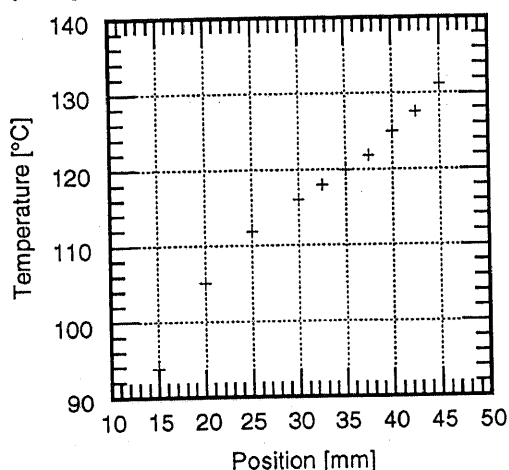


Fig.5-21 Temperature profile in the Bridgeman furnace I. The position was measured from the edge of the furnace, and the center of the furnace was further right.

In this method, MNA powder was put into a glass tube, evacuated to a vacuum of 10^{-4} Torr, heated to melt in the furnace, and cooled down. Then a sample with hollow cores was put into the tube, evacuated to vacuum, inserted to the furnace to be heated again to 140°C, and slowly pulled out from the furnace with a speed of about 5mm/hour. At last, the sample was taken out and cleaned with reagent acetone to remove unnecessary MNA solid on the sample. The first MNA solidification process was employed for the same reason as the slow uniform cooling method.

The quality and the orientation of MNA crystal core with this method did not improve from the previous method. This can be attributed to the insufficient temperature gradient on the sample caused with the large furnace compared with the sample. There was no difference between crystals grown in vacuum and in ordinary atmosphere.

5.6.2.3 The Zone Melting Method

In order to improve the temperature gradient on the sample, the zone melting method was examined. As shown in Fig.5-19(c), a heater was placed just above the sample, in order to make a steep temperature gradient on the sample.

In this method, MNA was filled into the hollow cores by the previous Bridgeman method I, with the only difference that the tube in which the sample was put in was pulled out of the Bridgeman furnace quickly. The MNA filled sample then was set on the sample holder of the zone melting furnace, and the heater was set above the sample. The sample was heated, and the stage was slowly moved.

Examined conditions were as follows: growth speeds of 9mm/hour and 18mm/hour, separations between the heater and the sample of 0.3mm and 0.5mm, and temperatures of heater surface of 300°C and 350°C. In addition, electric poling was examined with a DC electric field of 1kV/0.5mm. The results were not good, i.e. no

improvement was observed. This can be attributed to the fact that the heater is placed only above and not under the sample, and that under the sample there was a metal sample holder which acted as a thermal radiator. Therefore, the temperature of the sample surface was substantially different from the heater temperature, and was difficult to be set to a certain value. Moreover, the temperature gradient was gentle because of the metal holder.

5.6.2.4 The Bridgeman Method II

Based upon the results obtained in the above methods, a new Bridgeman furnace shown in Fig. 5-19(d) was designed. In this furnace, it was aimed to obtain controllability of the sample temperature and the temperature gradient, and the temperature uniformity in the middle of the furnace, through reducing the space around a sample within the furnace. Figure 5-22 shows the temperature gradient of this furnace, from which it can be seen that a steep temperature gradient is realized.

In this method, MNA powder was put between two cover glasses for sample holding, heated to melt in the furnace, and cooled. Then the sample holders were separated, and a sample with hollow cores was put on the solid MNA on the holder and sandwiched with another holder. They were inserted into the furnace, heated again to 140°C, and pulled out of the furnace slowly. After the growth, the sample was taken out of the holders and cleaned in reagent acetone to remove unnecessary MNA solid on the sample. The first MNA solidification process was employed to avoid intermittent filling of hollow core with MNA through intermittent melting of each MNA powder particle.

Crystal growth speeds of 1.8mm/hour through 20mm/hour were examined. The crystal quality was improved with the decrease in the growth speed. Especially, the decrease of MNA cracks and the voids at the convex regions of corrugation, which often occurred at higher growth speed or in the previous growth methods, was apparent. The crystal orientation showed a different tendency from the previous methods and some reported results, that was, x axis was oriented in the width direction for about half of the crystals. For the other half, x axis was oriented in the longitudinal direction, as was mentioned above. The y axis was oriented in the thickness direction, i.e. normal to the surface, for most of the crystals grown rather fast, while x axis was sometimes oriented normal to the surface for slowly grown crystals. In the latter case, y axis was oriented in the width direction and z axis in the longitudinal direction. However, the crystal orientation was not uniquely controllable with a certain growth condition. Fig. 5-23 shows some examples of quality and orientation of core crystal.

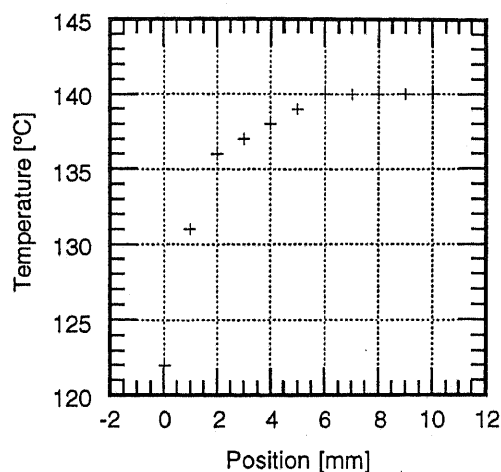


Fig. 5-22 Temperature profile in the Bridgeman furnace II. The position was measured from the edge of the furnace.

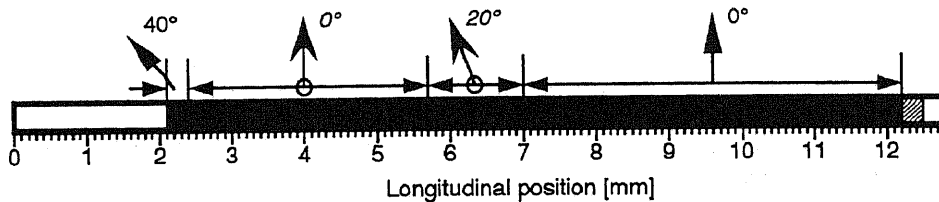


Fig.5-22 An example of MNA crystal quality and orientation grown with the Bridgeman method II. The darkness of the hatching represents the quality, that is, the darker region has higher quality. The arrows pointing up with an angle written in roman and in *italic* show the orientation of *x* axis and *y* axis, respectively, in the regions defined by the lateral arrows. The angles were measured from normal to the longitudinal direction. *z* axis was included in the plane of the paper.

5.6.3 Summary of MNA Crystal Growth

In order to grow a high quality MNA crystal core, it was necessary to establish a uniform and well controlled temperature distribution in the middle of the furnace and a steep temperature gradient in the edge of the furnace. This was realized by reducing the space around a sample within a furnace. In addition, sufficiently slow speed, as low as 2mm/hour, was preferable for high quality crystal growth. Under these conditions, the preferable crystal orientation, i.e. transversally oriented *x* axis, was obtained, even though perfect orientation was not achievable.

5.7 Waveguide End Surface Cutting Method

High quality end surfaces are indispensable to channel waveguides with end-fire optical coupling. It is impossible to use a cleaved surface for an amorphous such as glass, and therefore the end surface of glass is ordinarily polished after cut. Though, polishing an organic core waveguide often results in dent at the core because of the difference in hardness of an organic core and a glass clad. Thus, an 'as-cut' end surface was examined. A glass substrate is usually cut through putting force across a scratch on a reverse side with a diamond pen. This method often resulted into a slant end surface which was not preferable to an incident surface. Therefore, a multi-time scribing method was examined, in which a substrate was scribed on the reverse side with a wafer scribe (A-WS-100A, Tokyo Seimitsu Co., Ltd.) for a few times until cut up. A rather good, almost normal end surface was obtained with this method. The core surface and the clad surface was coincident in most of the cases.

It should be noted that MNA core sublimated at the end surface and the core surface retreated with a rate of about 2μm/day. Although this was not a serious problem for a short term experiment, some end surface coating should be applied to avoid sublimation for practical long term use.

5.8 Concluding Remarks

In this chapter, the results of experimental examination of each step of the fabrication methods of an organic channel waveguide have been described, which are summarized as follows:

In the deposition method, photoresists were superior to an evaporated Al film as the matrix core material, mainly because of the film surface smoothness and ease of removal process. Positive photoresists were compatible to the interference exposure process for corrugated waveguides, and a high resolution positive photoresist, *TSMR*, was especially preferable because of its rectangular cross section.

As an upper clad deposition method, the sol-gel method was not preferable in spite of its excellent step coverage, mainly because of its shrinkage during the bake process which brought fatal deformation to the photoresist matrix core, and of its low deposition rate. Plasma-CVD method was not preferable for its rather high deposition temperature and for its rather large film stress. RF sputter method and RF magnetron sputter method was preferable for its low deposition temperature with a trick to improve thermal contact between the sample and holder. However, the conditions for high film quality and low film stress were incompatible with each other, and some special processes such as the two step sputtering method or the additional polyimide coating method must be employed to obtain a sufficient result.

As the matrix core removal method, the HCl soaking method was not practical because of its very low removal rate, and this was one of the reasons for the inadequacy of the evaporated Al film for a matrix core. This was same for the remover soaking method. The incineration method and the acetone soaking method had reasonable removal rate, and the latter was more preferable for its low process temperature.

In short, the best was the combination of *TSMR* photoresist as the matrix core, the RF magnetron sputtering method combined with the two-step deposition or the additional polyimide coating method as the upper clad deposition method, and the acetone soaking method as the matrix core removal method.

In the sticking method, cover glass substrates was able to be stuck completely with 600–620°C for 1 hour, without vanishing of the etched grooves. Wet etching with buffered HF had a disadvantage of limited etching depth up to about 0.3μm, and dry etching with CF₄ RIE needed more examination on the etching conditions.

In the deposition method with interference exposure, relations between the magnitude of exposure and the corrugation depth was obtained, and 80 seconds of exposure for the *OFPR-800* photoresist and 40 seconds of exposure for the *TSMR* photoresist was suitable to obtain the degree of modulation in the photoresist thickness of 0.2.

In order to grow a high quality MNA crystal core, it was necessary to establish a uniform and well controlled temperature distribution in the middle of a furnace and a steep temperature gradient in the edge of the furnace, and this was realized by reducing the space around a sample within a furnace. In addition, sufficiently

slow speed, as low as 2mm/hour, was preferable to the high quality crystal growth. Under these conditions, the preferable crystal orientation, i.e. transversally oriented x axis, was obtained, even though perfect orientation was not achievable.

End surfaces with high quality and normal to waveguides was obtainable with the multi-time scribing method with a wafer scribe.

From these examinations, the fundamental fabrication conditions have been determined. Although these can be improved more, the new organic channel waveguide fabrication methods have been established.

Appendix 5.A Photolithography Conditions

Conditions of photolithography for the evaporated Al film, negative photoresist *ONNR-22*, positive photoresist *OFPR-800*, and another positive photoresist *TSMR* are summarized in the following Table 5-VI.

Table 5-VI Photolithography conditions

	5.A1	5.A2	5.A3	5.A4
	Evaporated Al film with lift-off method	Negative photoresist <i>ONNR-22</i>	Positive photoresist <i>OFPR-800</i>	Positive photoresist <i>TSMR</i>
Photoresist	<i>OFPR-800</i>	<i>ONNR-22</i>	<i>OFPR-800</i> 50cP	<i>TSMR</i> 25cP
Spin coating ^a	500rpmX5sec. + 6000rpmX30sec.	500rpmX5sec. + 6000rpmX30sec.	(a)500rpmX5sec. + 6000rpmX30sec. (b)500rpmX5sec. + 6000rpmX30sec.	500rpmX5sec. + 6000rpmX30sec.
Photoresist thickness	1.15 μ m	0.75 μ m	(a)1.15 μ m (b)1.69 μ m	1.0 μ m
Prebake	90°C 30min.	90°C 30min.	90°C 30min.	90°C 30min.
Exposure time ^b	28sec. ^c	28sec.	10sec.	10sec.
Development	<i>NMD-3</i> 1min.	<i>ONNR-22 Developer</i> 1min.	<i>NMD-3</i> 1min.	<i>NMD-3</i> 1min.
Rinse	Pure water 1min.X 2	<i>ONNR-22 Rinse 1</i> 1min., <i>Rinse 2</i> 1min.	Pure water 1min.X 2	Pure water 1min.X 2
Postbake	-	150°C 30min.	120°C 30min	120°C 30min
After treatment	Al evaporation, and lift off with boiled acetone	-	-	-

a. Spin coater: *IH-2D* (Mikasa Co., Ltd.)

b. Photomask aligner: *PLA-501F* (Canon Co., Ltd.), exposure ultraviolet intensity > 8mW/cm²

c. This conditions was not optimized and different from the condition of 5.A3

Appendix 5.B Conditions and Some Comments on SiO₂ Upper Clad Deposition

5.B1 Sol-Gel Method

In this method, a solution of metal-organic or -inorganic compounds is solidified into gel with hydration and polymerization, and further solidified into metal oxide with heat [60]. This method has been attracting attention because surfaces with any profile can be coated with spin or dip coating method at lower temperature than some other methods such as thermal CVD.

In this examination, a commercially available material solution (*OCD Si-11000*, Tokyo Ohka Kogyo Co., Ltd.) was employed. At first, the solution was diluted to half of the concentration with reagent ethanol. The diluted solution was spin-coated under the condition of 500rpm 1sec. + 6000rpm 30sec., and baked in a furnace at 250°C for 30min. Film thickness after baking was 0.15μm, and this process was repeated until sufficient thickness was obtained.

In the sol-gel method, cracks tend to be generated during the baking for a thick film. This was the reason for diluting the solution. For the diluted solution, cracks were sometimes generated around the center of spin-coating and at the edges of a substrate, where coated film was thicker than other areas.

5.B2 Plasma-CVD Method

In this method, SiO₂ was deposited with a plasma-CVD machine (*CPD-2114 Special*, ULVAC Corp.) under the following conditions: preparatory vacuum pumping to 2×10^{-5} Torr, the material gases were SiH₄ and N₂O, mass flow ratio 1:8, mass flow of N₂O 100sccm, the total gas pressure 0.3Torr, RF power 30W, and the deposition temperature 140°C–250°C.

5.B3 RF Sputtering Method

In this method, SiO₂ was sputtered with a parallel planar electrodes type RF sputter machine (*SBR-1104*, ULVAC Corp.) under the following conditions: the target was SiO₂, the preparatory vacuum pressure 2×10^{-6} Torr, the sputtering gas Ar with the pressure of 2×10^{-2} Torr, the RF power 400W (in the primary condition), and the presputtering time 15min. The deposited film was easily peeled off from the substrate under the condition of a higher sputtering gas pressure of 3×10^{-6} Torr.

5.B4 RF Magnetron Sputter Method

In this method, a parallel planar electrode type RF magnetron sputter machine (*SPF-210H*, Anelva Co., Ltd.) was employed. This sputter had been converted into a reactive type with Ar, O₂, and N₂ gas systems. The primary deposition conditions were as follows: the sputtering target was SiO₂, the preparatory vacuum pressure 5×10^{-5} Pa, the sputtering gas Ar and O₂ with some ratio in mass flow of 4sccm:0sccm, 3:1, 2:2, 1:3, and 0:4, the total sputtering gas pressure of 0.25 through 5.0 Pa, and the RF power of 100, 200, and 300W. The presputtering time was 10min.

The sputtering rate was 60nm/min. for Ar only with 300W of RF, and 17nm/min. for Ar:O₂=1:3 with 300W of RF. It hardly depended on the sputtering gas composition, and decreased with the increase of O₂ ratio. On the other hand, the rate was almost independent of the total gas pressure in the range of 0.25 through 2.5Pa, and decreased with higher total pressure. However, as was mentioned in subsection 5.3.2.4, the film quality and the film stress hardly depend on the total pressure and the ratio of Ar and O₂ gas flow.

5.B5 Additional Polyimide Coating Method

Commercially available polyimide (*Photonies UR-3800*, Toray Co., Ltd.) was spin-coated under the condition of 500rpm 10sec. + 6000rpm 30sec., followed with a baking process of 80°C 60min. + 180°C 30min. + 300°C 30min. + 400°C 30min. The film thickness after all these process was about 1 μ m.

Appendix 5.C Measurement of Core Refractive Indices and Crystal Orientation with an Interference Microscope

A transparent interference microscope measures optical path length of a sample, and refractive index can be obtained from this combined with the thickness. Hence, refractive indices and crystal orientation of an organic core can be measured with a transparent interference microscope combined with a step height measuring method such as a reflective interference microscope or a talystep. The *Interfaco* microscope (Karl-Zeiss Jena) which was employed in this measurement used the sharring method, in which light through the sample was divided into two beams, one of them shifted laterally, and joined to interfere each other. Therefore, the shift of interference fringes shows the difference of optical path length between two points of the sample, such as shown in Fig.5-23. As is shown in Fig.5-24, the measuring process was as follows:

1. The clad thickness adjacent to the core region d_3 was measured with a reflective interference microscope or a talystep scanning at a step between the clad deposited and not deposited regions. With the transparent interference microscope, the shift of interference fringes between the clad deposited and not deposited regions m_1 was measured. Refractive index of the clad n_c was obtained with the following equation:

$$(n_c - 1) d_3 = m_1 \lambda_0 \quad , \quad (5-C1)$$

where λ_0 was the wavelength of light in vacuum.

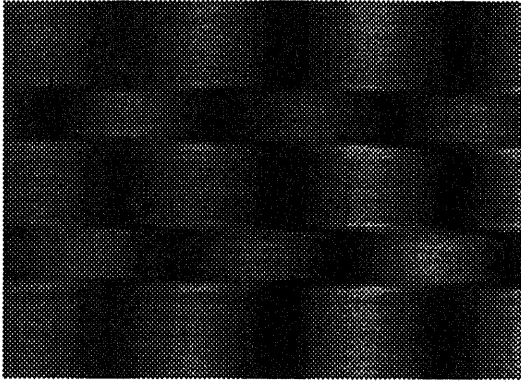
2. The step between the core region and other region d_2 was measured with a reflective interference microscope or a talystep. The shift of interference fringes between the *hollow* core region (before filled with an organic) and the neighbour region m_2 was measured with the transparent interference microscope. The core thickness d_1 was calculated with the following equation:

$$(n_c - 1) (d_2 - d_1) = m_2 \lambda_0 \quad . \quad (5-C2)$$

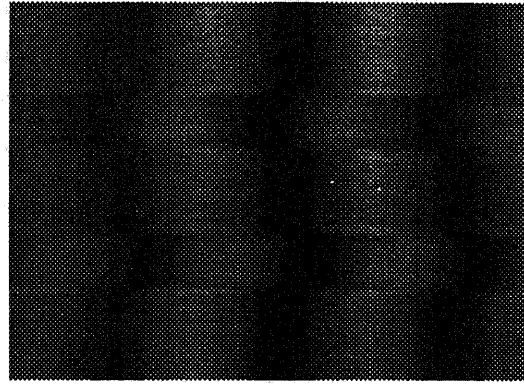
3. The shift of interference fringes between the *organic* core region and the neighbour region was measured with the transparent interference microscope with a polarizer inserted into the optical path. Rotating the polarizer, the maximum and the minimum interference fringe shifts m_{\max} and m_{\min} , and their polarizations θ_{\max} and θ_{\min} , respectively, were measured. The refractive indices were obtained with the following equations:

$$(n_{\max} - 1) d_1 = m_{\max} \lambda_0 - (n_c - 1) (d_3 - d_1) \quad , \quad (5-C3)$$

$$(n_{\min} - 1) d_1 = m_{\min} \lambda_0 - (n_c - 1) (d_3 - d_1) \quad . \quad (5-C4)$$



(a) Polarization with the highest refractive index.



(b) Polarization with the lowest refractive index.

Fig.5-23 Photographs of interference fringes observed with the *Interfaco* microscope. The sample was fabricated with the deposition method and the core thickness was $0.16\mu\text{m}$.

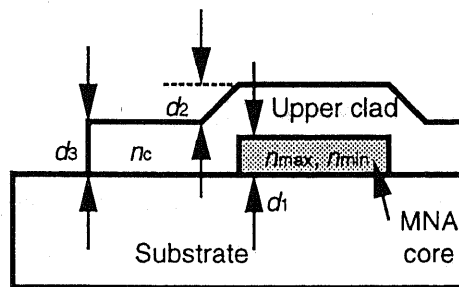


Fig.5-24 The model for refractive indices measurement method

Chapter 6

Evaluation of MNA Waveguides and SHG Devices

6.1 Introductory Remarks

In this chapter, MNA waveguide devices are evaluated. The devices are uniform channel waveguides, Y-branches, and corrugated channel waveguide quasi phase matching SHG devices. All these devices are $3\mu\text{m}$ or $5\mu\text{m}$ in width and $1\mu\text{m}$ in thickness. The single mode limit in the width and thickness for MNA core and SiO_2 clad waveguide is about $0.16\mu\text{m}$ and $0.53\mu\text{m}$ for the wavelength of $0.53\mu\text{m}$ and $1.06\mu\text{m}$, respectively, and hence the waveguides are multimode. Although single mode waveguides is preferable, the waveguide size has been determined based on the available fabrication technology in our laboratory.

In section 6.2, uniform waveguides and Y-branches are evaluated. Light guiding experiment and propagation loss measurement are described.

In section 6.3, SHG devices are evaluated. Light guiding experiment, propagation loss measurement, and SHG experiment are described.

In section 6.4, the results are summarized.

In Appendix 6.A, the SHG efficiency with propagation loss is theoretically derived.

6.2 Evaluation of Channel Waveguides

First of all, uniform channel waveguides were evaluated. The waveguides were fabricated with the deposition method, and the waveguide size was $3\mu\text{m}$ wide, $1\mu\text{m}$ thick, and 4mm long. Figure 6-1 shows the experimental setup for light guiding experiment and propagation loss measurement. Figure 6-2 shows the near field pattern at the output surface of the waveguide. The existence of higher order transversal modes is suggested from the pattern, and this is possible because this waveguide was multimodal. Figure 6-3 shows the scattered light intensity distribution along the longitudinal position, observed with a CCD camera placed normal to the waveguide. Scattered light intensity is regarded as proportional to the guided light intensity, and thus propagation loss can be obtained by fitting this scattered light intensity distribution to an exponential decay curve [61]. The

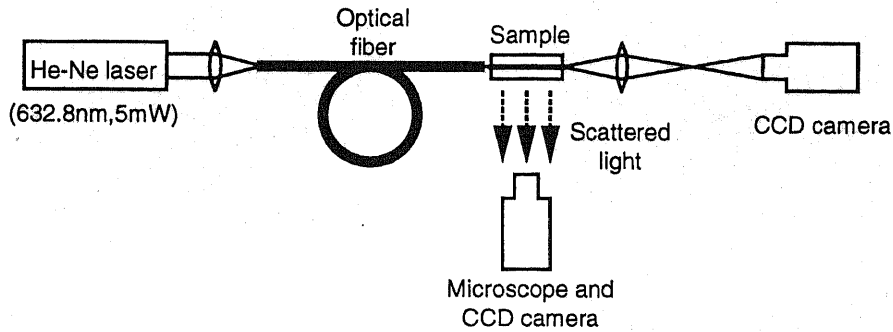


Fig. 6-1 Experimental setup for light guiding and propagation loss measurement of a uniform waveguide

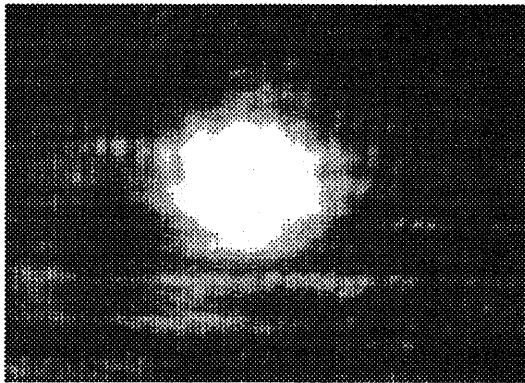
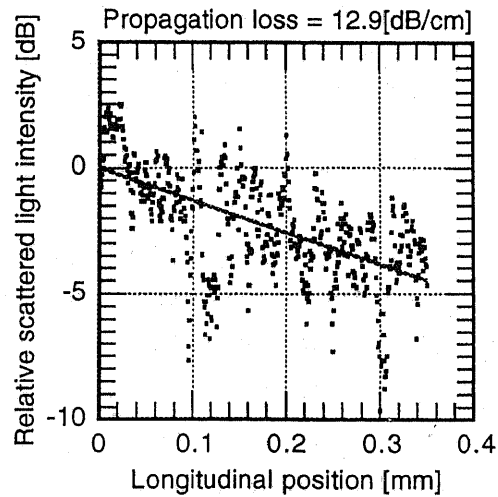


Fig.6-2 Near field pattern of guided light in a uniform waveguide at the output surface



result of the fitting is shown in Fig.6-3 with a full line, and the propagation loss was 12.9dB/cm.

Fig.6-3 Scattered light intensity distribution along the longitudinal position of a uniform waveguide. The fitted line to exponential decay is shown with full line.

Next, a guiding experiment was done with a Y-branch channel waveguide. The waveguides were fabricated with the deposition method using a photomask for Mach-Zhender interferometer devices. The waveguide size was $5\mu\text{m}$ wide and $1\mu\text{m}$ thick. Figure 6-4 shows the experimental setup, and Fig.6-5 shows the output near field pattern and the output cross sectional surface, which clearly shows the optical branching.

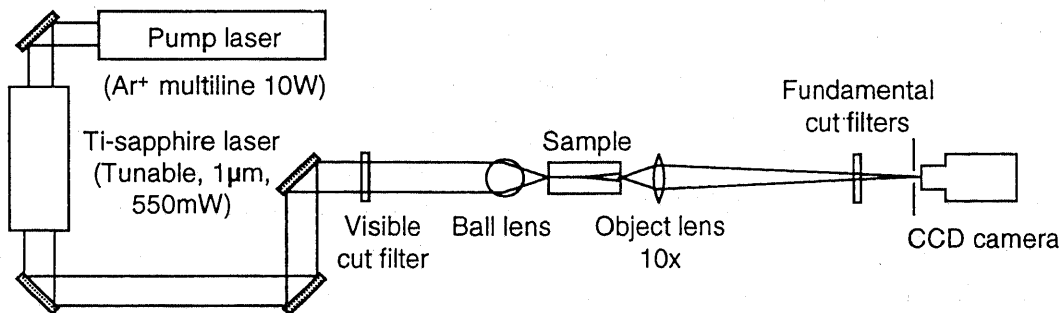


Fig.6-4 Experimental setup for light guiding experiment of a Y-branch waveguide

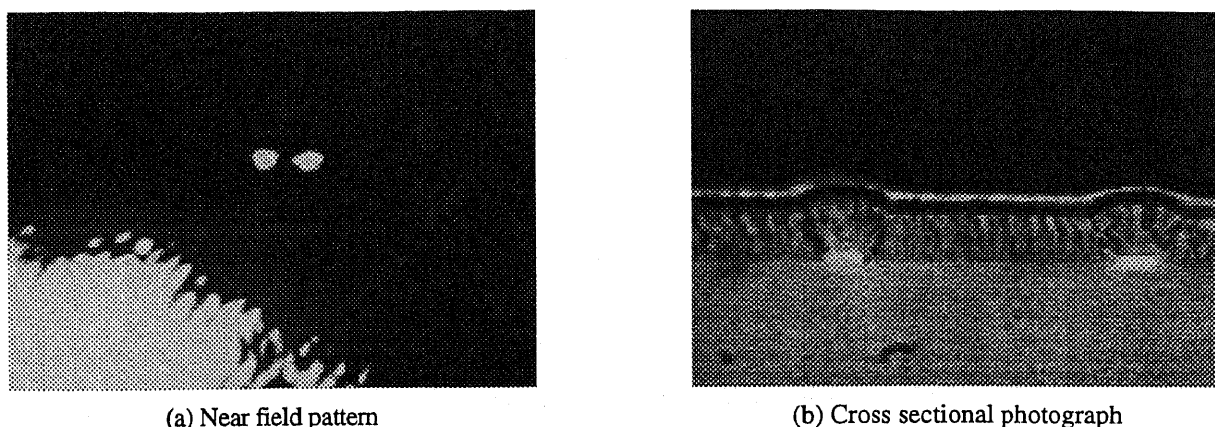


Fig.6-5 Near field pattern of guided light and output cross sectional surface photograph of a Y-branch waveguide

6.3 Evaluation of SHG Devices

The SHG devices were fabricated with the deposition method with interference exposure, described in sections 4.5 and 5.6. The fabrication conditions were as follows: the matrix cores were *TSMR* with a size of $3\mu\text{m}$ wide and $1\mu\text{m}$ thick, with the interference exposure time of 40 seconds for the corrugation depth of $0.2\mu\text{m}$, the SiO_2 upper clad deposition method RF magnetron sputtering with the thickness of $3\mu\text{m}$ followed by the polyimide coating, and the MNA crystal growth Bridgman method II with the speed of 2mm/hour . At first, the corrugation pitch was set $0.65\mu\text{m}$ in order to achieve quasi phase matching for the fundamental wavelength of $1\mu\text{m}$ (see Fig.2-2). Other pitches of $0.8\mu\text{m}$ and $1.0\mu\text{m}$ was also fabricated and evaluated.

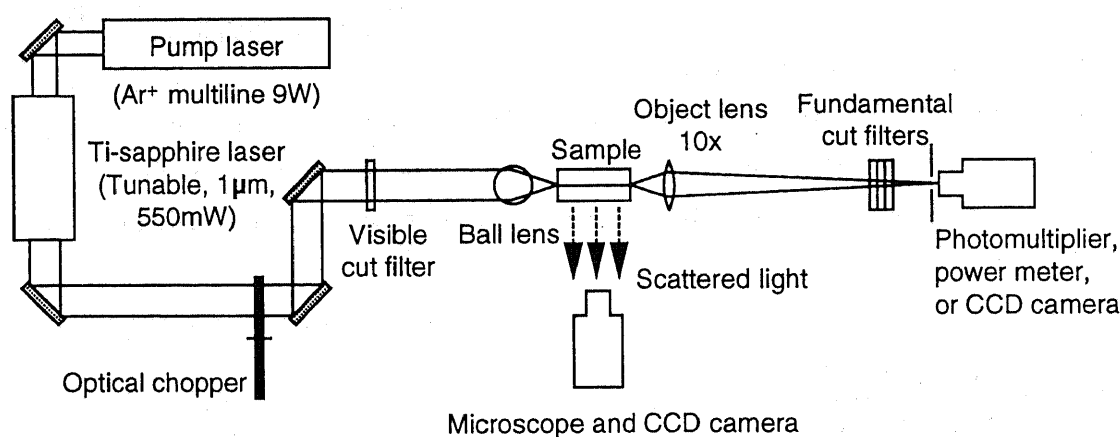


Fig.6-6 Experimental setup for evaluation of SHG devices

The sample was cut to 0.5mm long and set to the experimental setup shown in Fig.6-6. The light from the Ti-sapphire laser (*TITAN-SW*, Schwartz Electro-Optic, Inc.) included scattered pump light from the Ar ion laser, which was visible and disturbed the observation of SHG, and therefore a visible cut filter was inserted. The incident focusing lens needed high transparency in order to keep the light intensity, in addition to short focal length in order to focus the incident light into a small spot. Hence, a ball lens of focal length of 2.38mm was

employed as the incident focusing lens, in place of an ordinary high magnitude object lens for a microscope which used several lenses and had low transparency. The incident beam spot size focused with the ball lens was measured as $3.0\mu\text{m}$, which was consistent to the theoretical estimation.

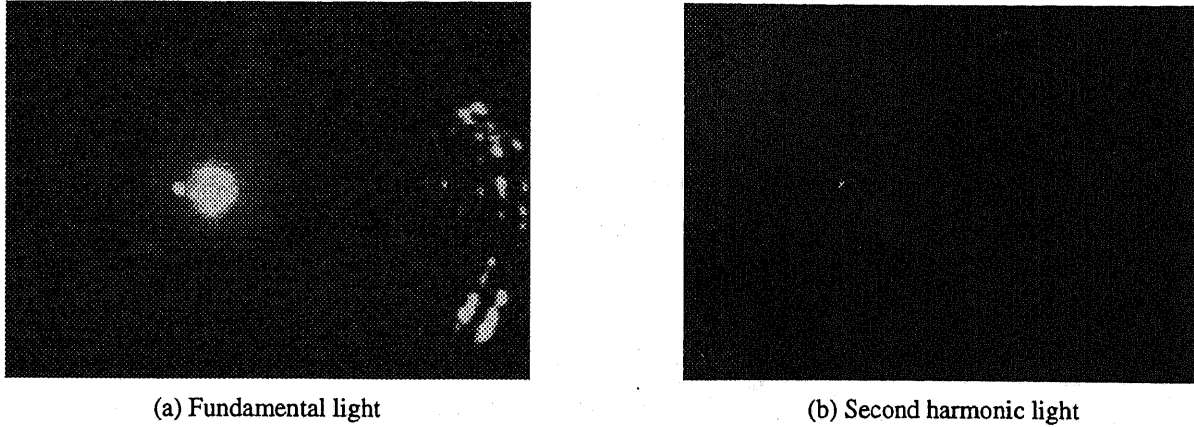


Fig.6-7 Near field pattern of guided lights of a SHG device based on MNA

Figure 6-7(a) shows the output near field pattern of the guided fundamental ($1\mu\text{m}$ of wavelength) light. The existence of higher order guided modes was suggested from the pattern. In these waveguides, coupling between the guided and radiation mode was theoretically expected, and the radiation angle with the first order diffraction for the fundamental wavelength of $1\mu\text{m}$ was estimated to be 83° , 66° , and 49° for a waveguide with the corrugation pitch of $0.65\mu\text{m}$, $0.8\mu\text{m}$, and $1.0\mu\text{m}$, respectively. Experimentally, radiation was observed in the angles which almost coincide with the theoretical estimations. In addition, another radiation was observed in the angle for the effective refractive index of about 1.4. When the incident beam was scanned from above to below the sample, the latter radiation was observed first increasing and then decreasing, followed by the increase and decrease of the former radiation. This fact and the effective refractive index of 1.4 suggest that this radiation was a

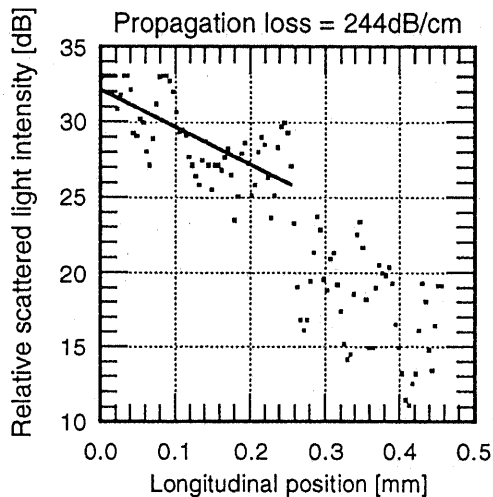


Fig.6-8 Scattered light intensity distribution along the longitudinal position of an SHG device. The fitted line to exponential decay is shown with full line.

leaky guided mode in the upper clad on the core. Figure 6-8 shows the scattered fundamental light intensity distribution along the longitudinal position, observed with a CCD camera placed normal to the waveguide. The propagation loss obtained with the exponential curve fitting was about 250dB/cm . The theoretical radiation loss estimated with the improved perturbation method [41] was 166dB/cm for the fundamental and 9.4dB/cm for the second harmonic. Although the separation between the experimental and theoretical value was not so small, it should be noted that the improved perturbation method is assuming a *planar* waveguide, and that the result with this theory has some error compared with the rigorous spatial harmonic expansion method.

As for the SHG experiment, some points had become clear to be noted from preliminary SHG experiments. The first was that MNA core was sublimated from the incident surface with the heat if the incident fundamental power exceeded about 100mW. On the other hand, second harmonic power was proportional to the square of the fundamental power. Thus, a chopper was inserted into the optical path, as is shown in Fig.6-6, in order to reduce the averaged fundamental power without reducing the peak power. The duty ratio of the chopper was set to 1/8, and core sublimation was sufficiently suppressed. Still, the incident surfaces should be coated for practical long term use, as was mentioned in section 5.6. The second was that the polyimide coated on the upper clad burnt when the fundamental light of higher power than about 100mW was focused on the polyimide layer. This damaged the incident surface of the channel waveguide. Therefore, the optical path was aligned with low power at first and then the power was increased.

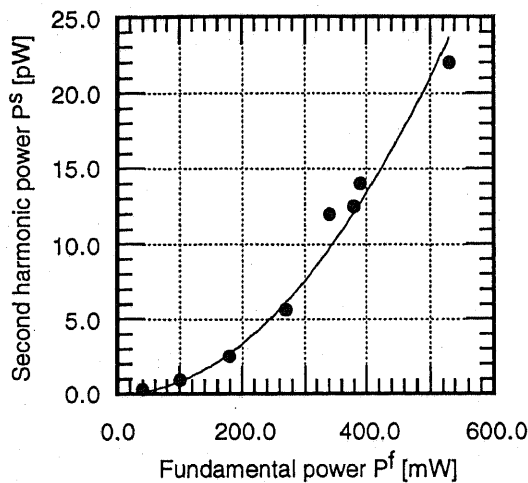


Fig.6-9 Dependence of the detected second harmonic power P_s on the fundamental power P_f for the incident fundamental wavelength of $1\mu\text{m}$. The fundamental power was measured at the output of the Ti-sapphire laser. The full line is the fitted parabolic curve.

First, the SHG experiment was done with a device with the corrugation period of $0.65\mu\text{m}$. The second harmonic was observed from the output surface and from the scattered light normal to the substrate. Figure 6-7(b) shows the output near field pattern of the second harmonic of $0.5\mu\text{m}$. Figure 6-9 shows the dependence of the detected second harmonic power P_s on the fundamental power P_f for the incident fundamental wavelength of $1\mu\text{m}$. The experimental results were well fitted with a parabolic curve (full line). The detected power of the guided fundamental from the output surface was 0.22mW for the incident power of 550mW, and the guided fundamental power at the input surface was estimated to be 42mW after the correction of various factors such as the propagation loss of the waveguide,

the losses of the optical components, and the duty ratio of the optical chopper. Similarly, the second harmonic power was also estimated to be 0.55nW for the detected power of 22pW. Therefore the SHG efficiency was $3.1 \times 10^{-7}/\text{W}$, which was one order smaller than the theoretical value $7.5 \times 10^{-6}/\text{W}$ for a device without corrugation, i.e. the interaction length equals the coherent length. SHG was observed in the fundamental range of $0.9 \sim 1.02\mu\text{m}$, which corresponds to the second harmonic of $0.45\mu\text{m}$ (violet) through $0.51\mu\text{m}$ (green), and the second harmonic power and SHG efficiency were almost same over these wavelength. This was inconsistent with the theory which predicted the existence of a sharp second harmonic power peak through phase matching even if the fundamental propagation loss was as large as 250dB/cm (see Appendix 6.A). These facts suggested that the phase matching was not achieved. The reported values of the refractive index of MNA, shown in Table 6-I, differ each other. In this work, the value in Ref.[30] was employed because the coefficients for the Sellmeier formula was determined only in Ref.[30]. The theoretical corrugation period for the phase matching based on the refractive index of Ref.[62] was about 20~25% larger. Thus, devices with the corrugation period of $0.8\mu\text{m}$ and $1.0\mu\text{m}$ were

fabricated and evaluated. The theoretical phase matching fundamental wavelength based on the refractive index of Ref.[62] was 0.995 μm and 1.031 μm for the corrugation period of 0.8 μm and 1.0 μm , respectively. A small peak of the second harmonic power, of which the increase factor was about 4, was observed at the fundamental wavelength of 1.006 μm for the corrugation period of 0.8 μm , though the increase of the second harmonic power was not observed for the corrugation period of 1.0 μm . Although the refractive index cannot be obtained with this result because the quasi phase matching condition is determined with the difference between the refractive indices of the fundamental and second harmonic, it can be said that the value reported in Ref.[62] may be more correct than the value in Ref.[30].

 Table 6-I Reported values of the refractive index n_x of MNA

	1.064 μm	n_x 0.6328 μm	0.532 μm	Measurement method
Levine et.al. [26]	1.8	1.99	2.28	Transparency spectrum of a thin film etalon
Morita et.al. [30]	1.78	1.99	2.28	Ellipsometry
	1.76	2.00	2.29	Fitted value with the Sellmeir formula
Umegaki [63]	1.80	-	-	Becke line method
Kinoshita et.al. [64]	1.907	-	2.284	?
Zhang et.al. [62]	2.093 \pm 0.001	2.341 \pm 0.001	2.494 \pm 0.001	m-line method of a thin film waveguide

6.4 Concluding Remarks

In this chapter, the evaluation of uniform and Y-branch channel waveguides and corrugated channel waveguide SHG devices were described. Light guiding was confirmed in a uniform channel waveguide, and the measured propagation loss was 12.9dB/cm for 632.8nm. Light guiding and branching was confirmed in a Y-branch channel waveguide, which demonstrated compatibility to an optical integrated circuit. In a SHG device, light guiding and SHG was confirmed for a range of wavelength 0.9~1.01 μm . The propagation loss for fundamental was about 250dB/cm, and the second harmonic power was 0.55nW for a fundamental power of 42mW.

Appendix 6.A SHG Efficiency with Propagation Loss

The coupled mode equations including the propagation loss can be expressed as:

$$\frac{da^f}{dz} = -i \kappa_q^* a^s \exp[-i \Delta\beta_q z] - \alpha^f a^f \quad (6-A1)$$

$$\frac{da^s}{dz} = -i \kappa_q a^{s2} \exp[i \Delta\beta_q z] - \alpha^s a^s \quad (6-A2)$$

where α^f and α^s is the *amplitude* (not the power) loss coefficient, κ_q the nonlinear coupling coefficient defined in Eq.(2-44). Although equations (6-A1) and (6-A2) can be solved analytically for $\alpha^f = \alpha^s = \alpha$ [45], this assumption

is not so practical. Hence, a more practical assumption of $|\kappa_q^* \alpha^s| \ll |\alpha^f|$ is employed here. This assumption means that the fundamental power depletion through the SHG process can be negligible compared with that through the linear loss, and is equivalent to the following expression:

$$\eta_0 \ll \alpha^f l \left| \text{sinc} \left(\frac{\Delta \beta l}{2} \right) \right| \quad (6-A3)$$

where η_0 is the SHG efficiency for the length of l without propagation loss. Under this assumption, the fundamental amplitude is affected only with the propagation loss as:

$$a^f(z) \approx a^f(0) \exp[-\alpha^f z] \quad (6-A4)$$

Substituting Eq.(6-A4) into Eq.(6-A2), the following equation can be obtained:

$$\frac{da^s(z)}{dz} = -i \kappa_q a^f(0)^2 \exp[-2\alpha^f z + i \Delta \beta z] - \alpha^s a^s \quad (6-A5)$$

This equation can be solved with the variable conversion $a^s = b^s \exp[-\alpha^s z]$, resulting into

$$a^s(z) = -i \kappa_q a^f(0)^2 \frac{1 - \exp[(\alpha^s - 2\alpha^f + i \Delta \beta_q) z]}{\alpha^s - 2\alpha^f + i \Delta \beta_q} \exp[-\alpha^s z] \quad (6-A6)$$

Therefore, the SHG efficiency can be derived as:

$$\eta = 2 \omega^2 \left(\frac{\mu_0}{\epsilon_0} \right)^{\frac{3}{2}} \frac{|d_{\text{eff}}|^2}{n_{\text{eff}}^2 n_{\text{eff}}^s S_{\text{eff}}^f} \exp[-2\alpha^s z] \frac{\{1 - \exp[(\alpha^s - 2\alpha^f) z] \cos(\Delta \beta_q z)\}^2 + \exp[2(\alpha^s - 2\alpha^f) z] \sin^2(\Delta \beta_q z)}{(\alpha^s - 2\alpha^f)^2 - \Delta \beta_q^2} \quad (6-A7)$$

In the case of $\alpha^f \gg \alpha^s$ and $a^f z \gg 1$, Eq.(6-A7) can be expressed as:

$$\eta = 2 \omega^2 \left(\frac{\mu_0}{\epsilon_0} \right)^{\frac{3}{2}} \frac{|d_{\text{eff}}|^2}{n_{\text{eff}}^2 n_{\text{eff}}^s S_{\text{eff}}^f} \frac{1}{(\alpha^s - 2\alpha^f)^2 - \Delta \beta_q^2} \exp[-2\alpha^s z] \quad (6-A8)$$

From this equation, the effective interaction length for the perfect phase matching is $1/(2\alpha^f - \alpha^s)$. Fig.6-10 shows the phase matching characteristics for the fundamental propagation loss of 250dB/cm and the second propagation loss of 0. The effective interaction length is about 0.17mm. The dependency on the fundamental wavelength is still quite sharp for such a large propagation loss. It should be noted that only one order of diffraction contributes to the SHG efficiency obtained with Eqs.(6-8) and (6-9), and that the contribution of other orders of diffraction should be considered if the phase mismatch is large.

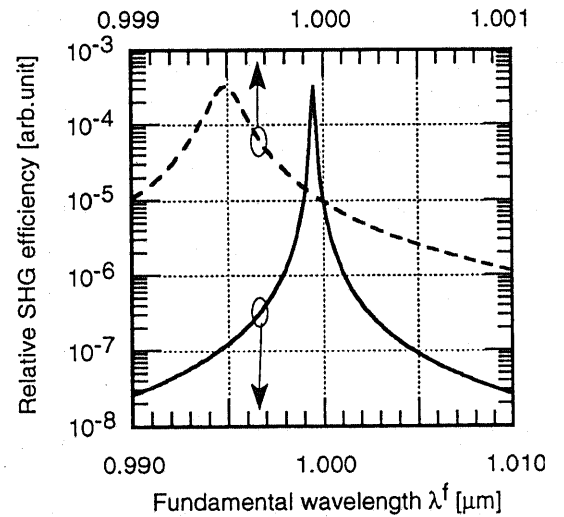


Fig.3-10 Theoretical dependence of the SHG efficiency on the fundamental wavelength for an MNA SHG device of $3\mu\text{m}$ wide and $1\mu\text{m}$ thick with the corrugation period of $0.65\mu\text{m}$. The propagation loss is assumed 250dB/cm for the fundamental and 0 for the second harmonic.

Chapter 7

Conclusion

In this dissertation, theoretical and experimental works on a corrugation quasi phase matching SHG device based on an organic MNA channel waveguide, to realize a high efficiency optical second harmonic device, were described.

In chapter 2, the use of the local normal mode expansion was proposed for SHG analysis in place of the ideal normal mode expansion, which was pointed out as insufficient in the analysis of a quasi phase matching SHG device because of the failure in describing the field profile in a periodic waveguide. A theory based on this local normal mode expansion was developed as follows: first of all, a general form of nonlinear coupled mode equations were derived from the Maxwell equations; then nonlinear coupled mode equations for SHG were derived, followed with the derivation of practical expressions of SHG efficiency, effective SHG coefficient, and figure of merit for SHG.

In chapter 3, some types of quasi phase matching SHG devices were analyzed with the local normal mode expansion theory developed in the previous chapter. Analytical expressions under the strong light confinement approximation were derived and numerical comparison between the local normal mode expansion method and the conventional ideal normal mode expansion method was carried out for examples of quasi phase matching SHG devices with corrugation and with periodic domain inversion.

As a corrugated device, a channel waveguide SHG device based on an organic MNA was analyzed, and characteristic results were obtained as follows: The SHG efficiency and the effective SHG coefficient dropped to 0 for a certain averaged width of waveguide, which was caused through the cancellation of modulation in field confinement and intensity. This result did not appear with the ideal normal mode expansion method. In addition, the dependence of SHG efficiency on the averaged waveguide width was quite different between the local normal mode expansion and the ideal normal mode expansion. This difference was attributed to the ability of description of the field profile in a periodic waveguide.

As a periodic domain inversion device, a channel waveguide SHG device based on LiNbO_3 was analyzed. The results with the local normal mode expansion and with the ideal normal mode expansion were almost completely coincident, which could explained by the fact that the field profile was almost uniform in this type of device.

In chapter 4, new methods to fabricate channel waveguides based on an organic crystal were proposed. In these methods, hollow cores are fabricated and organic crystals are filled into them.

Two methods, the deposition method and the sticking method, were proposed for the hollow core fabrication. In the deposition method, a matrix core is fabricated with photolithography, then an upper clad is deposited on it, and at last the matrix core is removed. In the sticking method, a substrate is grooved with photolithography and etching, and then faced with another substrate and heated to stick together. Both methods have advantages as follows: since the waveguide form is determined with the photolithography process, waveguides with complicated form such as a grating and a branch can be fabricated precisely. Also the core thickness can be determined accurately by controlling the thickness of the matrix core in the deposition method and the etched depth of the trench in the sticking method. Moreover, the organic core is protected by the upper clad layer. By choosing various materials for the clad, the degree of freedom in designing a waveguide increases considerably.

In order to fabricate a corrugated channel waveguide, the deposition method with interference exposure was proposed. In this method, a photoresist layer is exposed with interference fringe and ordinary channel pattern, and developed into a corrugated matrix core. The interference exposure time is controlled to fabricate certain depth of corrugation. Upper clad is deposited on it, and the matrix core is removed to fabricate a corrugated hollow core.

In chapter 5, the results of experimental examination of each step of the fabrication methods of an organic channel waveguide was described, which are summarized as follows:

In the deposition method, photoresists were superior to evaporated Al film as a matrix core material, mainly because of the film surface smoothness and ease of removal. Positive photoresists were compatible to the interference exposure process for corrugated waveguides, and a high resolution positive photoresist, *TSMR*, was especially preferable because of its rectangular cross section. As an upper clad deposition method, the sol-gel method was not preferable in spite of its excellent step coverage, mainly because of its shrinkage during the bake process which brought fatal deformation to the photoresist matrix core, and of its low deposition rate. Plasma-CVD method was not preferable for its rather high deposition temperature and for its rather large film stress. RF sputter method and RF magnetron sputter method was preferable for its low deposition temperature with a trick to improve thermal contact between a sample and a holder. However, the conditions for high film quality and low film stress were incompatible with each other, and some special processes such as the two step sputtering method or the additional polyimide coating method must be employed to obtain a sufficient result. As the matrix core removal method, the HCl soaking method was not practical because of its very low removal rate, and this was one of the reasons for the inadequacy of the evaporated Al film for the matrix core. This was same for the remover soaking method. The incineration method and the acetone soaking method had reasonable removal rate, and the latter was more preferable for its low process temperature. In short, the best was the combination of *TSMR* photoresist as the matrix core, the RF magnetron sputtering method combined with the two-step deposition or the additional polyimide coating method as the upper clad deposition method, and the acetone soaking method as the matrix core removal method.

In the sticking method, cover glass substrates was able to be stuck completely at 600~620°C for 1 hour, without vanishing of the etched grooves. Wet etching with buffered HF had a disadvantage of limited etching depth up to about 0.3 μ m, and dry etching with CF₄ RIE needed more examination on the etching conditions.

In the deposition method with interference exposure, relations between the magnitude of exposure and the corrugation depth was obtained, and 80 seconds of exposure for the *OFPR-800* photoresist and 40 seconds of exposure for the *TSMR* photoresist was suitable to obtain the degree of modulation in the photoresist thickness of 0.2.

In order to grow a high quality MNA crystal core, it was necessary to establish a uniform and well controlled temperature distribution in the middle of a furnace and a steep temperature gradient in the edge of the furnace, which was realized by reducing the space around a sample within a furnace. In addition, sufficiently slow speed, as low as 2mm/hour, was preferable for high quality crystal growth. Under these conditions, the preferable crystal orientation, i.e. transversally oriented *x* axis, was obtained, even though perfect orientation was not achievable.

End surfaces with high quality and normal to waveguides was obtainable with the multi-time scribing method with a wafer scriber.

From these examinations, the fundamental fabrication conditions have been determined. Although these can be improved more, the new organic channel waveguide fabrication methods have been established.

In chapter 6, the evaluation of uniform and Y-branch channel waveguides and corrugated channel waveguide SHG devices was described. Light guiding was confirmed in a uniform channel waveguide, and the measured propagation loss was 12.9dB/cm for 632.8nm. Light guiding and branching was confined in a Y-branch channel waveguide, which demonstrated compatibility of these new fabrication methods to an optical integrated circuit. In a SHG device, light guiding and SHG was confirmed for a range of wavelength 0.9~1.02 μ m. The propagation loss for fundamental was about 250dB/cm, and the second harmonic power was 0.55nW for a fundamental power of 42mW. From the phase matching characteristics, it was suggested that some of the reported refractive index value of MNA were not correct.

As is described above, new methods for theoretical analysis and fabrication of channel waveguide SHG devices based on an organic nonlinear material have been established in this dissertation. However, the currently obtained devices were still insufficient. Hence, as concluding remarks, we would like to point out some matters to be investigated in order to achieve practical high efficiency SHG devices.

The quasi phase matching SHG devices with corrugation which have been studied in this work have a disadvantage that large propagation loss is caused by the phase matched coupling between the guided and radiation modes. There are three methods to avoid this. The first method is the contra-directional phase matching method in which phase matching is achieved between a fundamental and a second harmonic mode propagating in the opposite direction to each other. The period of the first order corrugation for the contra-directional phase matching

is very small, e.g. about $0.1\mu\text{m}$, and no coupling to a radiation mode is caused. It should be noted that higher order grating may cause the coupling to radiation modes, and hence a fabrication technology for such a short period corrugation is needed. In addition, the short period may make the LNME single mode approximation invalid, and thus theoretical analysis methods should be investigated. The second method to reduce the propagation loss is the use of a higher order grating in the ordinary codirectional phase matching. If the first order diffraction cannot couple the guided mode to a radiation mode, the propagation loss will be reduced a lot. However, it should be noted that a higher order grating also reduces the SHG efficiency. The third method to reduce the propagation loss is the use of a clad material which has a refractive index very near to the core at the fundamental wavelength, in order to reduce the coupling coefficient. It should be noted, however, that this weakens the fundamental optical confinement resulting into reduction of the field modulation, i.e. the reduction of the SHG efficiency.

In order to fabricate high quality waveguides with reproducibility, many matters of the fabrication processes should be improved. Especially, the organic crystal growth condition and the crystal orientation should be further investigated, including examination of some *active* methods such as electric field poling. In addition, other clad materials than SiO_2 and cover glass should be investigated in order to increase the flexibility in the waveguide design. Moreover, the refractive index of organic materials must be determined exactly before designing a waveguide.

In order to analyze quasi phase matched SHG devices more exactly and to make the limit of the validity of the single mode LNME clearer, multimode theory and numerical methods should be investigated.

As is described above, many matters still remain to be investigated. Although, or maybe because, organic materials have infinite diversity, their characterization and fundamental investigation, such as determination of the refractive index and crystal growth method, often seems too much insufficient compared with inorganic materials. In order to make organics match against superior inorganics such as LiNbO_3 and LiTaO_3 , those fundamental matters seems necessary to be further investigated.

Acknowledgments

First of all, I express my deepest gratitude to Prof. Kunio TADA who have given me the chance of working in this project and have provided guidance and support all along this work. I am deeply indebted to Prof. Kazuro KIKUCHI who introduced me to the fascinating world of nonlinear optics. His guidance, suggestions, and discussions in a very wide field from the quantum optics to the crystal growth of MNA have helped and encouraged me a lot. I would like to appreciate Prof. Takanori OKOSHI, Prof. Yoichi FUJII, Prof. Takeshi KAMIYA, and Prof. Kazuo HOTATE for their helpful comments and criticisms. I greatly acknowledge advices and suggestions from Prof. Yoshiaki NAKANO.

I would like to express my whole-hearted thanks to all members of Tada/Nakano Lab. for their helps, discussions, and friendships. Especially, I would like to thank Dr. Yukihiro SHIMOGAKI for his guidance and advice on SiO₂ deposition and Macintosh computers, and Mr. Toru MURAI for his looking after me in so many matters of daily life, financial work, and public relations. Dr. Hideki HAYASHI (presently with Sekisui Chem. Co.) for discussion on the crystal growth of organic materials, Dr. Takuya ISHIKAWA (presently with Furukawa Electric Works Co.) and Dr. Yoshitaka OKADA (presently with Tsukuba Univ.) for advice on some matters in my experiments, Prof. Yi LUO (presently with the Tsinghua Univ., China) for guidance on the photolithography, Mr. Jun-ichi HASHIMOTO (presently with Sumitomo Electric Works Co.) for guidance on the RF sputter, and Dr. Toshiya YUHARA (presently with Hitachi Cable Co.) for advice and discussion on many matters in my experiments,. Dr. Hong-Li CAO, Mr. Nong CHEN, and Mr. Shen-Min LIN for their helping me on the interference exposure and reactive ion etching, are acknowledged very much. I would like to express my thanks to Mr. Yuen-Chuen CHAN for taking care of my poor English, besides so many fruitful discussions. Mr. Akio ISHIKAWA, Mr. Akihiro KANAZAWA, and Mr. Hiroshi HIRAYAMA who made every possible effort as my collaborators during their graduate research, are greatly appreciated.

I also thank Mr. Kazuya OKAMOTO of Nikon Co. for a lot of fruitful discussions and suggestions especially on the photoresists and interference exposure. Mr. Yasuyuki SAKAGUCHI of Showa Electric Works Co. is acknowledged for his advices on the cleaning process.

Mr. Takashi KONDO of the Department of Applied Physics for fruitful discussions, Dr. Norihide YAMADA of Hewlett Packard Labs. Japan and Dr. Tomohiro ONDA of the Department of Applied Physics for their kind invitation to the very interesting seminar, Dr. Shinji ARAMAKI of Mitsubishi Kasei Co. for helpful discussions, are appreciated a lot.

Acknowledgements

All members of Okoshi/Kikuchi Lab. who kindly allowed me to use the transparent interference microscope, of Nishinaga/Tanaka Lab. to use the ellipsometer, and of Katoda Lab. to use the talystep, are appreciated very much.

Last but not least, I would like to express my whole-hearted gratitude to my parents and brother who have encouraged and supported me continuously.

References

- [1] M. C. Teich and B. E. A. Saleh, in *Progress in optics XXVI* (E. Wolf, ed.), pp.1-104, North-Holland Publisher, Amsterdam (1988)
- [2] T. Kobayashi, ed., *Nonlinear optics of organics and semiconductors*, Springer Proceedings of Physics, Springer-Verlag, Berlin (1989)
- [3] D. S. Chemla and J. Zyss, ed., *Nonlinear optical properties of organic molecules and crystals*, Academic Press, Orland (1987)
- [4] R. C. Miller, "Optical second harmonic generation in piezoelectric crystals", *Appl. Phys. Lett.*, Vol.5, pp.17-19 (1964)
- [5] C. Flytzanis and J. Ducuing, "Second-order optical susceptibilities of III-V semiconductors", *Phys. Rev.*, Vol.178, pp.1218-1228 (1969)
- [6] J. Zyss and D. S. Chemla, in *Nonlinear optical properties of organic molecules and crystals* (D. S. Chemla and J. Zyss, ed.), Vol.1, pp.23-192, Academic Press, Orland (1987)
- [7] K. D. Singer, S. L. Lalama, J. E. Sohn, and R. D. Small, "Electro-optic organic materials" in *Nonlinear optical properties of organic molecules and crystals* (D. S. Chemla and J. Zyss, ed.), Vol.1, pp.437-468, Academic Press, Orland (1987)
- [8] T. Kobayashi, "Organic nonlinear optics", *Oyo Buturi*, Vol.57, pp.174-189 (1988) (in Japanese)
- [9] M. M. Fejer, G. A. Magel, and E. J. Lim, "Quasi-phase-matched interactions in lithium niobate", *Proc. Photo. Opt. Soc. (SPIE)*, Vol.1148, pp.213-224 (1989)
- [10] N. Uesugi and T. Kimura, "Efficient second-harmonic generation in three-dimensional LiNbO₃ optical waveguide", *Appl. Phys. Lett.*, Vol.29, pp.572-574 (1976)
- [11] H. Ito and H. Inaba, "Efficient phase-matched second-harmonic generation method in four-layered optical-waveguide structure", *Opt. Lett.*, Vol.2, pp.139-141 (1978)
- [12] E. J. Lim, S. Matsumoto, and M. M. Fejer, "Noncritical phase matching for guided-wave frequency conversion", *Appl. Phys. Lett.*, Vol.57, pp.2294-2296 (1990)
- [13] N. Hashizume, T. Kondo, T. Onda, N. Ogasawara, and S. Umegaki, "Theoretical analysis of Cerenkov-type optical second-harmonic generation in slab waveguide", *IEEE J. Quantum Electron.*, Vol.28, pp.1798-1815 (1992)
- [14] T. Onda and R. Ito, "Theory of optical second-harmonic generation in slab waveguides with dissipative nonlinear dielectric cores", *Jpn. J. Appl. Phys.*, Vol.30, pp.2770-2780 (1991)
- [15] R. Normandin and G. I. Stegeman, "Picosecond signal processing with planar, nonlinear integrated optics", *Appl. Phys. Lett.*, Vol.36, pp.253-255 (1980)
- [16] R. Normandin and G. I. Stegeman, "A picosecond transient digitizer based on nonlinear integrated optics", *Appl. Phys. Lett.*, Vol.40, pp.759-761 (1982)
- [17] D. Vakhshoori and S. Wang, "Demonstration of an AlGaAs/GaAs integrable optical correlator using surface-emitting second-harmonic generation", *Appl. Phys. Lett.*, Vol.53, pp.347-349 (1988)
- [18] N. Uesugi, K. Daikoku, and K. Kubota, "Electric field tuning of second-harmonic generation in a three-dimensional LiNbO₃ optical waveguide", *Appl. Phys. Lett.*, Vol.34, pp.60-62 (1979)
- [19] K. Yamamoto, K. Mizuuchi, and T. Taniuchi, "Milliwatt-order blue-light generation in a periodically domain-inverted LiTaO₃ waveguide", *Opt. Lett.*, Vol.16, pp.1156-1158 (1991)
- [20] K. Mizuuchi and K. Yamamoto, "Generation of blue light by quasiphasematching SHG in LiTaO₃", *Technical Digest of Conference on Lasers and Electro-Optics (CLEO)*, CThA1, pp.388-389 (1992)
- [21] J. P. van der Ziel, M. Ilegems, P. W. Foy, and R. M. Mikulyak, "Phase-matched second harmonic

- generation in a periodic GaAs waveguide", *Appl. Phys. Lett.*, Vol.29, pp.775-777 (1976)
- [22] P. J. Vella, R. Normandin, and G. I. Stegeman, "Enhanced second-harmonic generation by counter-propagating guided optical waves", *Appl. Phys. Lett.*, Vol.38, pp.759-760 (1981)
 - [23] C. Liao, P. Bundman, and G. I. Stegeman, "Second harmonic generation with surface guided waves in signal processing geometries", *J. Appl. Phys.*, Vol.54, pp.6213-6217 (1983)
 - [24] J. Khurgin, "Second-order susceptibility of asymmetric coupled quantum well structures", *Appl. Phys. Lett.*, Vol.51, pp.2100-2102 (1987)
 - [25] J. Khurgin, "Second-order nonlinear effects in asymmetric quantum-well structures", *Phys. Rev. B*, Vol.38, pp.4056-4066 (1988)
 - [26] B. F. Levine, C. G. Bethea, C. D. Thurmond, R. T. Lynch, and J. L. Bernstein, "An organic crystal with an exceptionally large optical second-harmonic coefficient: 2-methyl-4-nitroaniline", *J. Appl. Phys.*, Vol.50, pp.2523-2527 (1979)
 - [27] G. F. Lipscomb, A. F. Garito, and R. S. Narang, "An exceptionally large linear electro-optic effect in the organic solid MNA", *J. Chem. Phys.*, Vol.75, pp.1509-1516 (1981)
 - [28] G. F. Lipscomb, A. F. Garito, and R. S. Narang, "A large linear electro-optic effect in a polar organic crystal 2-methyl-4-nitroaniline", *Appl. Phys. Lett.*, Vol.38, pp.663-665 (1981)
 - [29] R. Morita, T. Kondo, Y. Kaneda, A. Sugihashi, N. Ogasawara, S. Umegaki, and R. Ito, "Dispersion of second order nonlinear optical coefficient d_{11} of 2-methyl-4-nitroaniline(MNA)", *Jpn. J. Appl. Phys.*, Vol.27, pp.L1131-L1133 (1988)
 - [30] R. Morita, N. Ogasawara, S. Umegaki, and R. Ito, "Refractive indices of 2-methyl-4-nitroaniline (MNA)", *Jpn. J. Appl. Phys.*, Vol.26, pp.L1711-L1713 (1987)
 - [31] S. Somekh and A. Yariv, "Phase-matchable nonlinear optical interactions in periodic thin films", *Appl. Phys. Lett.*, Vol.21, pp.140-141 (1972)
 - [32] S. Somekh and A. Yariv, "Phase matching by periodic modulation of the nonlinear optical properties", *Opt. Commun.*, Vol.6, pp.301-304 (1972)
 - [33] B. F. Levine, C. G. Bethea, and R. A. Logan, "Phase-matched second harmonic generation in a liquid-filled waveguide", *Appl. Phys. Lett.*, Vol.26, pp.375-377 (1975)
 - [34] B. U. Chen, C. C. Ghizoni, and C. L. Tang, "Phase-matched second-harmonic generation in solid thin films using modulation of the nonlinear susceptibilities", *Appl. Phys. Lett.*, Vol.28, pp.651-653 (1976)
 - [35] B. Jaskorzynska, G. Arvidsson, and F. Laurell, "Periodic structures for phase-matching in second harmonic generation in titanium lithium niobate waveguides", *Proc. Photo. Opt. Soc. (SPIE)*, Vol.651, pp.221-228 (1986)
 - [36] T. Suhara and H. Nishihara, "Theoretical analysis of waveguide second-harmonic generation phase matched with uniform and chirped grating", *IEEE J. Quantum Electron.*, Vol.QE-26, pp.1265-1276 (1990)
 - [37] A. W. Snyder, "Coupling of modes on a tapered dielectric cylinder", *IEEE Trans. Microwave Theory Tech.*, Vol.MTT-18, pp.383-392 (1970)
 - [38] D. Marcuse, *Theory of dielectric waveguides*, Academic Press, New York (1974)
 - [39] S. R. Seshadri, "Coupling of guided modes in thin films with surface corrugation", *J. Appl. Phys.*, Vol.63, pp.R115-R143 (1988)
 - [40] C. Vassallo, *Optical Waveguide Concepts*, Elsevier Science Publishers, Amsterdam (1991)
 - [41] H. Nishihara, M. Haruna, and T. Suhara, *Optical Integrated Circuits*, McGraw-Hill, New York (1989)
 - [42] E. A. J. Marcatili, "Dielectric rectangular waveguide and directional coupler for integrated optics", *Bell Sys. Tech. J.*, pp.2071-2102 (1966)
 - [43] R. A. Steinberg and T. G. Giallorenzi, "Modal fields of anisotropic channel waveguide", *J. Opt. Soc. Am.*, Vol.67, pp.523-533 (1977)
 - [44] A. Yariv, *Optical Electronics Fourth Edition*, Saunderson Publishing, Philadelphia (1991)
 - [45] J. A. Armstrong, N. Bloembergen, J. Ducuing, and P. S. Pershan, "Interactions between light waves in a nonlinear dielectric", *Phys. Rev.*, Vol.127, pp.1918-1939 (1962)
 - [46] A. Yariv, "Coupled-mode theory for guided-wave optics", *IEEE J. Quantum Electron.*, Vol.QE-9, pp.919-

- [47] M. M. Choy, W. R. Cook, R. F. S. Hearmon, H. Jaffe, J. Jerphagnon, S. K. Kurtz, S. T. Liu, and D. F. Nelson, in *Landolt-Börnstein numerical data and functional relationships in science and technology new series* (K. Hellwege and A. M. Hellwege, ed.), Vol.11, pp.154, Springer-Verlag, Berlin (1979)
- [48] T. Uemiya, N. Uenishi, Y. Shimizu, S. Okamoto, K. Chikuma, T. Tohma, and S. Umegaki, "Crystal cored fiber using organic material and focusing properties of generated second-harmonic wave", *Proc. Photo. Opt. Soc. (SPIE)*, Vol.1148, pp.207-212 (1990)
- [49] C. Goto, A. Harada, K. Kamiyama, and S. Umegaki, "Highly efficient generation of blue-green coherent light from optimally designed nonlinear optical fiber with organic core-crystal", *Technical Digest of Conference on Lasers and Electro-Optics (CLEO) CThA4*, pp.392-393 (1992)
- [50] H. Murayama, K. Muta, H. Takezoe, and A. Fukuda, "Control of organic-crystal orientation in glass capillary by modified Bridgeman-Stockbarger method", *Jpn. J. Appl. Phys. 2 (Lett.)*, Vol.31, pp.L710-L712 (1992)
- [51] T. Kondo, N. Hashizume, S. Miyoshi, R. Morita, N. Ogasawara, S. Umegaki, and R. Ito, "Frequency doubling of laser diode light in organic channel waveguides", *Technical Digest of Proc. Photo. Opt. Instrumen. Soc. (SPIE)*, pp.53-59 (1990)
- [52] N. E. Schlotter, J. L. Jackel, P. D. Townsend, and G. L. Baker, "Fabrication of channel waveguides in polydiacetylenes: composite diffused glass/polymer structure", *Appl. Phys. Lett.*, Vol.56, pp.13-15 (1990)
- [53] K. Tsuda, T. Kondo, F. Saito, T. Kudo, and R. Ito, "New fabrication method of channel optical waveguides of organic crystal using an inorganic photoresist", *Jpn. J. Appl. Phys. 2 (Lett.)*, Vol.31, pp.L134-L135 (1992)
- [54] W. W. Ng, C. S. Hong, and A. Yariv, "Holographic interference lithography for integrated optics", *IEEE Trans.*, Vol.ED-25, pp.1193-1200 (1978)
- [55] L. F. Johnson, G. W. Kammlott, and K. A. Ingersoll, "Generation of periodic surface corrugations", *Appl. Opt.*, Vol.17, pp.1165-81 (1978)
- [56] A. C. Adams, F. B. Alexander, C. D. Capio, and T. E. Smith, "Characterization of plasma-deposited silicon dioxide", *J. Electrochem. Soc.*, Vol.128, pp.1545-51 (1981)
- [57] Tokyo Ohka Kogyo Co., Ltd., *Product catalogue of resists for semiconductor fabrication* (1990) (in Japanese)
- [58] A. Kinbara, *The Sputtering Phenomena: Fundamental and Application to Thin Films and Coating Technology*, The University of Tokyo Press, Tokyo (1984) (in Japanese)
- [59] A. Suzuki and K. Tada, "Fabrication of chirped gratings on GaAs optical waveguides", *Thin Solid Films*, Vol.72, pp.419-426 (1980)
- [60] T. Sano, "A study on crystal growth of an organic nonlinear optical crystal 2-methyl-4-nitroaniline (MNA)", Thesis for master degree (major in chemistry), Faculty of Science, Graduate school of Tohoku University (1988) (in Japanese)
- [61] S. Sakka, *Science in the Sol-Gel Method - Low Temperature Synthesis of Functional Glasses and Ceramics-*, Agune-Shofusha, Tokyo (1988) (in Japanese)
- [62] Y. Okamura, S. Yoshinaka, and S. Yamamoto, "Measuring mode propagation losses of integrated optical waveguides: a simple method", *Appl. Opt.*, Vol.22, pp.3892-3894 (1983)
- [63] G. Zhang and K. Sasaki, "Measuring anisotropic refractive indices and film thicknesses of thin organic crystals using the prism coupling method", *Appl. Opt.*, Vol.27, pp.1358-1362 (1988)
- [64] S. Umegaki, "Optical second harmonic generation in an optical fiber: MNA", *Gekkan-Physics(Physics Monthly)*, Vol.8, pp.78-82 (1987) (in Japanese)
- [65] T. Kinoshita and K. Sasaki, "Organic nonlinear waveguides", *Shingaku-Gihou(Paper of Tech. Group on Electron. Components and Materials, IEICE of Jpn.)*, CPM87-20 (1987) (in Japanese)

Publication List

Papers related to this dissertation

- 1) T. Isoshima and K. Tada, "Local normal mode analysis of second harmonic generation in periodic waveguides", submitted to *IEEE J. Quantum Electron.*
- 2) T. Isoshima, A. Ishikawa, A. Kanazawa, H. Hirayama, and K. Tada, "Fabrication and evaluation of buried channel organic nonlinear waveguides and second harmonic generation devices", to be submitted.

International conferences related to this dissertation

- 3) T. Isoshima and K. Tada, "Local normal-mode expansion for analysis of second-harmonic generation efficiency", *Technical Digest of Integrated Photonics Research (IPR'91)*, ThC5 (1991)
- 4) T. Isoshima, A. Ishikawa, A. Kanazawa, H. Hirayama, and K. Tada, "Fabrication of buried channel organic nonlinear waveguides", *Technical Digest of Nonlinear Optics: Materials, Fundamentals, and Applications Second Topical Meeting (Nonlinear Optics '92)*, MD27 (1992)

Domestic conferences related to this dissertation (in Japanese)

- 5) K. Tada and T. Isoshima, "Conversion efficiency of MNA channel waveguide SHG device", *Extended Abstracts (The 50th Autumn Meeting, 1989)*; *Jpn. Soc. Appl. Phys.*, 29p-ZH-5 (1989)
- 6) T. Isoshima and K. Tada, "Local mode expansion analysis of quasi-phase-matched SHG efficiency in a periodic structure", *Extended Abstracts (The 51th Autumn Meeting, 1990)*; *Jpn. Soc. Appl. Phys.*, 29p-P-9 (1990)
- 7) T. Isoshima, A. Ishikawa, A. Kanazawa, and K. Tada, "Channel waveguides using low molecular weight organic nonlinear optical materials", *Extended Abstracts (The 38th Spring Meeting, 1991)*; *Jpn. Soc. Appl. Phys. and Related Societies*, 28p-PA-13 (1991)
- 8) T. Isoshima, A. Ishikawa, A. Kanazawa, and K. Tada, "Channel waveguide fabrication process suitable for low-molecular-weight organic nonlinear optical materials", *Proceedings of the First Electronics, Information, and System Conference; Electronics, Information, and System Society, IEE of Jpn.*, A-1-16 (1991)
- 9) T. Isoshima and K. Tada, "Local mode expansion analysis of quasi-phase-matched SHG efficiency in a periodic structure II", *Extended Abstracts (The 52th Autumn Meeting, 1991)*; *Jpn. Soc. Appl. Phys.*, 11p-ZN-1 (1991)
- 10) T. Isoshima, H. Hirayama, and K. Tada, "Analysis of second harmonic generation devices phase matched with the modal dispersion in a multilayer core", *Extended Abstracts (The 53th Autumn Meeting, 1992)*; *Jpn. Soc. Appl. Phys.*, 18a-X-9 (1992)

Other publications

- 11) K. Kikuchi and T. Isoshima, "Photon-counting cross-correlation using avalanche photodiodes", *Technical Digest of Conference on Laser and Electro-optics (CLEO'89)*, TuJ21 (1989)
- 12) K. Kikuchi, T. Isoshima, and M. Yamada, "Photon-counting receiver in near-infra-red region: use of GaInAs avalanche photodiode", *Electron. Lett.*, Vol.25, pp.1028-1029 (1989)